GDAŃSK UNIVERSITY OF TECHNOLOGY

The author of the doctoral dissertation: Michał Kamil Rycewicz
Scientific discipline: Automation, Electronics, Electrical Engineering and Space Technologies

DOCTORAL DISSERTATION

Title of doctoral dissertation: Structural and electronic properties of diamond-composed heterostructures

Title of doctoral dissertation (in Polish): Właściwości strukturalne i elektroniczne heterostruktur diamentowych

Supervisor *signature*
Robert Bogdanowicz, Ph. D., Assoc. Prof.

Gdańsk, year 2023

GDAŃSK UNIVERSITY OF TECHNOLOGY

STATEMENT

The author of the doctoral dissertation: Michał Kamil Rycewicz

I, the undersigned, declare that I am aware that in accordance with the provisions of Art. 27 (1) and (2) of the Act of 4th February 1994 on Copyright and Related Rights (Journal of Laws of 2021, item 1062), the university may use my doctoral dissertation entitled:
Structural and electronic properties of diamond-composed heterostructures
for scientific or didactic purposes.[1]

Gdańsk,..... .....

signature of the PhD student

Aware of criminal liability for violations of the Act of 4th February 1994 on Copyright and Related Rights and disciplinary actions set out in the Law on Higher Education and Science(Journal of Laws 2021, item 478), as well as civil liability, I declare, that the submitted doctoral dissertation is my own work.

I declare, that the submitted doctoral dissertation is my own work performed under and in cooperation with the supervision of Robert Bogdanowicz, Ph. D., Assoc. Professor.

This submitted doctoral dissertation has never before been the basis of an official procedure associated with the awarding of a PhD degree.

All the information contained in the above thesis which is derived from written and electronic sources is documented in a list of relevant literature in accordance with Art. 34 of the Copyright and Related Rights Act.

I confirm that this doctoral dissertation is identical to the attached electronic version.

Gdańsk,..... .....

signature of the PhD student

I, the undersigned, agree/do not agree* to include an electronic version of the above doctoral dissertation in the open, institutional, digital repository of Gdańsk University of Technology.

Gdańsk,..... .....

signature of the PhD student

[1] Art 27. 1. Educational institutions and entities referred to in art. 7 sec. 1 points 1, 2 and 4–8 of the Act of 20 July 2018 – Law on Higher Education and Science, may use the disseminated works in the original and in translation for the purposes of illustrating the content provided for didactic purposes or in order to conduct research activities, and to reproduce for this purpose disseminated minor works or fragments of larger works.

2. If the works are made available to the public in such a way that everyone can have access to them at the place and time selected by them, as referred to in para. 1, is allowed only for a limited group of people learning, teaching or conducting research, identified by the entities listed in paragraph 1.

ABSTRACT

Diamond is a promising material for 21st century electronics due to its high thermal and electronic conductivity, biocompatibility, chemical stability, high wear resistance, and possibility of doping. However, the semiconductor properties of diamond, especially free-standing films, have not been fully explored. Nor have their integration with polymers and fragile materials and their applications as electronic components. In this thesis, the objective was the fabrication of heterostructures containing diamond films on flexible surfaces for application in electronic devices using the change of electrical parameters under the influence of external factors. To overcome this scientific challenge, boron-doped diamonds were grown using chemical vapour deposition on tantalum. After their delamination, the resulting free-standing films were investigated and analysed using Raman spectroscopy, Scanning and Atomic Force Microscopy, Nanoindentation Tests, Electrochemical measurements, and Electrical Evaluation as a function of temperature. Next, the diamond films were utilised for fabricating six heterostructures. Based on the conducted research, these heterostructures can be used as durable, transparent electrodes, strain sensors, Schottky or Ohmic junctions, capacitors, trinitrotoluene sensors, and as a protective layer for transistors.

STRESZCZENIE

Diament jest obiecującym materiałem dla elektroniki XXI wieku ze względu na wysoką przewodność cieplną i elektryczną, biokompatybilność, stabilność chemiczną, wysoką odporność na zużycie oraz możliwość domieszkowania. Jednak właściwości półprzewodnikowe diamentu, zwłaszcza samoistniejących warstw, nie zostały w pełni zbadane. Jak również ich integracja z polimerami, materiałami wrażliwymi i ich zastosowania jako elementów elektronicznych. W niniejszej pracy celem było wytworzenie heterostruktur zawierających warstwy diamentowe do wytwarzania elementów elektronicznych poprzez wykorzystanie zmiany parametrów elektrycznych pod wpływem czynników zewnętrznych. Aby udowodnić tezę, zsyntezowano diamenty domieszkowane borem metodą chemicznego osadzania z fazy gazowej. Powstałe w wyniku delaminacji warstwy były badane i analizowane przy użyciu spektroskopii ramanowskiej, mikroskopii sił atomowych, skaningowej mikroskopii elektronowej, testów nanoindentacji, pomiarów elektrochemicznych oraz elektrycznych. Następnie, warstwy diamentowe posłużyły do wytworzenia sześciu heterostruktur. Na podstawie przeprowadzonych badań, stwierdzono, że opracowane heterostruktury mogą być wykorzystane jako trwałe, przezroczyste elektrody, czujniki naprężeń, złącza Schottky'ego lub omowe, kondensatory, czujniki trinitrotoluenu oraz warstwy ochronne dla tranzystorów.

To follow the dream, and again to follow the dream – and – so always – usque ad finem...

Joseph Conrad (Józef Teodor Konrad Korzeniowski)

TABLE OF CONTENTS

THESIS OVERVIEW

Chapter 1 presents a brief overview of the state of the art related to the scope of this thesis. First, the basic properties of diamond compared to other crystalline materials are presented. Next, methods of obtaining semiconductivity, metallic like-behaviour, superconductivity through surface termination, doping, and strain are discussed. Afterwards, fabrication methods for free-standing diamond films are presented including wet and reactive etching, focused ion beam milling of a single-crystal diamond, and delamination. After pointing out manufacturing methods, the interactions of diamond with 2D materials and polymers are discussed. Finally, electronic and electrochemical systems using diamond films are presented.

Chapter 2 contains the objectives, hypotheses and outline of the research conducted in the framework of this dissertation.

Chapter 3 is dedicated to the results of the research on the fabrication of free-standing boron-doped nanocrystalline diamond films for application in electronic components. Their conductivity, carrier mobility and concentration, sp^3/sp^2 ratio, effect of doping on the nature of their conductivity, mechanical properties (including Young's modulus), absorption, topography, and electrochemical properties are fully analysed.

Chapter 4 presents the heterostructures: diamond-C:H:N:O, diamond-polydimethylsiloxane, diamond-polyimide, diamond-graphene, diamond-polylactic acid, and diamond-black phosphorus developed as a result of research on free-standing boron-doped nanocrystalline diamond films. Each of these structures finds a different application as durable, transparent electrodes, strain sensors, Schottky or Ohmic junctions, capacitors, trinitrotoluene sensors, and a protective layer for transistors.

Finally, **Chapter 5** contains the summary of the studies performed in this dissertation. Moreover, the directions for possible further research are also discussed.

LIST OF IMPORTANT SYMBOLS

A	surface area
C	capacitance
D	hopping distance
e	electron charge
E_A	activation energy
E_F	Fermi level energy
E_{FB}	flat band potential
E_G	bandgap energy
I	current
k	Boltzmann constant
N_A	acceptor concentration
N_D	donor concentration
$N(E_F)$	density of states at Fermi level
p	hole concentration
R	resistance
T	temperature
U	voltage
W	hopping energy
γ	measure of the extent of localised function
ϵ	permittivity
ϵ_0	permittivity of free space
ϵ_r	relative permittivity of diamond
μ	mobility
σ	conductivity
ϕ_B	Schottky barrier
ϕ_m	work function of metal
ϕ_s	work function of semiconductor
χ	electron affinity

LIST OF IMPORTANT ABBREVIATIONS

2D	two-dimensional
3D	three-dimensional
AFM	atomic force microscopy
BDD	boron-doped diamond
BP	black phosphorus
CVD	chemical vapour deposition
FBDDF	free-standing boron-doped diamond film
FDF	free-standing diamond film
FET	field-effect transistor
FIB	focused ion beam
G-PLA	graphene-polylactic acid heterostructure
G-PLA-NDF	graphene-polylactic acid-diamond heterostructure
GF	gauge factor
h-BN	hexagonal boron nitride
HPHT	high pressure, high temperature
PDMS	polydimethylsiloxane
PET	polyethylene terephthalate
PLA	polylactic acid
PPC	polypropylene carbonate
SEM	scanning electron microscopy
SIMS	secondary in mass spectrometry
SMU	source/measure unit
TNT	trinitrotoluene
VdW	Van der Waals

1. INTRODUCTION

Diamond is an interesting wide-bandgap material for future electronic and biosensing applications, because of its high Young's modulus [1], extreme wear resistance [2], high thermal conductance [3], chemical stability [4], high breakdown voltage [5], and possibilities of doping [6]. In the last century, the development of CVD technology has expanded the applicability of diamond films, because it became possible to deposit them on various 2D and 3D substrates at a relatively low cost [7]. Currently, they can be found on surfaces of optical fibres [8, 9], on dental burs [10], in drug delivery [11] and in electronic systems [12].

The most popular methods of diamond deposition are the HPHT (high pressure, high temperature) and CVD (chemical vapour deposition) processes. CVD, unlike HPHT, allows growth at low pressures. Moreover, it enables coverage of large areas on structured substrates [13]. During the process a plasma can be created using microwaves [14–16]. The chamber usually contains a carbon source, hydrogen and dopants. The presence of hydrogen atoms is essential during the process. It prevents the reconstruction of the surface, and etches sp^2 and sp phases [17].
When diamond is deposited on nondiamond substrates, the resulting film is polycrystalline [18]. Its properties depend on the process conditions including the temperature, pressure, and gas mixture. Based on the crystal size, polycrystalline diamond films can be categorised as:

- Microcrystalline (> 1000 nm)
- Nanocrystalline (10–100 nm)
- Ultrananocrystalline films (3–5 nm)

The size of the crystallites is related to the growth model. In the case of microcrystalline diamond, columnar growth consistent with the Van der Drift model can be applied, while continuous diamond renucleation is observed for utrananocrystalline diamond [19]. Polycrystalline diamond exhibits different properties compared to single-crystal diamond such as lower carrier mobility and fracture strength. A comparison of the properties of silicone, silicone carbide, gallium nitride, single-crystal and polycrystalline diamond is shown in Table 1.1.

Table 1.1. Properties of silicone, silicone carbide, gallium nitride, single-crystal and polycrystalline diamond [20].

Parameters	Si	SiC	GaN	Single-crystal diamond	Polycrystalline diamond
Bandgap (eV)	1.11	3.26	3.39	5.47	5.47
Lattice constant (Å)	5.42	4.36 (3C)	3.189 (a-axis)	3.57	3.57
Breakdown field (MV/cm)	0.3	3.5	3.4	1–2	-
Electron mobility ($cm^2/(V \cdot s)$)	1500	800	900	>2000	1800
Thermal conductivity (W/(cm·K))	1.5	4.9	2.2	>20	>19

Compared to other materials, polycrystalline and single-crystal diamond exhibit significantly higher electron mobility and thermal conductivity, enabling their use in high-frequency and high-power applications. The breakdown field value for single-crystal diamond is lower than that for SiC and GaN. However, this value is higher than that of commercially used silicone nowadays.

1.1. Semiconducting diamond

Diamond is characterised by sp^3 bonding, a cubic crystal structure and tetrahedral hybridization. Short C-C bonds are difficult to break and a large overlap of orbitals is present. As a result, the band gap of diamond is 5.47 eV (Table 1.1). Undoped diamond is a nonconductive material, but p-type conductivity can be induced by surface transfer doping [21, 22]. The carbon atom located at the surface of the crystal adsorbs species preventing the diamond surface from being graphitised. The most popular is hydrogen termination of the surface, which is usually achieved at the end of chemical vapour deposition growth. This method is used for the fabrication of field-effect transistors with a high cutoff frequency [23]. However, the channel of the transistor must be protected from oxygen. The negative charges cause a positive shift in the threshold voltage, leading to normal on-operation [24].

Another solution is to introduce dopants into the diamond lattice. The structures of undoped diamond, diamond with boron and diamond with phosphorus atoms are shown in Fig. 1.1.

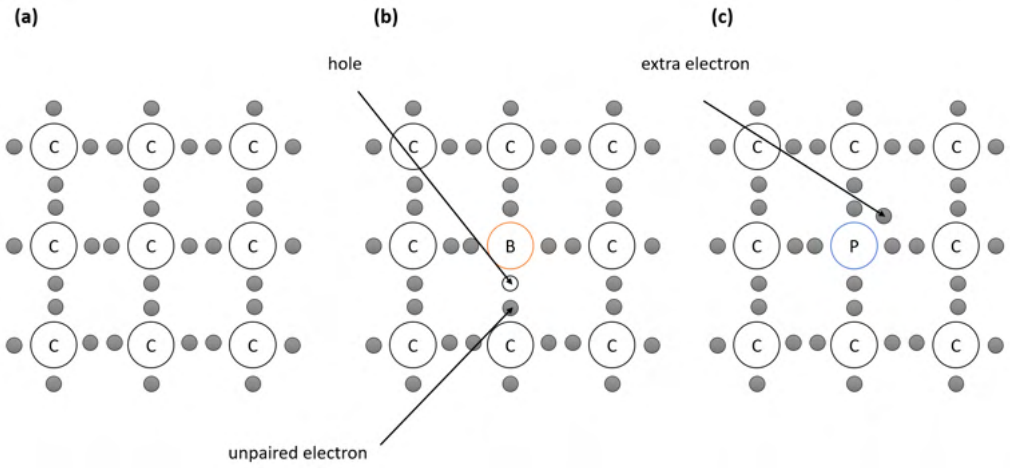

Fig. 1.1. Two-dimensional representation of the diamond crystal structure (a), with B-dopants (b), with P-dopants (c).

Each carbon atom is surrounded by four neighbours, as illustrated in Fig 1.1 (a). There are no free electrons to conduct electric current. When boron (group III) is introduced into the diamond structure, as shown in 1.1 (b), it creates a hole. The transfer of charge becomes possible. In the case of phosphorus, its atom in the diamond structure behaves as a donor. Introducing atoms is achieved by using the appropriate concentration of gases in the chamber during the CVD or ion implantation process [25, 26]. The energy band model of diamond doped with the different atoms is presented in Fig. 1.2. Nitrogen or phosphorus-doped diamonds present n-type behaviour, because nitrogen and phosphorus atoms act like donors with a donor level of 1.7 eV and 0.6 eV, respectively. The p-type diamond is based on low boron doping with an acceptor level at 0.37 eV.

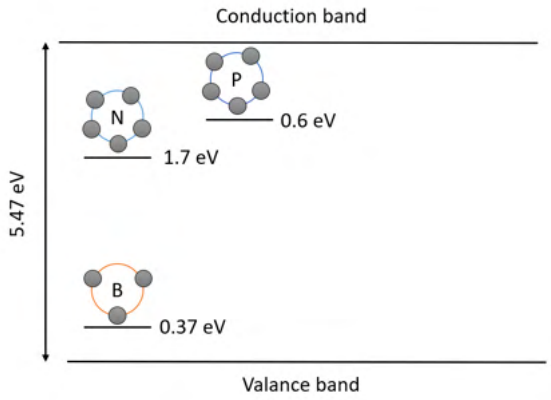

Fig. 1.2. Band gap states in diamond.

There are still difficulties in producing low-resistance n-type layer and high-quality n-type selective areas [27]. Ohmic contacts require high n-doping, which at present is hard to obtain and control at the desired level of doping [28, 29]. It should be easier to achieve the ohmic contacts using N-doping than P-doping, because nitrogen and carbon have almost the same covalent

bond lengths [30]. However, the deep donor level prevents nitrogen from being used at room temperature [31]. There is still the possibility of doping with sulphur and oxygen. Nevertheless, sulphur doping shows lower doping efficiency [32], and oxygen donors deactivate above 600℃ [33]. Another solution may be co-doping [34].

A comparison of the electrical properties of boron-doped and phosphorus-doped single-crystal diamonds is presented in Table 1.2.

Table 1.2. Effect of doping on the resistivity of HPHT synthetic diamond crystals.

	Boron-doped diamond [35]	**Phosphorus-doped diamond [36]**
Type	<111>	<111>
Concentration of dopants (atoms/cm^3)	$4.6 \cdot 10^{20}$	$10 \cdot 10^{20}$
Resistivity	5.8 mΩ cm	70 Ω cm

Despite the similar concentration of atoms in the structure of the diamonds, the resistivity of boron-doped diamond is more than an order of magnitude lower than that of phosphorus-doped diamond. It's worth adding that, in contrast to nitrogen or phosphorus doping, the CVD process can produce boron concentrations above 10^{21} cm^{-3} [35]. A higher concentration of boron increases the conductivity of the material but simultaneously causes a reduction in carrier mobility and an increase in defects in the diamond lattice. By changing the number of boron atoms, it is possible to shape the charge transport mechanisms, as shown in Fig. 1.3.

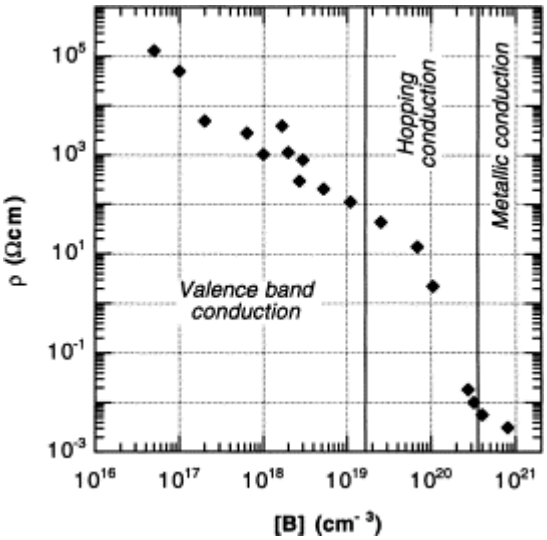

Fig. 1.3. Resistivity as a function of B-doping concentration at room temperature [37].

The contribution ([B]<10^{19} cm^{-3}) to the conductivity is associated with the motion of the holes in extended states of the valance band [38]. Between 10^{19} cm^{-3} and $3 \cdot 10^{20}$ cm^{-3}, the

conduction due to hopping transport between boron acceptor states is observed, while for heavily doped samples, metallic conduction is present [37].

1.2. Metallic-like behaviour and superconductivity of diamond films

When the boron doping increases, the Fermi level shifts towards the top of the valance band and the energy gap decreases compared to undoped film (Fig. 1.4). Additionally, the valance band peak for boron shifts towards higher energies and has a center at 41.10 eV [39]. A further increase in the doping allows the system to pass the metal transition and presents metallic-like behaviour. The impurity is merged with the conduction band [40] and the holes play a critical role in determining the metallic nature of diamond [41]. Thus, the Fano effect is observed in Raman spectra [35, 42]. Unfortunately, increasing the concentration of boron leads to a decrease in the activation energy of the holes [43]. The result is lower mobility. To solve this problem, nanometrically thick δ-doped layers are used [44, 45]. They are characterised by high boron content and high carrier mobility. The key factors are thickness, a high change in the boron concentration in the diamond lattice, and the interface between the δ-doped layer and the low-doped layer to minimise carrier scattering [43, 46]. To achieve this, the choice of process parameters such as methane concentration, pressure, and temperature presented later in this section is important [47].

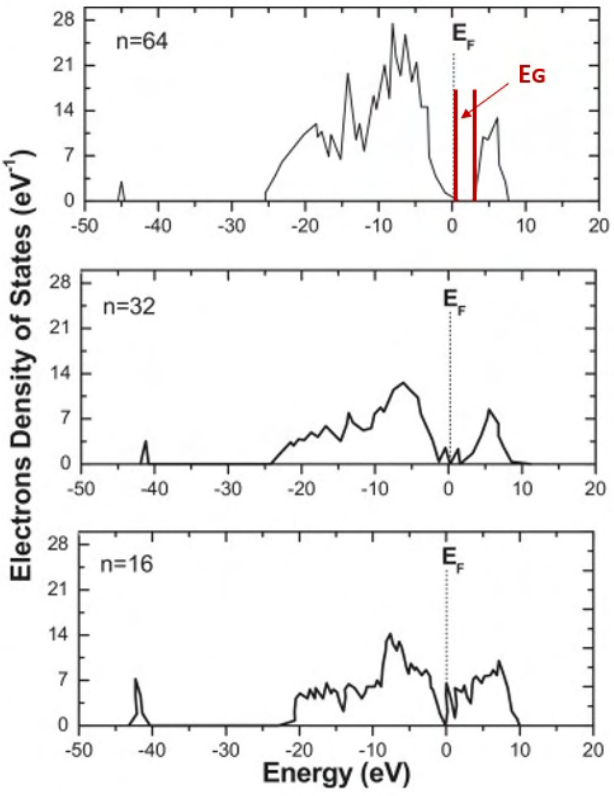

Fig. 1.4. Density of states of boron-doped diamond [39]. N is the total number of carbon atoms with one boron atom in the lattice. E_F represents the Fermi level, while E_G is the band gap of diamond.

In 2004, Ekimov et al. [40] discovered that highly-doped diamond is a superconductor with a superconducting transition temperature below 4 K. As a result, diamond layers can be used for the fabrication of superconducting resonators [48]. In 2021, Klemencic et al. [49] presented microbridges where the columnar crystal structure of boron-doped nanocrystalline diamond forms an intrinsic Josephson junction array that supports a line of phase slippage across the microbridge.

Another approach to obtaining semiconducting or superconducting diamond is strain engineering. In 2020, Liu et al. [50] performed numerical simulations which showed that a nondoped diamond can be a superconductor. The researchers performed compression-shear deformation, which induces increasing metallisation and lattice softening. The results of the deformation are shown in Fig. 1.5.

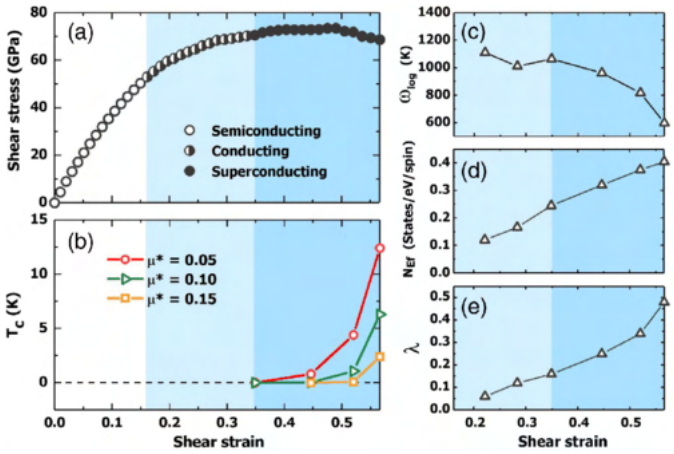

Fig. 1.5. (a) Semiconducting, conducting, and superconducting stages of deformed diamond indicated on the compression-shear stress-strain curve. (b) The critical temperature as a function of strain for a selected range of the Coulomb pseudopotential (μ^*). (c)–(e) Strain dependence of logarithmically averaged phonon frequency ω_{log}, electronic density of states at the Fermi energy $N(E_F)$, and electron-phonon coupling parameter λ [50].

For values above 0.161, strain completely closes the electronic band gap of diamond. However, increasing the strain within the range of 0.161-0.349 is not sufficient to produce a superconducting state with various critical temperatures determined by the Coulomb pseudopotential, as shown in Fig. 1.5(b). When the values exceed 0.349, the phonon frequency decreases (Fig. 1.5(c)), and the diamond demonstrates a high electronic density of states (Fig. 1.5 (d)) and high electron-phonon coupling (Fig. 1.5(e)), which allows it to behave as a superconductor. Shi et al. [51] performed a similar experiment for single-crystalline diamond nanoneedle using the finite element method. The results are presented in Fig. 1.6.

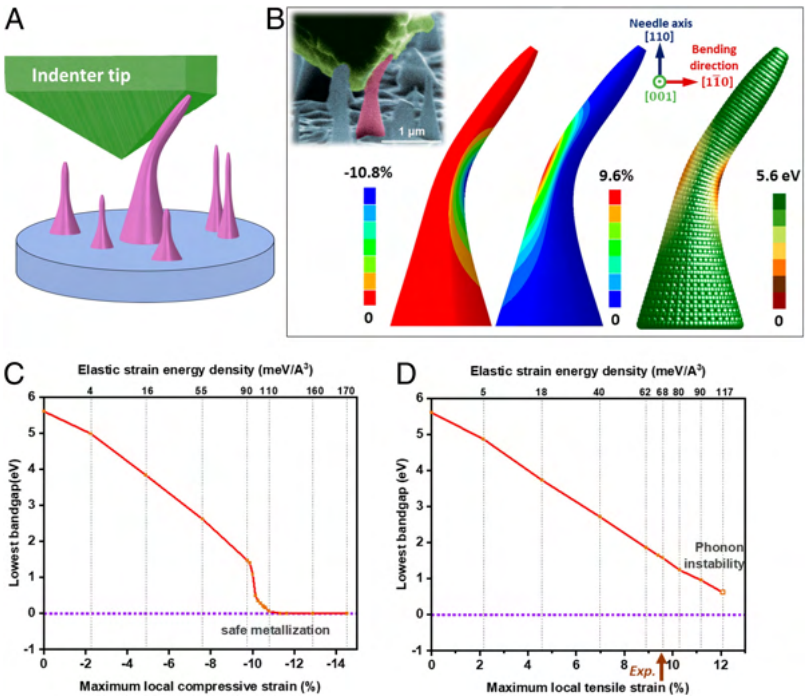

Fig. 1.6. Metallisation in diamond nanoneedles. (A) Schematic of the bending. (B) Finite Element Method predictions for a diamond nanoneedle with its <110> crystallographic direction aligned with the needle axis and a scanning electron microscope image of the deformed nanoneedle. (C) Bandgap of diamond decreases from 5.6 eV to 0 eV as a result of bending. (D) Fracture or graphitisation of diamond nanoneedle beyond 12.1% local tensile strain [51].

The metallisation appears on the side of the nanoneedle at a local strain of -10.8% (Fig. 1.6 (B)) [51, 52]. Moreover, diamond nanoneedles are able to withstand compressive and tensile strains of -10.8% ((Fig. 1.6 (C)) and 9.6% ((Fig. 1.6 (D)) respectively. However, these values can vary based on the crystal structures [53].

The properties of boron-doped diamond are not only determined by the level of the strain and dopants introduced during CVD growth, but also depend on the pressure, temperature, microwave power, and methane concentration. A high concentration of methane in the chamber reduces the transparency of the film and increases the sp^2/sp^3 ratio [54]. On the other hand, a low concentration can lead to a lower growth rate [55]. This significantly affects the crystal size and the number of grain boundaries [56]. In addition, it changes the incorporation of boron into the diamond lattice and shifts the critical temperature for superconductivity [57, 58]. During the growth process, increasing the temperature leads to a higher growth rate, but beyond a certain temperature, the growth rate saturates and may even decrease [59]. The precise temperature threshold depends on various factors, including the concentration of methane. The lowest temperature needed for growth is 350 ℃ and requires a linear antenna for induction plasma [60]. The concentration of species in the plasma and the underlying processes are also determined by the microwave power density and pressure [61]. Too much power and pressure leads to poorer incorporation of the dopants [62]. Higher power density results in faster growth rates [63], but this may come at the expense of the

quality of the diamond produced [56].

It is worth noting that after CVD growth, boron-doped diamond can be terminated with hydrogen, although other terminations are also possible, such as oxygen or fluorine termination using oxygen plasma or fluorine radicals, respectively. As a consequence, the adsorption energies are different as shown in Table 1.3.

Table 1.3. Average adsorption energies (eV per adsorbate) and adsorption energies (eV) for an otherwise 100% terminated surfaces [64].

Surfaces	Species	H	O on top	F
Undoped	Average	-4.34	-5.06	-4.58
	Last specie	-4.38	-4.90	-4.27
B-doped	Average	-4.28	-5.04	-4.52
	Last specie	-3.44	-4.28	-3.34

The results presented by Zhao et al. [64] in Table 1.3 show that the oxygen on top is the most favourable termination type.

In summary, diamond is an insulator that, through the introduction of dopants, surface termination or strain engineering, can become a semiconductor and even present metallic behaviour. It should be stressed that there is a lack of studies on the effect of strain on the conductivity of doped diamond. The combination of high conductivity and biocompatibility of boron-doped diamond should make it possible to produce modern, flexible junctions for electronics and biosensor applications. However, the surface termination of boron-doped diamond should be carefully examined. The choice of process parameters, such as pressure, temperature, microwave power density and dopant concentration, significantly affect the quality and conductivity of the diamond and are essential for producing properly functioning devices.

1.3. Diamond-based junctions

Due to limitations of the material's intrinsic properties, silicone-based electronic devices do not meet the requirements for future high-power, high-frequency and high-temperature applications [65]. Diamond is considered as a promising material for future electronic devices, because of its high breakdown field, high thermal conductivity and high carrier mobility. This chapter introduces the fabrication of contacts to diamond and the latest diamond transistors, junctions, and their applications.

1.3.1. *Electrical contacts for diamond devices*

Before implementing electronic devices, it is important to consider the methods of making contacts with diamond. The band structure of the Schottky metal-semiconductor junction is shown in Fig. 1.7 (a,b). For a p-type, semiconductor, when ϕ_m (work function of metal) < ϕ_s (work function of semiconductor), the band alignment at thermal equilibrium leads to a downward semiconductor band bending at the interface. Fermi levels are aligned. Furthermore, a so-called Schottky barrier forms at the metal-semiconductor interface, which is described by the equation:

$$\phi_B = \frac{E_G}{e} + \chi - \phi_m \tag{1.1}$$

where χ represents the electron affinity, E_G is the bandgap of the semiconductor, and e represents the elementary charge. However, this equation only applies for ideal junctions.

If $\phi_m > \phi_s$, an ohmic contact is formed, as shown in Fig. 1.7 (c,d). At thermal equilibrium, an upward bending of the semiconductor band at the interface due to hole accumulation is observed. According to Ohm's law, the current will increase linearly with the applied voltage, which is described by the equation:

$$I = \frac{U}{R} \tag{1.2}$$

where U is the applied voltage and R is the resistance.

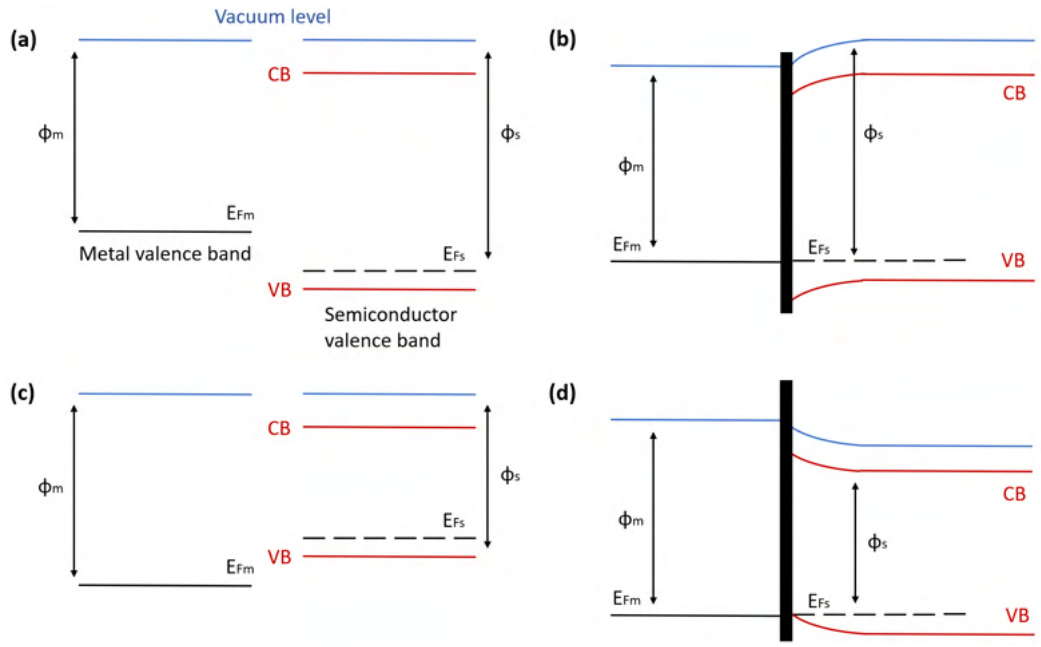

Fig. 1.7. Energy band diagrams of metal and p-type semiconductor contacts: (a) isolated metal and p-type semiconductor when $\phi_m < \phi_s$, (b) band alignment at thermal equilibrium when $\phi_m < \phi_s$, (c,d) when $\phi_m > \phi_s$.

Ohmic contact can be achieved using gold or carbide-forming metals [66, 67]. On the other hand, implementing of Schottky contacts may require the use of aluminium [68].

1.3.2. Diamond transistor and diodes

Diamond has been shown to work in various configuration as MESFET (Metal-Semiconductor Field-Effect Transistor) [69], JFET (Junction-Gate Field-Effect Transistor) [70], H-FET (Hydrogen-Terminated Diamond Field-Effect Transistor) [71], MOSFET (Metal-Oxide Semiconductor Field-Effect Transistor) [72], and BJT (Bipolar Junction Transistor) [73] as presented in Fig. 1.8.

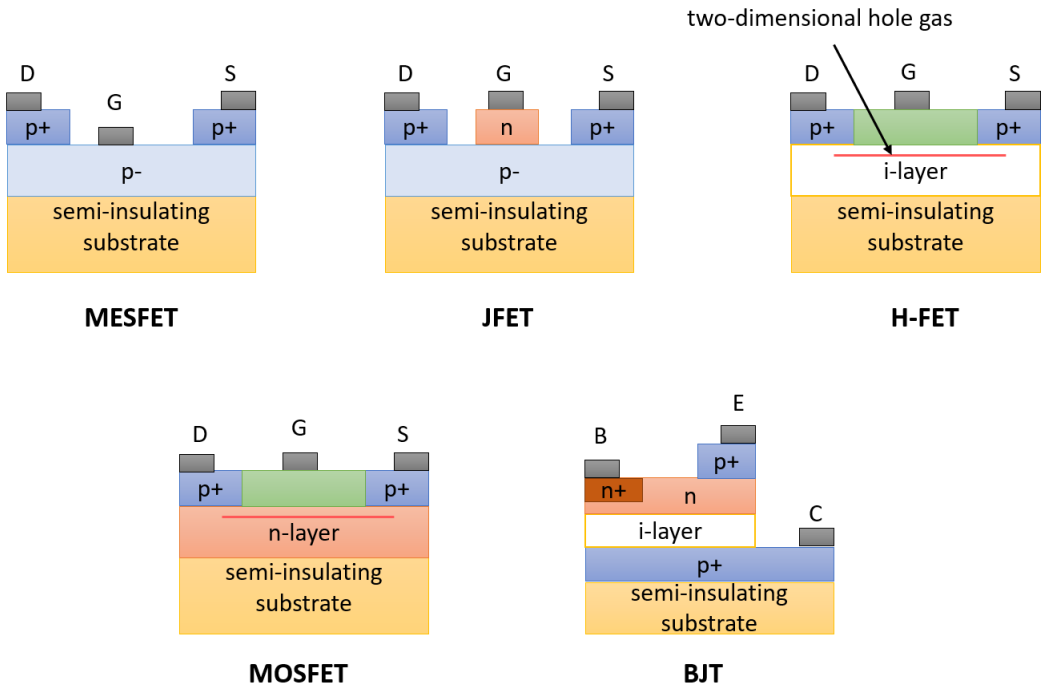

Fig. 1.8. Examples of single-crystal diamond transistor configurations [27]. Heterojunction bipolar transistors are also distinguished [74].

One of the most popular types of diamond transistors is hydrogen field-effect transistors. Hydrogenation can be achieved immediately after crystal growth, which speeds up the device fabrication process. Dankerl et al. [75] showed an array of transistors used to record action potentials from cells (Fig. 1.9 (a)). For this purpose, the researchers mostly used the single-crystal diamond. The transistors were coated with chemically stable SU-8 (photoresist) except for the active gate region (Fig. 1.9 (b)).

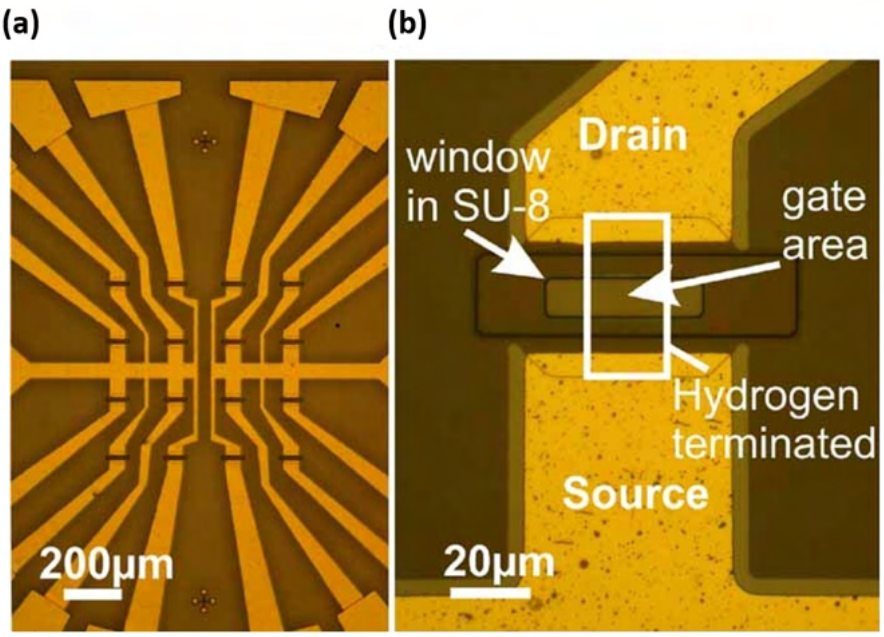

Fig. 1.9. Single-crystal FET array with the openings in the SU-8 [75].

P-type surface semiconductivity is also used for nanocrystalline diamond transistors. Ahmad et al. [76] fabricated an electrolyte-gated transistor that is able to detect human immunodeficiency virus type 1 trans-activator transcription protein and can be used as a biosensing platform. Moreover, hydrogen-terminated nanodiamond transistors can be used for the detection of glucose [77].

In the case of boron-doped diamond, FinFET-type transistors (commonly used in the silicone industry) can be fabricated [78], enabling high-power-density devices in radio-frequency and power electronics [79]. The structure presented by Huang is shown in Fig. 1.10 (a). FinFETs consist of two heavily boron-doped diamond layers as the drain and source above a lightly doped layer (Fig. 1.10 (b)). A Fin is created between the drain and source. As shown in Fig. 1.10 (c,d), the device exhibits an on/off ratio of over 3000 and a gate current modulus below 1 nA at a gate voltage of -12 V. Additionally, diamond-like carbon layers can also be used as a gate-dielectric [80].

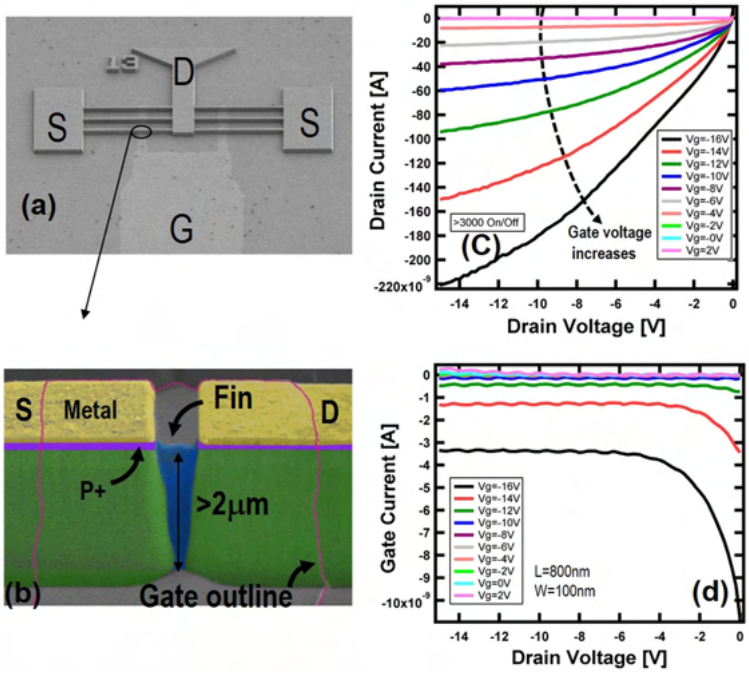

Fig. 1.10. (a,b) SEM images of a diamond FinFET (channel length is 800 nm). (c) Output characteristic. (d) Gate leakage versus drain voltage as a function of gate voltage [78].

Diamonds can be used for unipolar (pseudo vertical Schottky barrier, vertical Schottky barrier, Schottky p-n junction, metal-intrinsic-p type) and bipolar (PiN) diodes as well [27]. Breakdown voltages above 10 kV can even be obtained [81]. An example of a p-n junction that uses a single-crystal diamond membrane is shown in Fig. 1.11.

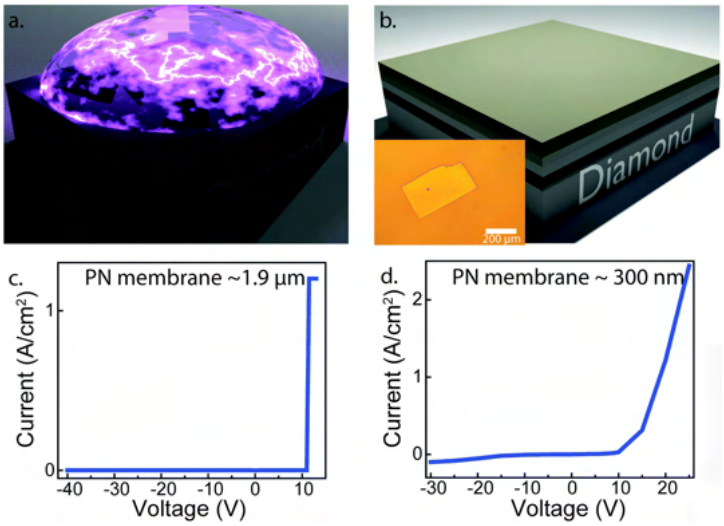

Fig. 1.11. (a, b) Bulk boron-doped diamond that was implanted with He ions is overgrown to create a phosphorus-doped layer represented by dark green in (b). An I–V curve of 1.9 μm thick (c) and 300 nm thin (d) p-n membrane [82].

The n-type layer is grown on top of the p-type diamond (Fig. 1.11 (a)). Phosphorus is used as a dopant during the CVD process. The devices (Fig. 1.11 (b)) exhibit diode-like behaviour with a forward threshold voltage of approx. 10 V. The forward voltage and rectification ratio can be altered

by adjusting the thickness of the diamond membrane (Fig. 1.11 (c,d). It is worth mentioning that the use of diamond p-n junctions enables the fabrication of ultraviolet light-emitting diodes [83].

1.4. Diamond versus two-dimensional materials

In recent years, there have been significant developments in two-dimensional materials technology. These materials are characterised by intralayer covalent and interlayer van der Waals (vdW) bonding [84]. Shaping their energy gap can be done by changing the thickness. A comparison of the properties of selected 2D materials and diamond is presented in Table 1.4. Black phosphorus and molybdenum disulphide show lower values of thermal conductivity and carrier mobility compared to single-crystal and polycrystalline diamond. Hexagonal boron nitride has a higher energy gap and can be used as a substrate for graphene [85]. However, 2D materials are thinner than the continuous diamond films produced today.

Table 1.4. Properties of 2D materials and single-crystal, polycrystalline diamond [20, 86–96].

Material	**Bandgap (eV)**	**Thermal conductivity (W/(m·K))**	**Carrier mobility (cm^2/(V·s))**	**Superconductor**
Graphene	~0	~5000	<4000	twisted
Black phosphorus	0.3–2.00	~60	10,000	under high pressure
Molybdenum disulphide	1.3–1.90	131	200	requires doping
Hexagonal boron nitride	~6	~550	-	-
Single-crystal diamond	5.47	>2200	>2000	boron-doped or bended
Polycrystalline diamond	5.47	>2200	1800	boron-doped or bended

Graphene deserves special attention due to its high thermal conductivity [97], high carrier mobility [98] and mechanical strength [99]. Unfortunately, graphene is a near non-zero bandgap material. As a result, a small on-off ratio for a transistor is observed [100]. One way to overcome this problem is to use a suitable substrate for graphene. Diamond has better thermal conductivity, larger optical phonon energy and a potentially lower surface trap density than SiO_2 [101–103]. In 2015, Zhao et al. [104] proposed a graphene transistor on nanodiamond particles. The schematic diagram is presented in Fig. 1.12 (a), while the SEM and FIB images are presented in (b) and

(c). The carrier mobility increased by 60% compared to the transistor on siliconee dioxide. Higher stability was also obtained. Nevertheless, the shorter gate device (Fig. 1.12 (d)) shows lower gate modulation compared to the longer gate device (Fig. 1.12 (e)) due to the dominant role of the contact resistance [104, 105].

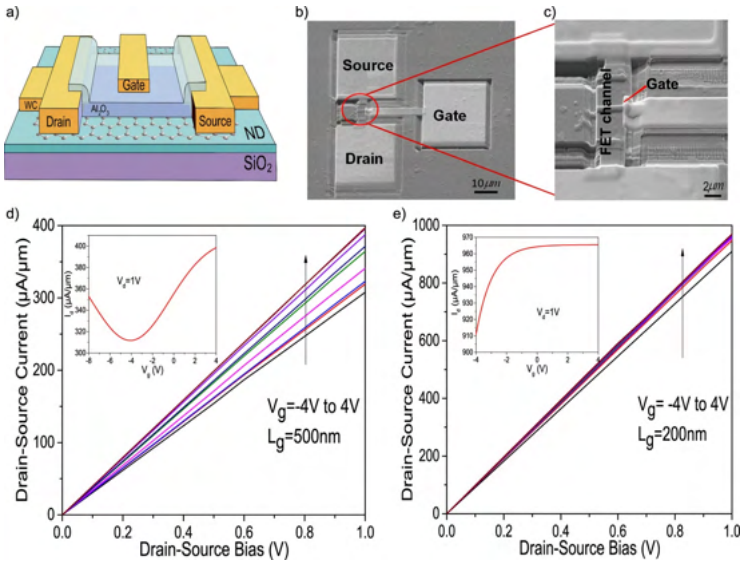

Fig. 1.12. Fabrication and output characteristics for graphene FET on H-terminated nanodiamonds. (a) Schematic drawing (b) SEM and (c) Focused ion beam image. Output characteristics of a 500 nm device (d) and a 200 nm device (e) [104].

In the case of the direct transfer of diamond nanoparticles to the graphene surface, it is possible to obtain a significant magnetoresistance effect at low temperatures (< 100 K) [106]. However, the increasing resistance of the material is observed. Graphene-diamond systems can also behave as photomemristors. Ueda et al. [107] presented a graphene-on-diamond junction with multiple resistance states and nonvolatile memory functions. The resistance state can only be switched by a specific irradiation. Similar properties were observed for carbon nanowall-diamond junctions [108]. Moreover, arrays fabricated from graphene-diamond junctions can act as image sensors that could provide an optical memory function and selectively memorize information depending on the relative importance of the data [109]. An example of a photomemristor, its Raman spectra and current-voltage characteristics are presented in Fig. 1.13.

A low resistance state can be obtained with a positive bias, while a high resistance state should be generated upon photoirradiation together with a negative bias as show in Fig. 1.13 (a) [109]. In order to fabricate a photomemristor, vertically aligned graphene is deposited on diamond (Fig. 1.13 (c–d)). The contact to graphene was made from Ni, while for diamond – Cu/Ti.

A technology that combines materials with different hybridizations (in particular, sp^3-sp^2) may find applications in photoelectric conversion [110] and highly spin-polarized states [111]. Direct graphenization of diamond is also possible [112]. The key factors influencing the quality of the

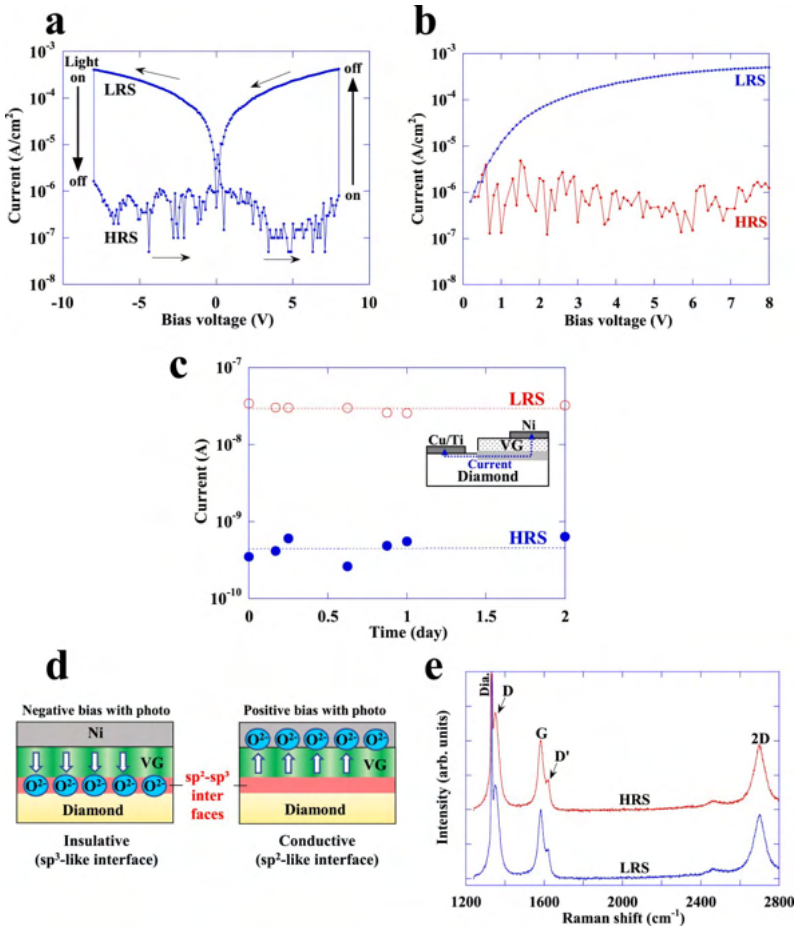

Fig. 1.13. Current-Voltage (IV) characteristic of a graphene-diamond junction in response to (a) photoirradiation and (b) dark conditions, where HRS represents the high resistance state and LRS represents the low resistance state. (c) The current retention properties were also analysed. (d) Diagram illustrating how the heterostructure works. (e) Raman spectra of the junction [109].

formed junction are the doping and termination of the diamond surface [113]. Wan et al. [114] showed that graphene causes strong band bending at the hydrogen-terminated diamond surface, lowering the binding energy of the valence band by approx. 150 meV. Furthermore, the lattice defects induced by the dopants favour a more pronounced charge transfer between graphene and diamond [115]. The proper choice of doping can also result in the formation of a graphene layer on the diamond and a better interface between the structures [116]. It should be noted that studies on interactions between boron-doped diamond and graphene are marginally reported in the literature.

Research on the interactions of diamond with other two-dimensional materials are also present in the literature. Kim et al. [117] presented the conjugation of diamond with molybdenum disulphide to achieve higher electrochemical capacitance. Sasama et al. [118] fabricated a high-mobility diamond field-effect transistor with a monocrystalline h-BN gate dielectric (> 300 cm^2 $V^{-1}s^{-1}$), while Vishwakarma et al. [119] reported cubic boron nitride grown on polycrystalline and single-crystal diamond substrates. Recently, Dettlaff et al. [120] combined boron-doped diamond with phosphorene enabling electrochemical studies of the 2D material at high anodic potentials.

Micromechanically exfoliated black phosphorus has gained significant attention recently for its high carrier mobility [96], optical anisotropy [121], efficient electrical control of the bandgap [122], and ambipolar behaviour [123]. However, black phosphorus is not stable under ambient conditions [124] and requires protective methods.

In summary, diamonds can regulate electronic properties and serve as a platform for 2D materials. Their use enhances carrier mobility, changes magnetoresistance, capacitance, and electrochemical properties. However, the interactions with boron-doped diamonds are not yet fully understood and require additional studies.

1.5. Fabrication of free-standing diamond films

Fabricating structures using fragile materials that are not heat resistant is more challenging due to the high temperatures required for diamond growth in a hydrogen-rich plasma (even using a CVD system) [125]. To solve this problem, free-standing diamond films (FDF) can be used. FDF is a thin layer of diamond, whether single-crystal or polycrystalline, that is not attached to any substrate or support material. This subsection presents six methods of fabricating free-standing diamond using:

- Delamination – diamond film detaches from the substrate as a result of a mismatch in the thermal expansion coefficients between the materials (Fig. 1.14 (a))
- Wet selective etching – liquid etchants are used to partially remove the substrate on which a diamond film grows (Fig. 1.14 (b))
- Reactive ion etching – liquid etchants are replaced by plasma (Fig. 1.14 (c))
- Focused ion beam milling of single-crystal diamond – a high energy ion gun removes part of a single-crystal diamond (Fig. 1.14 (d))
- Laser stripping – a type of laser cutting (Fig. 1.14 (e))
- Rolling-up technology – a combination of wet selective and reactive ion etching to achieve self-rolling diamond (Fig. 1.14 (b,c)).

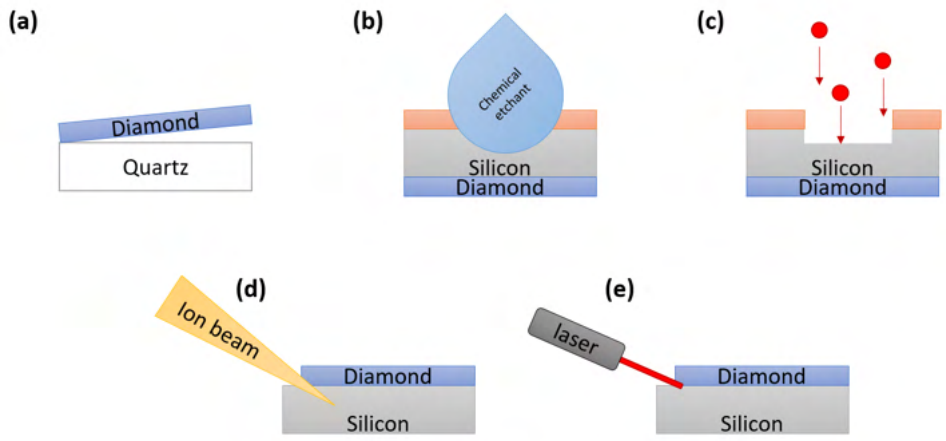

Fig. 1.14. Various methods for fabricating free-standing diamonds.

The first presented method to manufacture diamond nanosheets was developed by Seshan et al. [126]. First, a diamond film is grown on quartz (Fig. 1.15). Due to a mismatch in the thermal expansion coefficient between the quartz and the diamond layer, the carbon film delaminates from the substrate, as shown in Fig. 1.15 (a). Consequently, the diamond film can be transferred in the same way as typical 2D materials [127]. To achieve this, the fabricated diamond on PDMS (Fig. 1.15 (b)) is transferred onto the desired substrate (Fig. 1.15 (c)) and then the PDMS is removed (Fig. 1.15 (d-h)). Due to van der Waals forces, the diamond film remains on the desired substrate. A disadvantage of the solution proposed by Seshan et al. [126] is the low purity of the resulting material due to the residual presence of PDMS on the diamond film after the transfer. To reduce polymer contamination, polypropylene carbonate can be used [128].

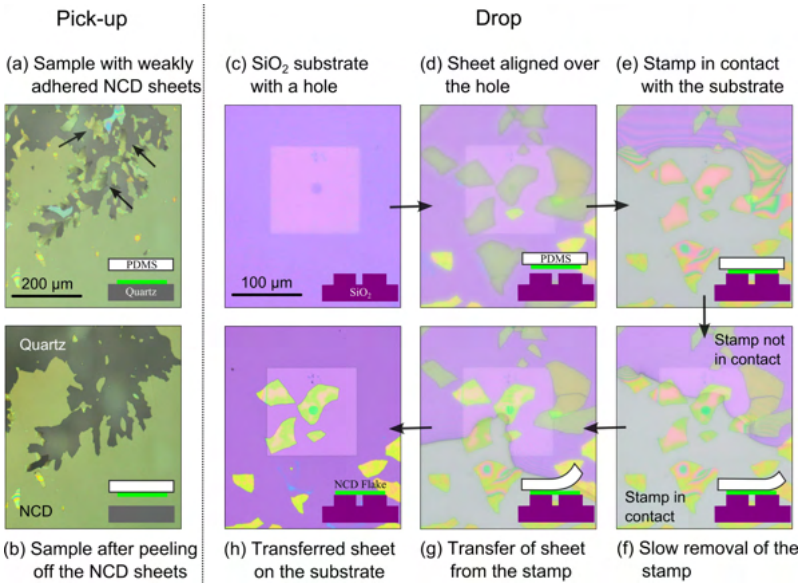

Fig. 1.15. Pick-up and drop transfer of diamond nanosheets [126].

The manufacturing of free-standing diamond films is also possible by wet selective etching. For this purpose, silicone and chromium can be used [129, 130]. Janssens et al. [131] presented the fabrication of ultra-thin nanocrystalline diamond membranes using patterned diamond film deposited on quartz (Fig. 1.16 (1–2)).

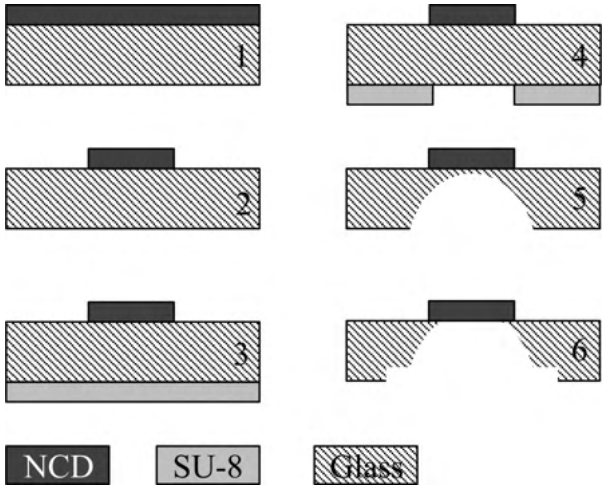

Fig. 1.16. Fabrication of free-standing diamond sheets using wet selective etching [131].

The etching procedure requires the use of a mask, as shown in Fig. 1.16 (3–4). In the presented paper, the researchers used SU-8 (commonly used photoresist). The quartz is etched in areas not covered by the resist (Fig. 1.16 (5)). This method requires low-temperature diamond growth and deep etching of the substrate. However, it should allow conductive membranes to be manufactured [54].

Another approach allowing for the fabrication of thin free-standing diamond films is reactive ion etching. The fabrication of a free-standing germanium-doped diamond film is presented in Fig. 1.17 [132]. In the first step, GeO_2 powder in ethanol was deposited on sapphire (Fig. 1.17 (a)). Next, CVD growth was performed (Fig. 1.17 (b)). During the process, the incorporation of the germanium atoms from a piece of solid germanium, laying close to the sample, into the diamond lattice occurred. Then, undoped diamond, which served as the substrate for the germanium doped diamond, was etched using reactive ion etching in the presence of oxygen and SF_6 (Fig. 1.17 (c)). As a result, free-standing single-crystal diamond films with a thickness of 300 nm were obtained (Fig. 1.17 (d)). SEM micrographs of the overgrown and the thinned free-standing diamond film are shown in Fig. 1.17 (e–f), while the surface roughness is shown in (g).

In 2021, Dang et al. [133] showed a flexible microfabricated diamond. For the fabrication, the researchers used a focused ion beam on a single-crystal diamond. Fig. 1.18 (A)–(E) show transmission electron microscope images of the fabricated single-crystalline diamond bridge structures with lengths of approximately 100 nanometres and 1 micrometre. The thickness is approximately 200 nm. The study suggests that an indirect-direct bandgap transition is possible

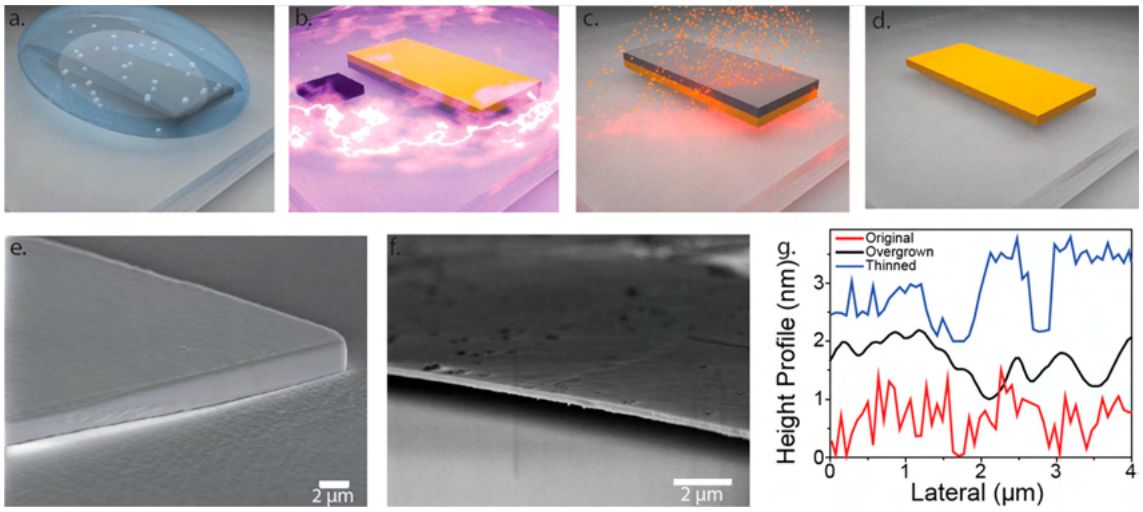

Fig. 1.17. Fabrication process of single-crystal diamond membranes containing GeV colour centres. (a) Single-crystal diamond membrane (dark grey) is transferred to a sapphire substrate using a solution containing GeO_2. (b) CVD growth with germanium source. (c) Removing the original diamond not containing colour centres. (d) Diamond membrane with GeV centres. (e, f) SEM images of the overgrown and the thinned diamond membrane. (g) AFM scans of the surface roughness [132].

with a tensile strain larger than 9% along the <111> direction. The samples were subjected to strains ranging from 6.5% to 8.2% with full recovery along the <100>, <101>, and <111> directions. The strain distribution of the diamond bridge at the critical geometry is presented in Fig. 1.18 (F), while the nearly linear elastic response is shown in (G). The loading-unloading photos from the study and recovered samples are shown in (H) and (I–J), respectively. The results of the finite element method simulation reproducing the experiment are shown in (K).

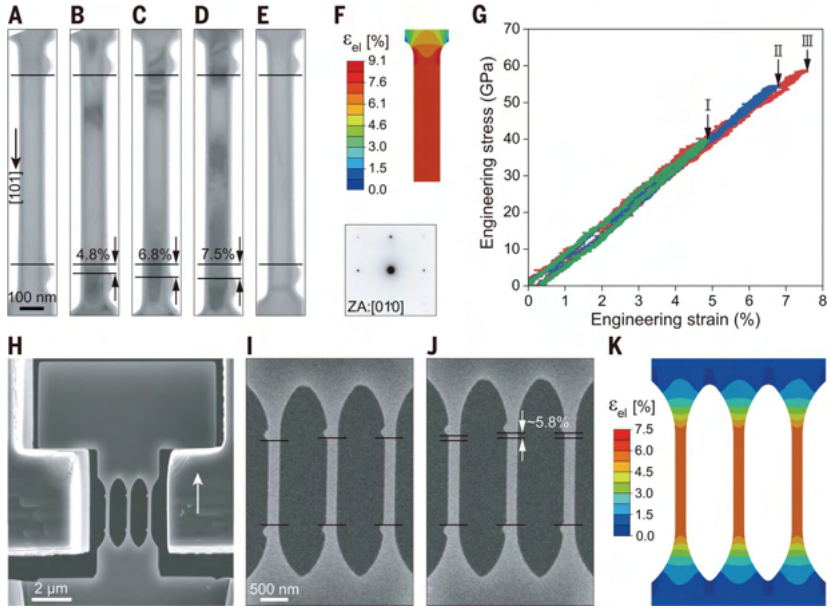

Fig. 1.18. Loading-unloading tensile experiments on single-crystal diamond films fabricated using a focused ion-beam. (A–E) Transmission electron microscope images of single-crystalline diamond bridges. (F) Elastic strain distribution at the critical geometry. (G) Stress as a function of the strain of multi-cycle loading-unloading measurements. (H) Tensile straining of the diamond bridges. (I-J) Recovered samples after tests with a maximum 5.8% tensile strain. (K) Uniform elastic strain distribution along the tensile direction [133].

Another method of fabricating diamond films is laser stripping. Flexible nanocrystalline diamond foils with high hardness (> 70 GPa) and very low thermal conductivity (< 1 W/mK) with thicknesses of up to 100 µm can be produced [134]. Their main advantage is high reliability. An ultrasonic bath is used after application of the laser to weaken the adhesion between the diamond and silicone substrate [135].

In recent years, rolled-up nanotechnology has been developed [136, 137]. It can find applications in lab-in-a-tube [138], optical microcavities [139], and energy storage [140]. In 2017, Tian et al. [141] presented self-rolling ultrathin nanocrystalline nanomembranes (Fig. 1.19).

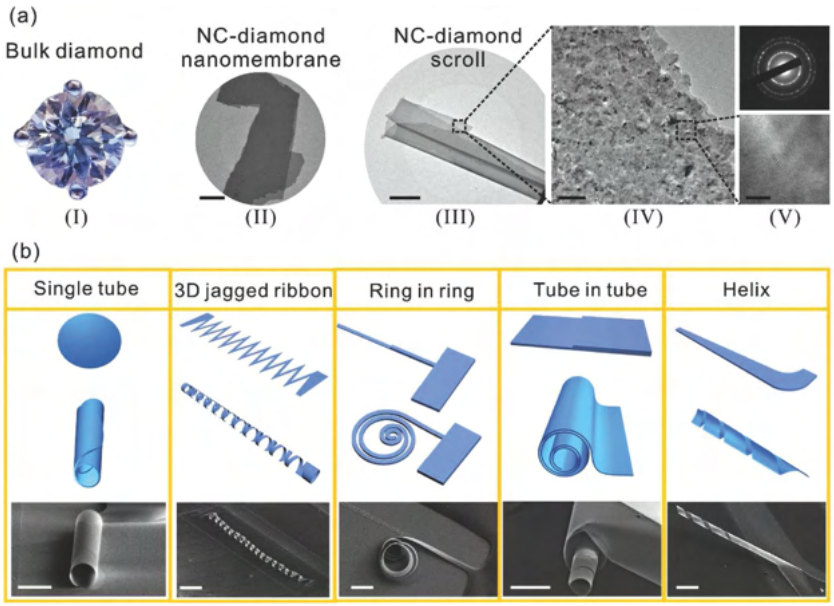

Fig. 1.19. (a) Self-rolling geometries. (I) Optical image of bulk diamonds. (II–V) SEM and TEM images of diamond structures. Scale bars: II) 10 µm, III) 5 µm, IV) 100 nm, and V) 2 nm. (b) 2D patterns, 3D predictions, and SEM images. Scale bars: 10 µm [141].

The fabrication of rolled-up diamonds requires a combination of reactive ion etching and wet etching. In the first step, CVD diamond grown on silicone dioxide is coated with a patterned photoresist. Then the nanocrystalline diamond and SiO_2 are etched in the areas not covered by the resist using reactive ion etching. Finally, the sample is immersed in a hydrofluoric acid solution. The self-rolling is a result of the intrinsic stress gradient. A free-standing diamond film is presented in Fig. 1.19 (a)-II, and curved in (a)-III, respectively. Fig. 1.19 (a)-(IV,V) reveal the nanocrystalline structure of the fabricated films. All fabricated rolled-up structures are presented in part (b) of Fig. 1.19.

Free-standing diamond films offer new opportunities for the fabrication of electronic devices. It becomes possible to utilise the top surface (growth side) and nucleation side (Fig. 1.20). These two surfaces present different mechanical, morphological, electrical, and electrochemical properties [142–145]. The nucleation side is smoother (Fig. 1.20 (a)) because it is in direct contact with the substrate during growth (Fig. 1.20 (b)) and has fewer boron atoms, as illustrated in Fig. 1.20 (c,d).

Oxygen is present at the beginning of the diamond growth due to chamber contamination. This oxygen is present due to the necessity of opening the chamber during sample insertion. Although low pressure is maintained at the start of the CVD procedure, some oxygen still remains in the chamber. Over time, its concentration decreases during CVD growth. As a result, the nucleation side exhibits a different electrochemical response and electrical conductivity compared to the growth side [146]. The two sides also differ in the sp^3/sp^2 phase ratio [143]. Hence, the choice of the layer in direct contact with the 2D material, whether it be polymer or solution, is critical for the fabrication of electronic devices.

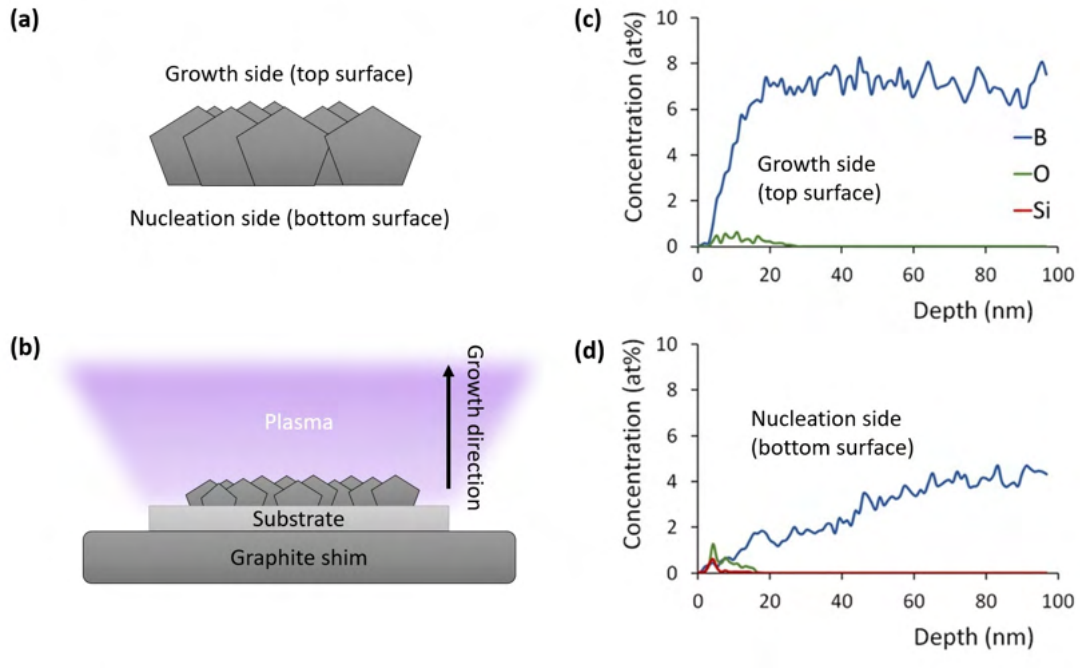

Fig. 1.20. (a) Two sides of a free-standing diamond film after delamination and (b) schematic diagram of diamond film during CVD growth. Concentrations of boron, oxygen, and silicone for the different sides of a boron-doped diamond thin film: (c) the growth side, (d) the nucleation surface. Figs. (c) and (d) were obtained from [147].

In summary, the development of FDF should enable a new form of integration of diamonds with materials that are not heat resistant. However, the process of making these films is more complicated and time-consuming than the growth of the diamonds themselves. Each method has its own advantages and disadvantages. Wet selective etching and reactive ion etching, if carried out for too long, can cause cracks. In addition, wet selective etching requires the use of hazardous chemicals. Reactive ion etching and focused ion beam milling of single-crystal diamond are expensive because they require specialized equipment. Laser stripping cannot produce very thin layers. Diamond delamination is straightforward and less time-consuming, but residues of the materials on which they were deposited may be present in the diamond structure. It should be noted that the fabrication of FDF enables the utilisation of the nucleation side, which is usually characterised by a higher concentration of the sp^2 phase and has a smoother surface.

1.6. Integration of diamond films, powders, particles with polymers

The utilisation of free-standing diamond films enables improved integration with polymers, which can lead to the development of flexible electrical and sensing devices. The integration of diamond with polymers can take various forms, including:

- Chemical Bonding – Diamond particles can be chemically bonded to a polymer.
- Mixing – Nanodiamond particles are physically mixed with a polymer.
- Dispersion – Particles are dispersed through a dispersant to avoid agglomerations.
- Coating – Diamond film coats a polymer surfaces.

Diamond allows for different materials to be attached to its surface using chemical bonds. During this process, electron transfer can occur as a result of the broken bond. Diamond particles or films can also be mixed with resins to improve their electrical, mechanical and thermal management properties. However, in this case it is important to have the correct concentration of the nanoparticles and polymer so the entire structure can conduct current. Additionally, dispersion is used to avoid agglomeration. The fabricated diamond films can also be transferred directly to various polymers enabling their application in electrochemistry, flexible electronics, and medicine [11, 148, 149]. In this case, a polymer usually serves as a substrate for a diamond film, which participates in charge transfer between the diamond and electrolyte/material.

The first structure presented in this subsection is diamond-PDMS (polydimethylsiloxane), which can be used as a microfluidic system for the electronic monitoring of cells (Fig. 1.21). Gold layers are used to create electrical contacts and serve as the counter electrode. Babchenko et al. [150] were able to culture HeLa cells (human cell line) in the diamond-PDMS channel. The system exhibits stable adhesion and electrical sensitivity to the adsorption of bovine serum albumin.

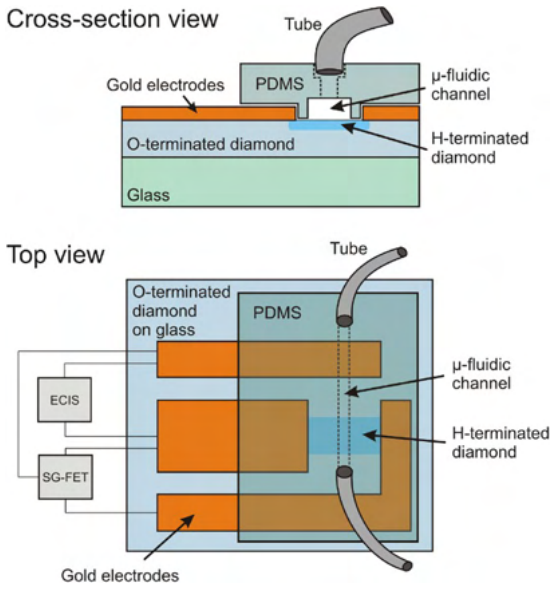

Fig. 1.21. Schematic drawing of diamond-PDMS microfluidic system [150].

PDMS and PET (polyethylene terephthalate) can also be used as flexible substrates for dopamine sensing using thin diamond [151]. The detection is performed on the diamond surface. Fan et al. [152] present implementing flexible sensors that are suitable for neurotransmitter sensing (Fig. 1.22).

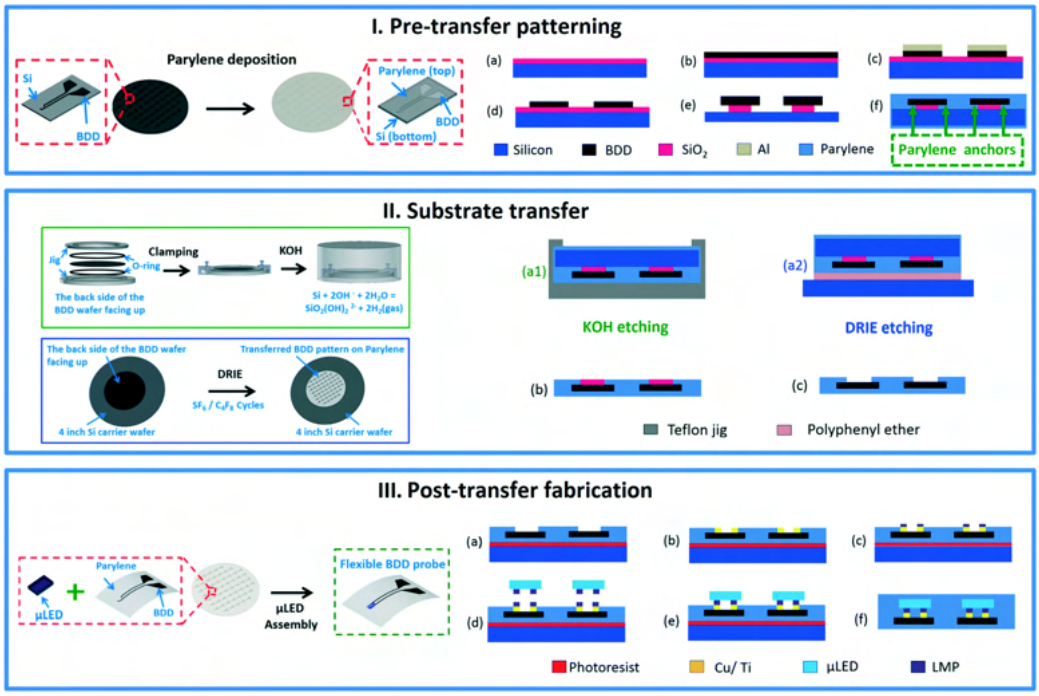

Fig. 1.22. Fabrication of flexible neurotransmitter sensor: I. pre-substrate transfer patterning; II. substrate transfer, and III. post-transfer fabrication [152].

The fabrication of a neurotransmitter sensor in this case involves three steps:

- Patterning – Parylene-C coats the patterned diamond electrode (Fig. 1.22 I)
- Transfer – silicone and silicone dioxide are removed using wet etching and deep reactive ion etching (Fig. 1.22 II)
- Post-transfer fabrication – for exposing selected parts of the chip (Fig. 1.22 III)

The fabricated device has a wider potential window and smaller double layer capacitance compared to gold electrodes, enabling a higher signal-to-noise ratio and detection of a wider range of substances. A combination of diamond and other polymers is also possible. The surface of BDD electrodes can be modified by Nafion film (conductive polymer) to enhance the current response and sensitivity [153]. The electrode coating is obtained by applying the solution onto the diamond surface. As a result, a linear response for detecting caffeine can be achieved in a range from 2.0 $\cdot 10^{-7}$ to 1.2 $\cdot 10^{-5}$ M [154]. Bergonzo et al. [155] were able to prepare diamond-based retinal implants on polyimide and parylene, while Hess et al. [156] fabricated diamond electrodes on a polynorbornene-based substrate. Due to the current development of 3D printing technology, diamond microparticles are mixed with commercially available acrylate resin. As a result, the printed

composites exhibit improved heat transfer rates and significantly decreased thermal expansion coefficients compared to the unmodified resin [157]. Moreover, 3D printable composites consisting of boron-doped diamond are utilised for printing humidity sensors [158]. The fabrication of the humidity sensor takes only 2 minutes.

To conclude, diamond films, powders and particles allow integration with polymers, which is achieved through chemical bonding, mixing, dispersion, and coating. Such heterostructures have potential applications in detecting chemical compounds and cells, microfluidic systems, and even as humidity sensors. Some applications may require post-transfer fabrication steps to remove residues from the diamond surface.

1.7. Diamond film as an electrochemical sensor

Diamond provides unique electrochemical properties such as:

- Wide potential window for aqueous (~3–3.5 V) and non-aqueous (~5.0–7.5 V) media [159]. As a result, the voltage range over which the electrochemical system operates is wider and more stable. For this range, there are no electrolyte decomposition reactions.
- Low background current [160], also called non-Faradic, it is the flowing current between electrodes when no electroactive species have been added and no electrolyte decomposition is observed [161].
- Biocompatibility [162, 163] is commonly defined as the ability of a material to exist in contact with the tissue of the human body without being harmful or toxic [164].
- Tunability through the boron concentration [146]. The current density and potential windows are shaped via doping.
- Fast response [165, 166]. The time to detect a pathogen, substance, etc. is short.
- Low absorbance is observed from 225 nm to the microwave range and beyond, with slight absorption occurring between 2 and 6 μm [18]. Direct electrochemical and optical measurements are possible.

The above properties and studies on diamond thin films [133] suggest that diamond may find applications as a flexible electrochemical sensor. At the time the experiments began (ca. 2018), no reports existed of high-area electrochemically active free-standing boron-doped diamond films being fabricated and transferred to a flexible polymer substrate. However, free-standing diamond films were used for sensing applications. Liu et al. [167] was analysing the role of sp^2 carbon in the non-enzymatic electrochemical sensing of glucose. The nucleation side of free-standing single-crystal boron-doped diamond showed the highest sensitivity, which can be attributed to its higher sp^2 content, which catalyses glucose oxidation. Gao et al. [168] presented that highly boron-doped diamond membranes can be applied as an electrochemically switchable filter. The

organic compound is decomposed via oxidation at positive potentials, while heavy metal ions can be trapped on the filter via electrochemical reduction. Moreover, diamond membranes are used for protein extraction [169].

The idea behind the operation of sensors utilising boron-doped diamond is presented using the work by Nidzworski et al. [165]. The manufacturing procedure and the method of obtaining a swab are presented in Fig. 1.23. The fabricated device enables the detection of the biomarker of influenza, which is present in saliva, through a change in electrochemical impedance of the entire structure, as shown in Fig. 1.23 (A).

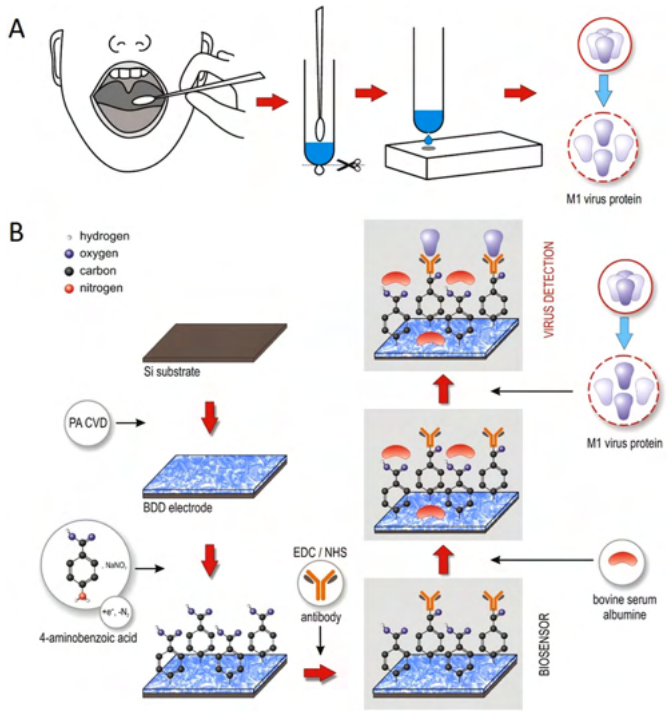

Fig. 1.23. Biosensor for influenza virus detection. (A) Acquiring throat swab cultures. (B) Boron-doped diamond electrode surface modification, which serves to identify the biomarker for influenza virus (the M1 protein) [165]

After the diamond growth, a linker in the form of an adhesive monolayer of 4-aminobenzoic acid is attached to its surface as shown in Fig. 1.23 (B). Anti-M1 antibodies are then captured, followed by the application of bovine serum albumin to close open areas and eliminate the immobilisation of antibodies. A virus protein attaching blocks the efficient transfer of electrons between the electrode and redox-active species in the electrolyte, resulting in a change in impedance. The response time of this sensor is only 5 minutes.

Observing the change in the recorded current generated by the oxidation/reduction of a compound at a certain potential value makes it possible to determine the concentration of this compound in the solution as well. For this purpose, boron-doped diamonds are used [170, 171]. An example of the simultaneous detection of mefenamic acid and indomethacin is presented in Fig. 1.24. Mefenamic acid and indomethacin belong to non-steroidal anti-inflammatory drugs, which is

one of the most frequently prescribed drug types [172], therefore analysis of their concentration in pharmaceutical formulations is very important.

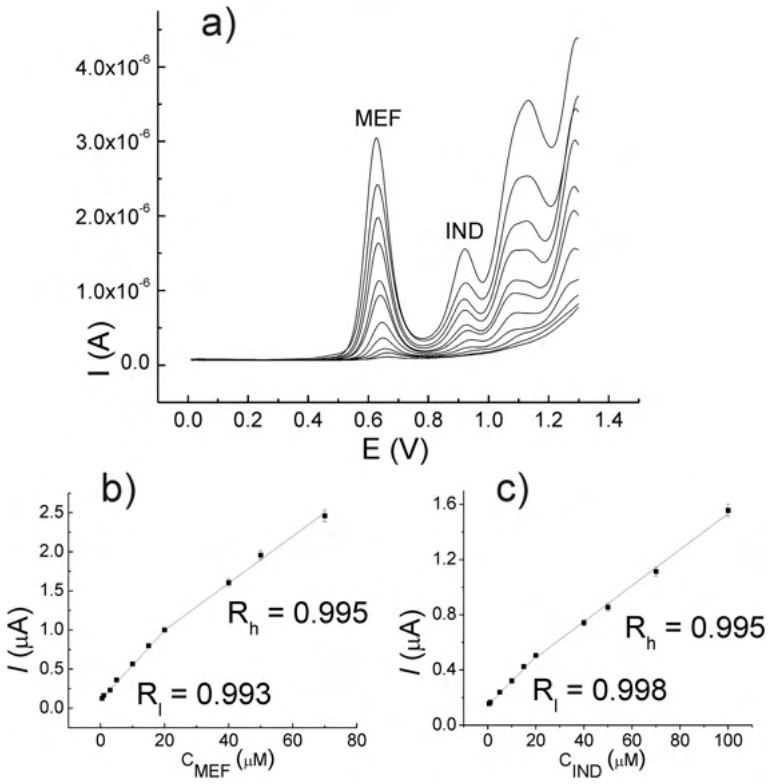

Fig. 1.24. (a) Differential pulse voltammograms and (b,c) dependence of peak current intensity on the concentration (0, 0.5, 1, 3, 5, 10, 20, 40, 50, 70, and 100M) of a mixture of mefenamic acid and indomethacin in Britton-Robinson buffer solution using boron-doped diamond [171].

Increasing the concentration of compounds in a solution changes the intensity of the peak currents for selected potentials, allowing simultaneous detection of compounds as shown in Fig. 1.24 (a). The detection curve of indomethacin (Fig. 1.24 (b)) has a wider linear range than that of mefenamic acid (Fig. 1.24 (c)). The presented method is relatively inexpensive and fast compared to other techniques which can also require sample pre-treatment [173–175].

In summary, boron-doped diamond shows unique properties making it useful in modern (bio)sensors and electrochemical systems. Detection by either current or impedance change analysis is possible. Proper selection of the diamond's surface impacts the device's sensitivity.

2. AIM AND HYPOTHESIS OF THE DISSERTATION

Diamond is a versatile material that has many advantages including: high thermal and electrical conductivity, biocompatibility, chemical stability, and high wear resistance. These advantages of diamond make it an almost ideal material for future electronics. High carrier mobility and thermal conductivity make it possible to create modern and high-speed electronic devices. Biocompatibility allows integration into the human body, and the durability of the material protects our environment. High chemical resistance can protect from chemical hazards in emergency situations. As a result, diamond can be 'an intersection of technology and biology for our century' [176].

However, the semiconductor properties of diamond, particularly thin and free-standing, have not been fully revealed, including their integration with polymers and use in electronic devices. Generally, CVD diamond films are fabricated at temperatures above 500 ℃ (in the case of linear antenna systems – above 350 ℃). For that purpose, the use of high temperature-resistant substrates is required. Most of these substrates can not be used as flexible substrates. Therefore, an alternative approach utilising tantalum as a substrate during CVD growth for fabricating free-standing boron-doped diamond films (FBDDF) developed at the home department [177] can be used to transfer films to flexible substrates (i.e.PDMS, Polyimide). Based on this, **the aim of the dissertation is the fabrication of heterostructures containing diamond films on flexible surfaces for application in electronic devices using the change of electrical parameters under the influence of external factors (e.g. pressure, temperature, stress). The specific goal is to fabricate diamond on flexible substrates at low temperatures for sensing applications (including conversion and accumulation of energy)**.

The study focuses on determining the most important electrical properties of free-standing diamond films as a function of the synthesis parameters (temperature, growth time, methane and boron concentration in the gas phase). These parameters change the type and level of conductivity, sp^3/sp^2 ratio, thickness, grain size, and capacitance of the diamond. The value of the capacitance can define if the realised films can find application as a capacitor or sensing device. Additionally, the semiconducting properties of free-standing boron-doped diamond films were studied as a function of the surface termination. The surface termination and morphology of the films strongly affects the electrochemical properties, which are crucial in the implementation of sensors and electronic components. To investigate the electrochemical properties, outer-sphere electron transfer processes and inner-sphere transfer processes can be used. Based on the studied properties of free-standing diamond films, the author of the dissertation uses the most effective films to develop electronic devices.

Combining free-standing diamond films with polymers makes it possible to fabricate flexible, transparent sensing devices. For this purpose, the following polymers can be used:

- Polydimethylsiloxane (PDMS) – a transparent polymer used for 2D material transfers, microfluidics, and lab-on-a-chip devices [178, 179].
- Polyimide – a flexible insulation film commonly used in the electronics industry that is able to withstand high temperatures and harsh environments [180].
- Polyamide – commonly found in fabric and fibres requiring both flexibility and strength [181].

Furthermore, the combination of free-standing diamond films, polymers, and two-dimensional materials presents new opportunities for fabricating junctions, transistors, and other electronic devices. The addition of FBDDF should improve the electrical, thermal conductivity and mechanical properties of the resulting heterostructure. Heterostructures containing FBDDF can be more durable, and the manufacturing process should require fewer non-renewable resources, thereby protecting the environment.

The following research hypotheses were formulated:

H1. Increasing the concentration of boron can lead to a metallic conductivity mechanism for free-standing diamond films.

H2. Electrical parameters of boron-doped free-standing diamond films can be modified by applying stress that changes inter-grain charge transfer mechanisms in these films.

H3. Utilising a low concentration of boron in free-standing diamond films enables the fabrication of Schottky junctions.

H4. Low surface roughness and structural defects due to the tantalum substrate can induce efficient electron transfer in electrolyte operation for electronic device applications (i.e. sensors, capacitors, transistors)

3. GROWTH AND DIAGNOSTICS OF FREE-STANDING DIAMOND FILMS

3.1. Summary of measurement methods

Before fabricating diamond-composed heterostructures (structures consisting of two dissimilar materials, usually with different band gaps or crystal compositions [182, 183]), it was necessary to fabricate free-standing diamond films (FDF) and study their morphological, electrical, chemical, and mechanical properties. Based on this, films could be selected for the manufacturing of heterostructures. This chapter presents the fabrication and properties of FDF. The studies conducted in this part of the thesis are listed in Table 3.1.

Table 3.1. Conducted measurements of CVD-grown free-standing diamond thin films.

Characterisation technique	[B]/[C] ratio in the gas phase (ppm) during CVD growth	CVD growth time (h)
Raman spectroscopy	0–20,000	3
Scanning electron microscopy	0–20,000	3
Atomic force microscopy	10,000	3
Electrical measurements	250–20,000	3
	10,000	5
Mechanical measurements	10,000	12
Electrochemical measurements	250–20,000	3

Raman spectroscopy is a non-destructive method for analysing the electronic and structural properties of diamond films, i.e. the presence of defects, sp^3/sp^2 ratio, boron incorporation, and strain level. The research was conducted using a laser operating at a wavelength of 514 nm (LabRAM HR, Horiba Scientific, Japan), which was carried out by the author during an internship at Delft University of Technology (professor Buijnsters' group). Additionally, measurements were taken using a Micro-Raman spectrometer (InVia, Renishaw, United Kingdom) operating at a wavelength of 785 nm, in collaboration with the Institute of Fluid-Flow Machinery (Gdańsk, Poland). During the collaboration for this study, the author was actively involved in conducting the measurements. Furthermore, the author was responsible for analysing and developing all the results obtained in Delft and Gdańsk.

Scanning electron microscopy can evaluate materials' surface topography, morphology, and thickness. SEM micrographs of the free-standing diamond films were obtained using two

scanning electron microscopes: a JSM-6500F (JEOL, Japan), located in Delft, and a Quanta 250 FEG (FEI, USA), located in Gdańsk. The images taken in Delft were captured personally, while those obtained in Gdańsk were taken with the cooperation of the Department of Physics and Mathematics at the Gdańsk University of Technology. During the study, the author was analysing and developing the SEM results.

Atomic force microscopy can be used to confirm the results obtained by SEM, and to evaluate the roughness of the layers. The Wrocław University of Science and Technology provided the AFM topography results obtained by a Veeco Nanoman V (Bruker, USA), and the author of this thesis was responsible for analysing and interpreting the results.

Electrical measurements provide information about the conductivity of a sample and its behaviour as a function of temperature. They also enable the determination of the band structure of diamond, as well as the carrier mobility, concentration of dopants, and effect of strain. The measurements and analysis studies were personally performed using two systems: a HFS600E-PB4 system (Linkam, UK) and a setup developed by the author, which is available at the home department. The Department of Physics (University of California, Riverside, USA) contributed to the discussion and interpretation of the data.

In *mechanical tests*, the elastic modulus and hardness of the diamond films can be measured. Additionally, a sample with the longest possible process time was tested to determine the limits of diamond growth. The studies of personally prepared samples were conducted in collaboration with the Faculty of Mechanical Engineering at the Gdańsk University of Technology, using a NanoTest Vantage system (Micro Materials, UK) and a scanning electron microscope (S-3400 N, Hitachi, Japan). The results obtained from the studies were then analysed and interpreted by the author of this dissertation.

Electrochemical studies answer the question of whether a film can find use in sensors or energy storage components, while also providing information on interactions with electrolyte, carrier concentration, charge transfer kinetics, and band structure. The research was conducted at the University of Gdańsk and the home department, using a PGStat 128 N potentiostat (Metrohm Autolab, The Netherlands) and a VMP-300 (BioLogic, France). The author of the thesis participated in measurements at both the University of Gdańsk and Gdańsk University of Technology and was responsible for analysing and developing the results obtained from the home department (Cyclic Voltammetry and Impedance measurements).

The aforementioned studies enabled the proper selection of diamond films to fabricate heterostructures with polymers and materials that are not heat resistant.

3.2. Chemical vapour deposition of diamond films

All the free-standing diamond films presented in this work were synthesised using a chemical vapour deposition system (AX5400S, Seki Technotron) present at Gdańsk University of Technology. The parameters of the films were changed by varying the diborane and methane concentrations in the gas phase (Table 3.2). Different process times were also used. It should be noted that the concentrations of boron/methane in the plasma and in the diamond lattice after CVD growth are not equal. In the further parts of the dissertation, when the concentration of boron/methane is mentioned, it will refer to the concentration in the gas phase during CVD growth by default, unless stated otherwise.

Table 3.2. Concentrations of gases for the growth of FDF films by Chemical Vapour Deposition (CVD) with 1% methane concentration.

[B]/[C] ratio in plasma (ppm)	**H_2 (sccm)**	**CH_4 (sccm)**	**B_2H_6 (sccm)**
20,000	285	3	15
10,000	292.5	3	7.5
5,000	295	3	3.75
1,000	299.25	3	0.75
500	599.25	6	0.75
250	599.62	6	0.38
0	300	3	0

Before each growth, mirror-polished tantalum substrates (10 mm x 10 mm x 1 mm) were cleaned with acetone and isopropyl alcohol for 5 minutes. Next, they were seeded ultrasonically in an aqueous suspension containing nanodiamond powder (4–7 nm in size) for 15 minutes. After seeding, the substates were rinsed with isopropyl alcohol for 1 minute.

A photo of the setup for chemical vapour deposition is shown in Fig. 3.1. The setup includes a microwave generator with an operating frequency of 2.45 GHz, a waveguide, a chamber with a heated graphite stage on which the sample is mounted, a control panel, a pyrometer for temperature measurement, and gas supply lines.

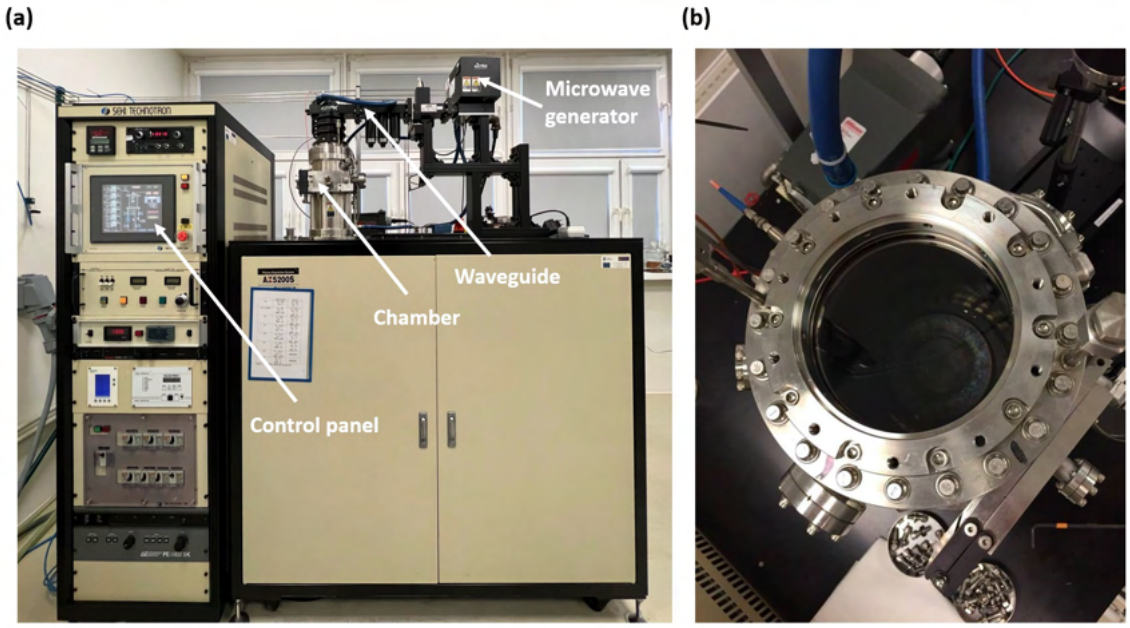

Fig. 3.1. (a) Chemical vapor deposition setup available at Gdańsk University of Technology, (b) Interior of the chamber, with the waveguide that supplies microwaves from the generator removed.

After the samples are introduced into the chamber (Fig. 3.1 (b)), the pressure is lowered to 10^{-3} Torr. Once the temperature reaches 500℃, hydrogen is introduced into the chamber. One minute later, the pressure is again lowered to 10^{-3} Torr. This is done primarily to remove residual oxygen and nitrogen. The pressure is then raised to 50 Torr and the appropriate gases are introduced into the chamber and the plasma is turned on. The plasma microwave power is kept at 1.1 kW, while the substrate temperature is 500℃ during the process. The pressure inside the chamber during diamond growth is 50 Torr.

Once the diamond growth is complete, the plasma is turned off and the chamber cooled with hydrogen. During cooling, the lattice mismatch and the difference in the thermal expansion coefficients between the tantalum and the diamond is enough to produce initial stresses that prohibit proper adhesion of the diamond film [177, 184].

3.3. Diamond transfer systems and procedures

As mentioned in the introduction, the process of fabricating free-standing diamond films is more complex and time-consuming than the growth of diamonds themselves. In 2019, a method for producing FDF using delamination of diamond from a tantalum substrate was proposed by a research team at the home department. This method allows for the transfer of FDF onto various materials, such as SiO_2/Si, Au, and graphene [177]. However, the method of transfer and integration with polymers and not heat resistant, fragile substrates required further development.

The first method developed by the author of this dissertation, illustrated in Fig. 3.2, involves

the use of PDMS (polydimethylsiloxane) and Kapton. Kapton is a flexible polyimide that is widely used in electronics due to its excellent thermal stability, high strength, and electrical insulating properties. After the diamond growth process, the surface of the diamond film is coated with PDMS (Fig. 3.2 (a)) that was prepared in advance using a Sylgard 184 kit with a hardener/base ratio of 1:10 (3h in 60℃). After the PDMS layer is applied to the diamond, the tantalum layer can be mechanically removed, resulting in a nucleation side on the PDMS surface. To work with the top surface of the diamond, Kapton can be placed on the diamond surface, and the PDMS layer should be removed similarly to the tantalum layer (second row of Fig. 3.2 (a)). This is made possible by Kapton's superior adhesion compared to PDMS. In the case of using only the nucleation side, PDMS can be substituted by Kapton, as shown in Fig. 3.2 (b).

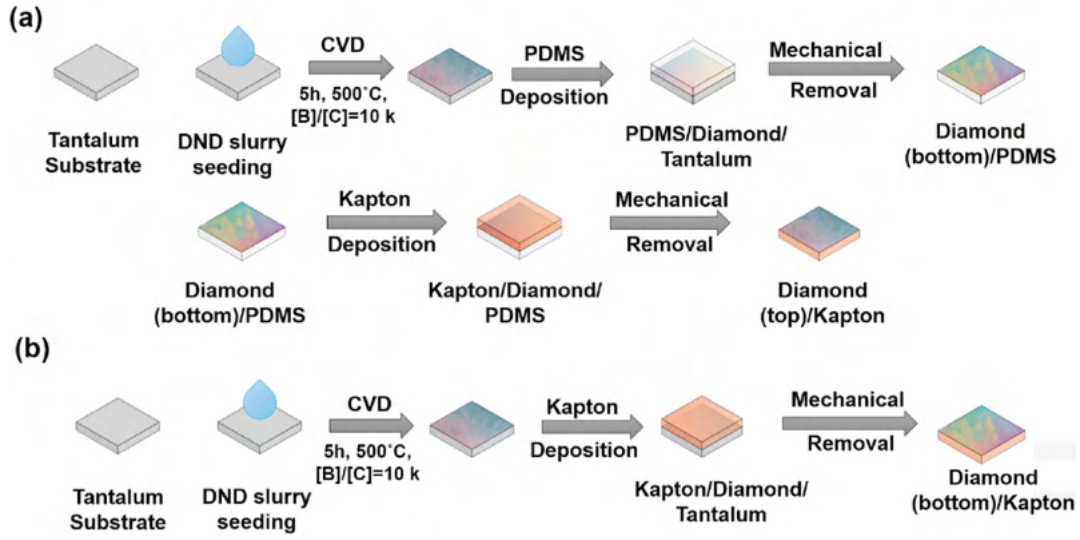

Fig. 3.2. (a) Transfer of the growth surface, and (b) transfer of the nucleation side of diamond onto polyimide [MR3].

The fabricated FBDDF on PDMS and FBDDF on Kapton are presented in Figs. 3.3 (a) and (b), respectively.

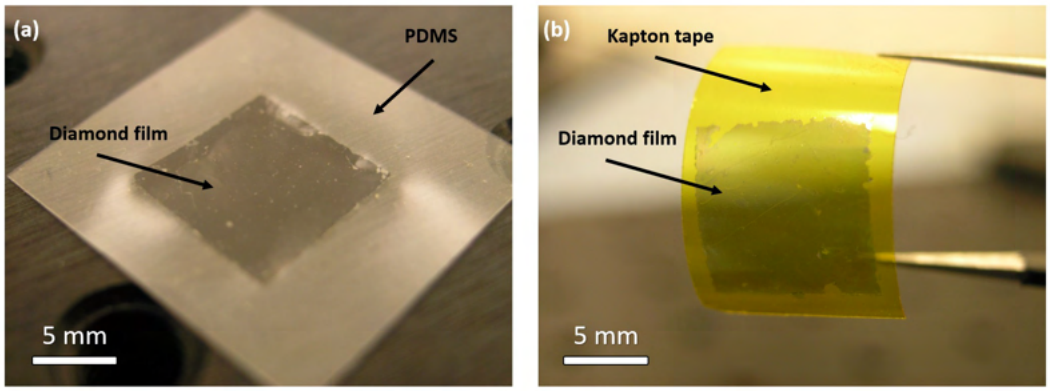

Fig. 3.3. (a) FBDDF ([B]/[C] = 20,000 ppm, 4% methane concentration during 3 hours of CVD growth) on PDMS, and (b) FBBDF ([B]/[C] = 10,000 ppm, 1% methane concentration during 3 hours of CVD growth) on Kapton. The photos were taken with a digital camera (C-5060, Olympus, Japan).

Although transfer using PDMS is a commonly used method, it is not considered ideal due to the residues and deformations that may be introduced during the process [185]. Therefore, a second transfer method has been proposed by the author of this dissertation to overcome these limitations.

In the first step of the transfer process, the diamond film is placed onto a SiO_2/Si substrate using tweezers and then fractured using electrical probes, as illustrated in Fig. 3.4 (a). Sonication of the diamond on tantalum, followed by evaporation of the solution on the SiO_2/Si substrate, can also be used to break down the films. As a result, diamond films are formed with widths and lengths ranging from several to ten micrometres on the SiO_2/Si substrate (Fig. 3.4 (b)). Next, a droplet of PDMS is deposited onto flat commercially available PDMS film (PF X-4, Gel-Film, USA), which is in direct contact with prepared transparent microscopic glass. After being heated at 60℃ for 3 hours, the hemisphere of PDMS is coated with a thin layer of polypropylene carbonate (PPC) in anisole (5%) for 5 minutes (70℃). Afterwards, the diamond film can be removed from the SiO_2/Si using XYZ and XY stages at room temperature (22℃ and 44 % RH) as presented in Fig. 3.4 (c) and placed onto the desired substrate (Fig. 3.4 (d)), which is heated to 120℃. Any remaining polymer residue (shown in Fig. 3.4 (e)) can be removed using acetone, resulting in a free-standing diamond film on the desired substrate, as illustrated in Fig. 3.4 (f).

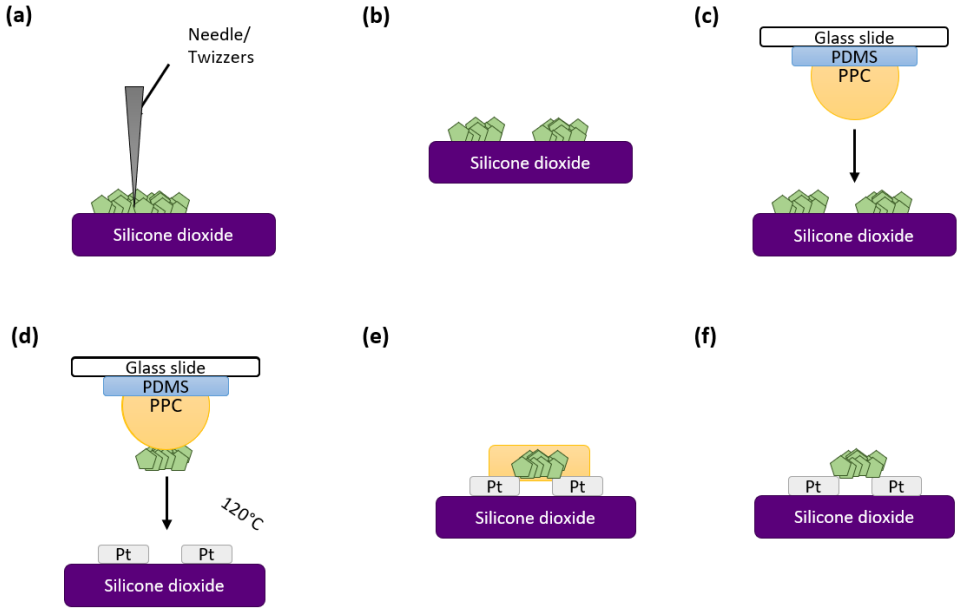

Fig. 3.4. Schematic diagram of the modified transfer procedure developed by other authors [128, 186, 187], and optimised for transporting free-standing diamond films by the author of the dissertation.

In order to carry out the second transfer method, it was necessary to design the system shown in Fig. 3.5.

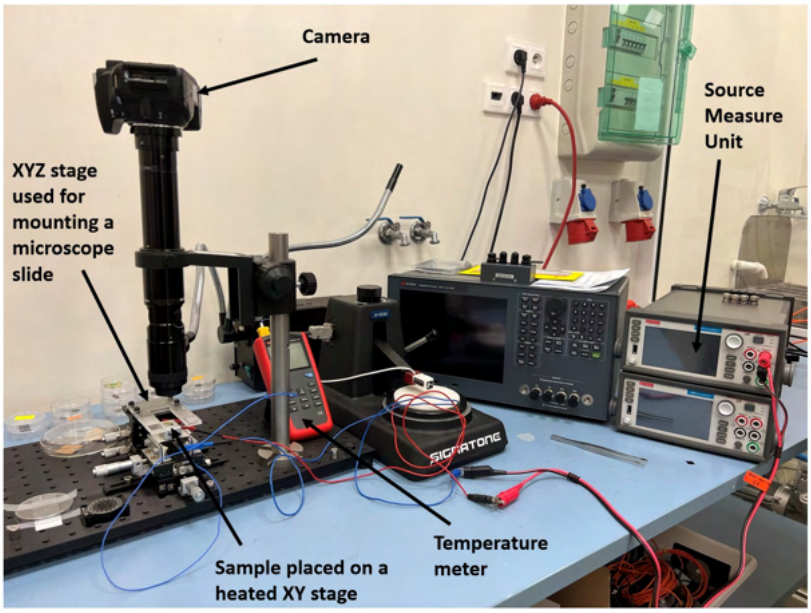

Fig. 3.5. System for transferring 2D materials and free-standing diamond films.

The experimental setup used for transferring two-dimensional and three-dimensional materials consists of a zoom lenses (Navitar, USA) supplemented with a digital camera (D5600, Nikon, Japan), with coaxial illumination, an XY stage for the sample, and an XYZ stamp stage. All components are mounted on an optical breadboard using magnets. The microscope images can be transmitted via Wi-Fi to an application on a phone or computer. Similar setups have been used in other transfer methods [187–189]. However, the presented setup has been modified to incorporate several advantages, including low cost, heating capability, glove-box assembly, high accuracy, high-quality images, and rotational alignment. The system allows the sample to be heated up to the melting point of tin, which is higher than the required 120 ℃, since the sample is mounted on a table made of tin.

Images taken during the transfer of FDF using the system designed by the author of this dissertation are presented in Fig. 3.6.

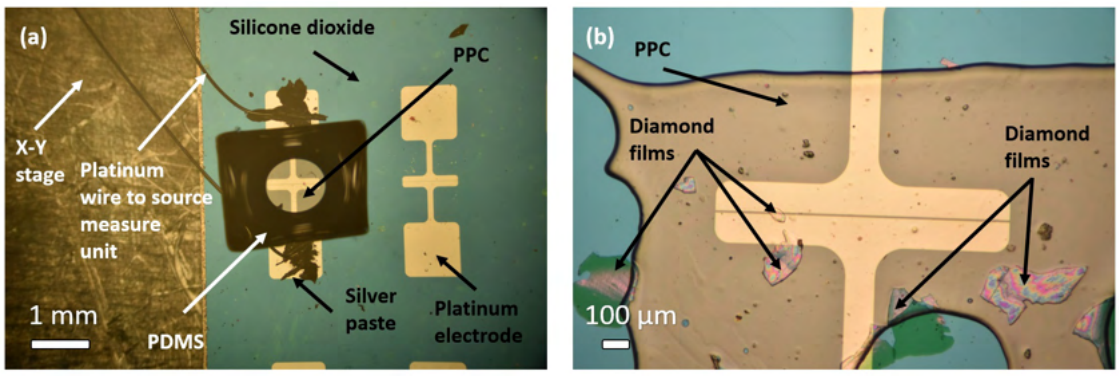

Fig. 3.6. (a) Moment of transfer of the diamond film onto the electrode surface. (b) Diamond film on the electrode with the remaining polypropylene carbonate (PPC) residue after transfer.

To summarise, two diamond film transfer methods have been designed and developed. The first method utilises PDMS and Kapton and is suitable for larger electronic devices that do not require high sample purity. The second method, which is more time-consuming, allows for fabrication with micrometre precision. The use of PPC reduces polymer contamination on the diamond surface.

3.4. Raman spectroscopic investigation of fabricated films

The Raman spectra of free-standing diamond films as a function of the [B]/[C] concentration in the gas phase is shown below. The experimental data was acquired utilising a LabRAM HR (Horiba Scientific, Japan).

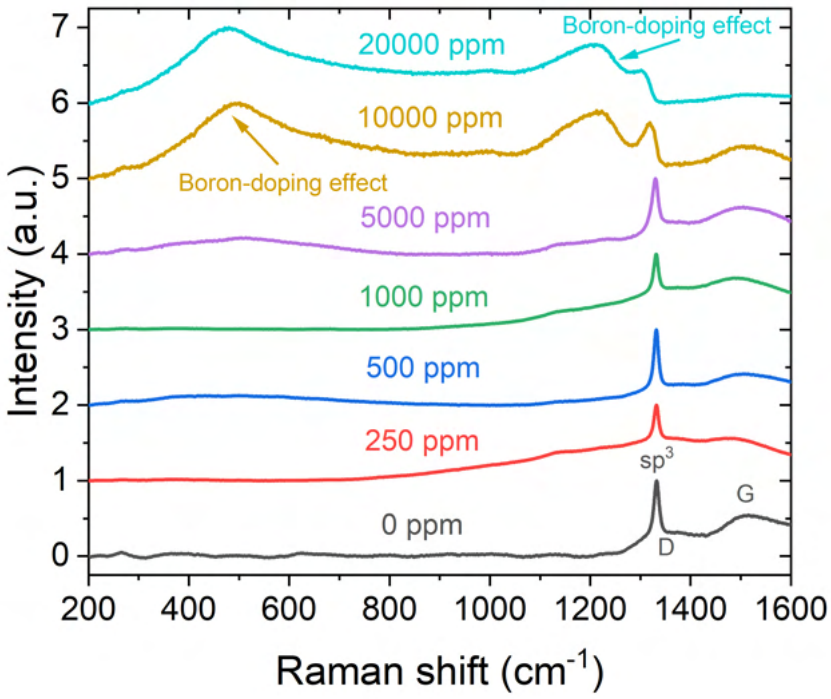

Fig. 3.7. Raman spectra obtained for free-standing diamond films with different levels of boron doping. The laser operated at a wavelength of 514 nm, a power of 450 μW, and a spot size of 2 μm [MR1].

Increasing boron level up to 20,000 ppm leads to the red-shift of the diamond zone centre phonon line located at around 1332 cm^{-1} for relatively low-doped samples. This shift in the peak position is attributed to factors such as an increase in the B-doping level [35], variations in grain sizes and shapes [190, 191], and differences in boundary densities [192], resulting in variation of the residual stress [193]. The deformation of the diamond (sp^3) peak, known as the 'Fano effect', is only observed in heavily doped samples prepared with a [B]/[C] ratio of 10,000 and 20,000 ppm. In addition, as the doping increases, bands with asymmetric shapes centred around 500 cm^{-1} and 1200 cm^{-1} appear. The 500 cm^{-1} band for the heavily boron-doped diamond films can be fitted

by a Lorentzian and a Gaussian component to estimate the boron incorporation into the diamond lattice (Fig. 3.8) [194]:

$$B = 8.44 \cdot 10^{30} \exp\left(-0.048 \cdot W\right) \tag{3.1}$$

where W is the wavenumber of the Lorentzian component in cm^{-1}. The boron content was found to be $1.88 \cdot 10^{21}$, $2.27 \cdot 10^{21}$, and $3.75 \cdot 10^{21}$ atoms/cm^3 for samples grown at 1%, 2%, and 4% of methane concentration in the gas phase, respectively [MR1, MR6].

The Raman spectra presented in Figs. 3.7 and 3.8 consist of two bands at around 1350 cm^{-1} and 1550 cm^{-1}, which are attributed to the sp^2 phase. The existence of aromatic sp^2 rings can be inferred from the presence of the D peak (1350 cm^{-1}), while the G peak (1550 cm^{-1}) originates from sp^2-C in both rings and chains [195]. These peaks are more prominent for the samples with the higher methane concentrations (Fig. 3.8) indicating a lower quality diamond film. The increase in the sp^2/sp^3 ratio and higher incorporation of boron into the diamond lattice with an increasing concentration of methane are in agreement with the research presented by Rouzbahani et al. [57] for heavily boron-doped single-crystal diamond.

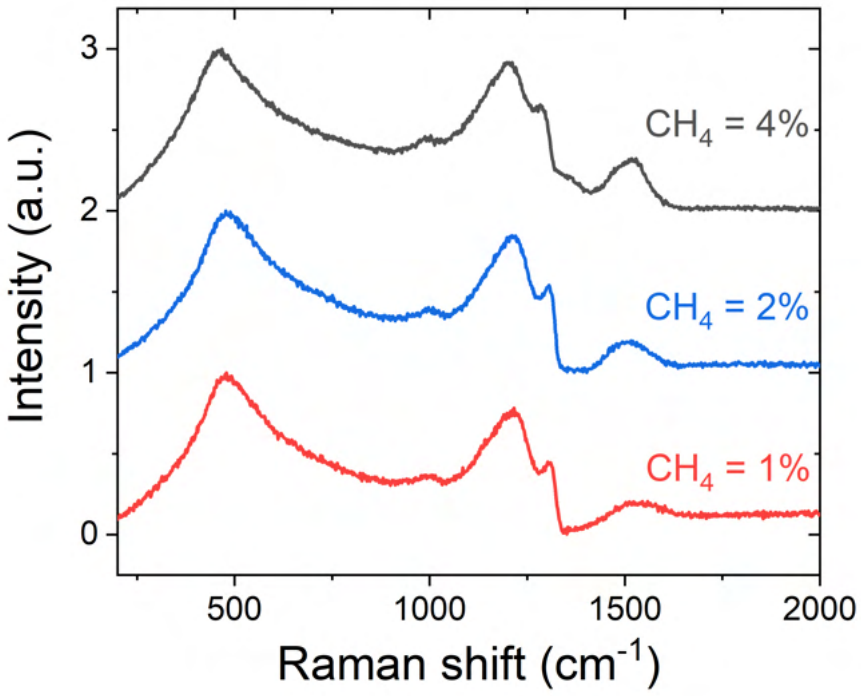

Fig. 3.8. Raman spectra for free-standing diamond films with various methane concentrations in the gas phase during CVD growth. The data was acquired using a Micro-Raman spectrometer (InVia, Renishaw, United Kingdom) that operates at a wavelength of 785 nm [MR6].

The articles [MR3, MR5] report Raman spectra for the growth surface and nucleation side of the sample with [B]/[C]=10,000 ppm and 20,000 ppm. The free-standing diamond films' top surface has a higher boron concentration than the nucleation side due to boron suppression during

the initial stage of CVD growth caused by residual oxygen in the chamber [147]. Boron incorporation into the diamond lattice is not a homogeneous process, with an sp^3/sp^2 ratio depending on the duration of the process and the level of doping. The nucleation side can have a higher sp^3/sp^2 ratio [MR3], while a lower ratio can be obtained by changing the CVD growth time for the same boron concentration as presented in the article [MR5]. Similar sp^3/sp^2 ratios were obtained by other groups [35, 196].

It can be concluded that Raman spectroscopy of diamond films reveals shifts in diamond lines and the appearance of new bands with increased doping. Boron incorporation into the diamond lattice was affected by the methane concentration and found to be a non-homogeneous process. Additionally, the sp^3/sp^2 ratio can be shaped by the growth time [MR3, MR5].

3.5. Scanning Electron and Atomic Force Microscopy

The morphology of the growth and nucleation surface of diamond films with different boron concentrations in the gas phase is presented in Fig. 3.9.

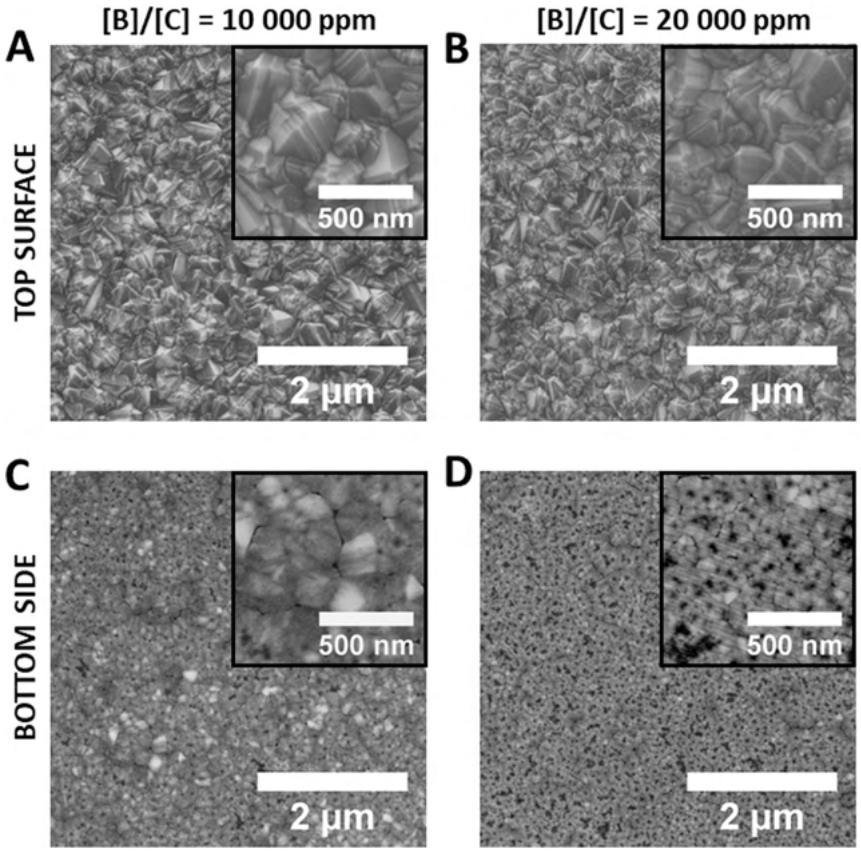

Fig. 3.9. Top surface (A,B) and nucleation side (C,D) for [B]/[C]=10,000 and 20,000 ppm, respectively. The images were obtained utilising a scanning electron microscope, specifically a Quanta 250 FEG (FEI,USA), with a 10 kV beam accelerating voltage and a secondary electron Everhart-Thornley detector [MR5].

The nucleation side is smooth due to direct contact with tantalum during CVD growth, with highly visible grain boundaries. Black spots result from interfacial defects (either amorphous

or graphitic forms), while a few nano-sized gaps are caused by the detachment of individual grains. These results are in agreement with the findings presented by other groups for micro-and nanocrystalline diamond films [195, 197]. The mean planar grain radius for the growth surface is shown as a function of boron doping in the gas phase in Fig. 3.10.

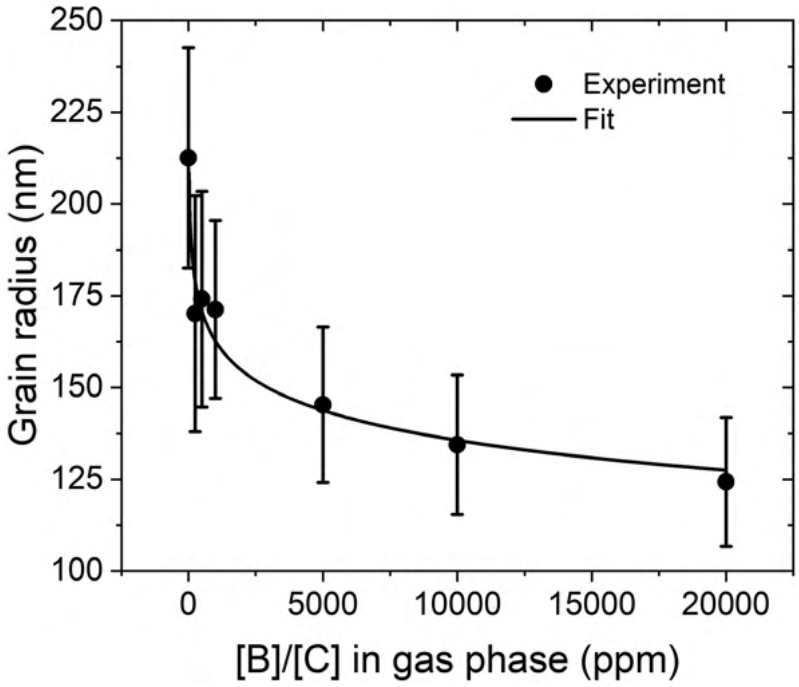

Fig. 3.10. Average planar grain radius of the diamond films as a function of boron doping in the gas phase. The error bars represent the standard error of the mean. Data was obtained using a scanning electron microscope (JSM-6500F, JEOL, Japan) in secondary electron imaging mode [MR1].

An increase in the boron concentration in the gas phase leads to a significant reduction in the grain radius and surface roughness. Due to random nucleation, the grains do not exhibit any preferred crystalline orientation, and they are non-spherical and of various sizes due to non-homogeneous doping.

The AFM topography (Fig. 3.11) confirms the SEM results. The nucleation side (Fig. 3.11 (b)) is smoother than the growth surface (Fig. 3.11 (a)), and no faceted grains are visible. The average roughness was 10 nm, while the top surface had a roughness value of 54 nm [MR3]. The increased roughness is an outcome of the sharp edges of faceted grains.

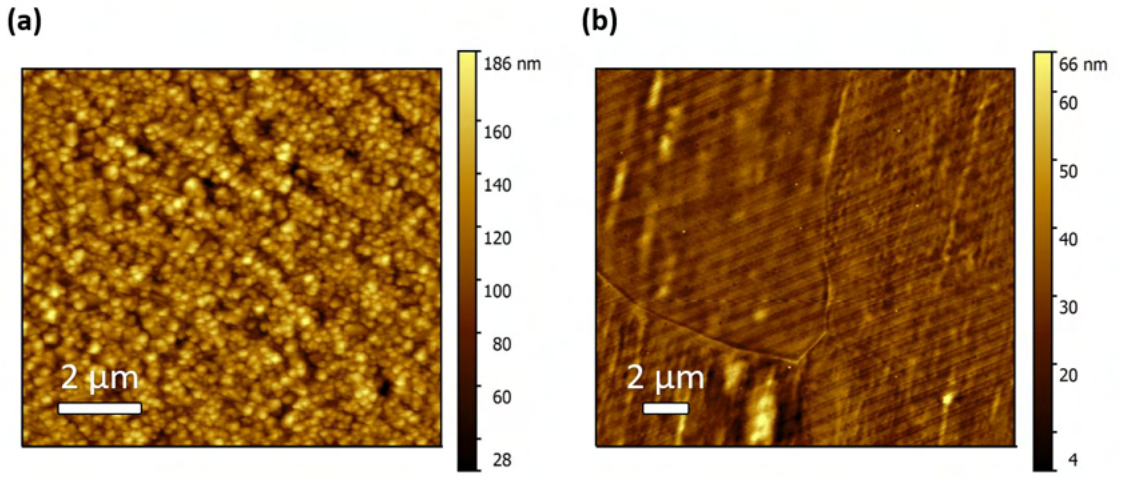

Fig. 3.11. AFM results obtained from a sample with [B]/[C] = 10,000 and a growth time of 3 hours. The measurements were performed using a Veeco Nanoman V (Bruker, USA) microscope equipped with a Nanoscope V controller.

The difference in surface morphology of free-standing diamond films is the result of boron-doped film growth from spherical nucleation sites, followed by a Van der Drift growth model. Over time, a columnar growth structure becomes apparent (Fig. 3.12). Williams et al. [19] demonstrated similar effects, where larger grains overlap with smaller ones.

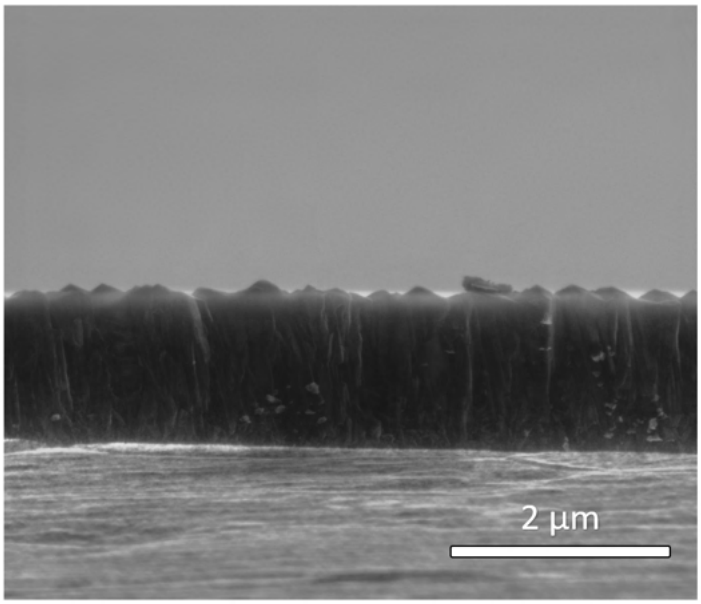

Fig. 3.12. Columnar growth of diamond films resulted in film thicknesses ranging from 300 nm to 4.2 µm for 1.5 and 12 hours of CVD growth, respectively.

When there are changes in the methane concentration in the gas phase, morphological studies indicate that an increase in the standard deviation of the grain size and the film thickness are correlated with a higher sp^2 phase, as demonstrated in [MR6].

The SEM study also showed that the growth rate for tantalum obtained at Gdańsk University of Technology was higher compared to the values obtained for silicone and quartz by other groups [198].

To conclude, scanning electron in secondary electron imaging mode and atomic force microscopy were utilised to analyse the topography, thickness, and growth model of the diamond films. The top surface exhibits higher surface roughness and fewer defects in comparison to the nucleation side. An increase in doping leads to reduced surface roughness, while a higher methane concentration causes an increase in the standard deviation of the grains and film thickness. As a result, the selection of the side of FDF in direct contact with another material can be crucial in shaping their interface. The diamond growth follows the Van der Drift model.

3.6. Electrical measurements

Fig. 3.13 (a,b) show the I-V characteristics of the fabricated free-standing boron-doped diamond films for two selected temperatures of measurement – 153K and 293K. The measurements were carried out on diamond films grown for a process time of 3 hours and with boron concentrations ranging from 250 ppm to 20,000 ppm in the gas phase. Ohmic contacts (Au/Ti) were used for bulk conductance measurements [66].

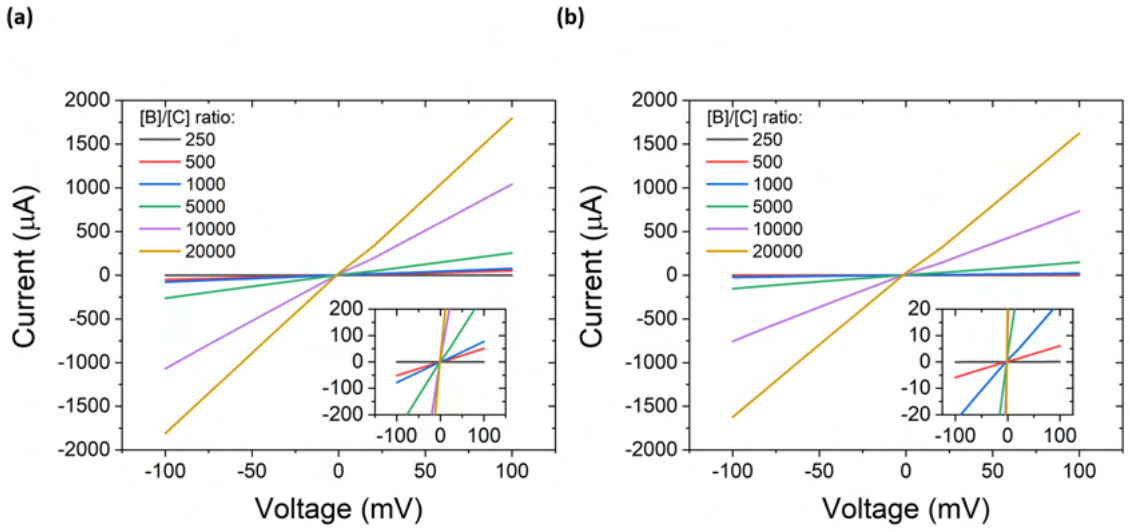

Fig. 3.13. Current-voltage characteristics of boron-doped diamond films at (a) 153K and (b) 293K, respectively. The measurements were performed using a HFS600E-PB4 Linkam system (United Kingdom). The residual sum of squares for linear fit did not exceed 10^{-9}.

In the studied voltage range, the characteristics are linear (Fig. 3.13 (a,b)). As the temperature increases, there is a change in the slope of the curve, and consequently, in the conductance of the samples. It should be noted that the slope for the sample with the [B]/[C] = 20, 000 ppm in the gas phase is virtually constant. Based on the presented figures, it can be concluded that the

observed changes in current are ohmic, and are proportional to the voltage applied [199].

The systematic variations of the conductance versus temperature (153-473K) for different boron levels are presented in Fig. 3.14.

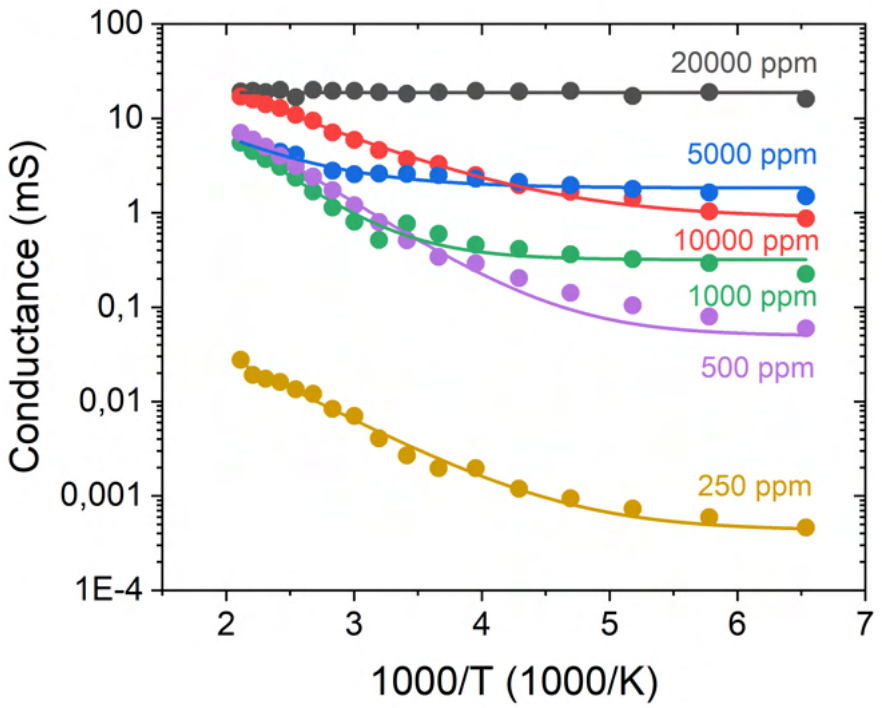

Fig. 3.14. Bulk conductance of boron-doped free-standing diamond films (FBDDF) as a function of the boron concentration in the gas phase. Six measurements were performed for each temperature. The standard error of the mean conductance did not exceed 2.5% of the mean value [MR1].

The sample with [B]/[C] = 20,000 ppm was virtually constant across the entire temperature range (153–473 K) studied. Lower doping level ([B/C] < 20,000 ppm) shows a reduction in the boron concentration, resulting in an increase in resistance, which is particularly evident at lower temperatures (<250 K). A similar trend is also observed at higher temperatures (393-473 K).

Based on Fig. 3.14 and research conducted by other groups on diamond films [199–202], two mechanisms of conductivity can be distinguished in FBDDF: thermal activation from the valence band into the impurity band under a high-temperature regime and variable range hopping for lower temperatures. For high temperatures, the data can be approximated using the function:

$$\sigma = A \exp\left(-\frac{E_A}{kT}\right) \tag{3.2}$$

where

$$A = 283.3\ \Omega^{-1}\ \mathrm{cm}^{-1} \exp\left(-2.16 \cdot 10^{7}\ \mathrm{cm}^{-1} \cdot N_A^{-1/3}\right) \tag{3.3}$$

Here, σ represents the conductivity, N_A is the acceptor concentration, E_A is the activation energy,

T is the temperature, and k is the Boltzmann constant [203]. As a result, the activation energy for thermal hopping across an energy barrier can be calculated. The values of E_A are shown in Table 3.3. The activation energy increases with the decreasing boron concentration because impurity bands form [204]. To calculate the concentration of the holes in the fabricated diamond films, the following equations are used:

$$p = \frac{N_D + N_X}{2}\left(\sqrt{1 + \frac{4N_X(N_A - N_D)}{(N_D + N_X)^2}} - 1\right) \tag{3.4}$$

$$N_X \equiv -\exp\left(\frac{E_A}{k \cdot T}\right) \tag{3.5}$$

where N_D is the concentration of compensating donors [38, 205, 206]. The boron concentration was determined by electrochemical measurements using the Mott-Schottky method by the author of this dissertation, and the results are presented in section 3.8. In the case of [B]/[C] = 250 ppm in the gas phase, Secondary-Ion Mass Spectrometry studies utilising an Atomika 4500 (Cameca, France) were performed to estimate the boron concentration in the diamond lattice. Additionally, for the [B]/[C] = 20,000 ppm sample, the concentration of boron was determined based on the Raman spectrum, as presented in section 3.4. The concentration of the donors was estimated according to the results reported by Tsukioka et al. [207] and Bormashov et al. [208]. Fig. 3.15 shows the temperature dependence of the carrier concentration, determined using equation 3.4.

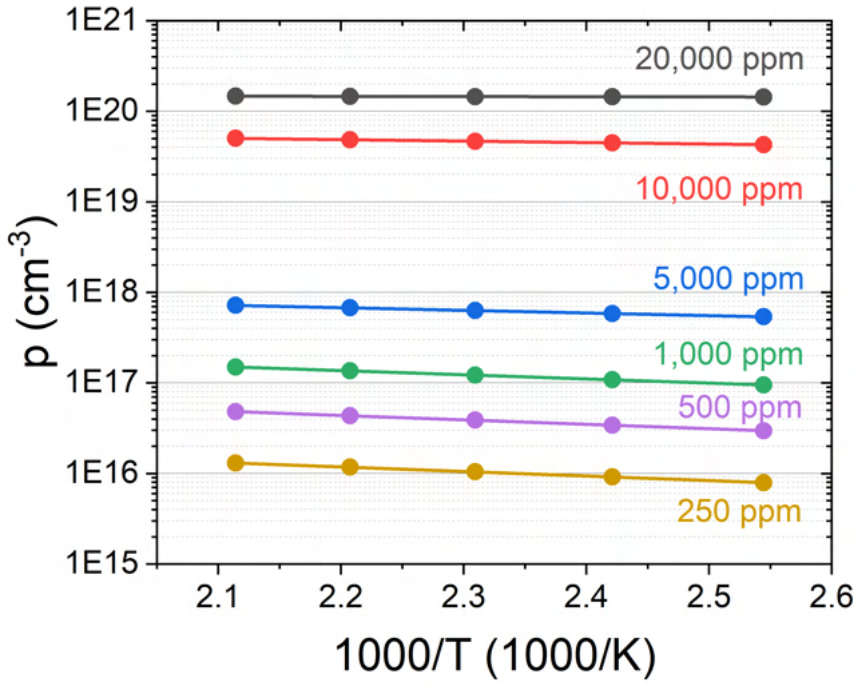

Fig. 3.15. Hole (carrier) concentration in boron-doped diamond films as a function of temperature and boron concentration in the gas phase during CVD growth.

Less pronounced temperature dependence is observed in the high-temperature regime for heavily doped free-standing diamond films with [B]/[C] ratios of 10,000 and 20,000 ppm. This finding is in agreement with the results reported by Gajewski et al. [38].

The carrier mobility was determined based on the concentration of holes and assuming ionized impurity scattering, using the equation given in [38]:

$$\mu_{ionized} = \frac{64\sqrt{\pi}\epsilon^2(2kT)^{3/2}}{pe^3\sqrt{m_h}} \cdot \left(\ln\left(1+\left(\frac{12\pi\epsilon kT}{e^2 p^{1/3}}\right)^2\right)\right)^{-1} \tag{3.6}$$

where ϵ represents the permittivity, e is the electron charge, and m_h is the effective hole mass.

A summary of the electrical parameters of the free-standing diamond films can be found in the following Table 3.3.

Table 3.3. Resistivity, activation energy, carrier concentration, hole mobility, and hole concentration of boron-doped free-standing diamond films as a function of the boron concentration in the gas phase.

[B]/[C] (ppm)	Resistivity at 293K (Ω·cm)	E_A (meV)	N_A (atoms/cm^3)	μ (cm^2 V^{-1} s^{-1})	p (cm^{-3})
250	1605.23	150	$1.22\cdot10^{18}$⋆	421	$2.51\cdot10^{15}$
500	581.91	147	$4.31\cdot10^{18}$	127	$9.75\cdot10^{15}$
1,000	129.61	140	$1.22\cdot10^{19}$	43.6	$3.35\cdot10^{16}$
5,000	7.61	98	$3.16\cdot10^{19}$	7.36	$2.88\cdot10^{17}$
10,000	0.71	58	$1.26\cdot10^{21}$	0.32	$3.08\cdot10^{19}$
20,000	0.38	-	$1.88\cdot10^{21}$⋆	0.16	$1.39\cdot10^{20}$

⋆SIMS studies have shown a boron concentration of approximately $4.5 \cdot 10^{17}$ atoms/cm^3. The differences arise from the non-homogeneous boron doping of the samples.

⋆Value obtained from the Raman spectrum.

The introduction of boron doping increases the conductivity of the diamond films by creating impurity bands [204]. However, the concentration of boron is not equal to that of carriers. Boron can be located in areas that do not participate in the continuum of electronic states, such as interstitials, the surface of crystallites, and non-diamond carbon impurities at grain boundaries [196]. During CVD growth, there is a lattice mismatch between neighbouring grains due to randomness in position and orientation, resulting in many disordered sp^3 and sp^2 phases at grain boundaries as observed by Zhang et al. [209] and Williams et al. [210]. In these disordered sp^3 and sp^2 phases, boron atoms act as impurities and do not contribute to the formation of mobile charge carriers for electronic transport [196, 209]. These statements were confirmed by studies by Zieliński et al. [211]. They found that the impedance at the boundaries between grains was up to 5 orders of magnitude

higher than within the grains themselves. Increasing the concentration of boron in the gas phase leads to a decrease in hole mobility too due to the increased number of grain boundaries (as seen in the SEM micrographs in Section 3.5) and scattering of ionised impurities at the boron acceptors, resulting in reduced mobility [55, 212]. This reduction in mobility of FDF follows the law [212, 213]:

$$\mu \approx 1/p. \tag{3.7}$$

It has been observed that boron doping of diamond films on tantalum is less efficient compared to other studies on nanocrystalline diamond. For instance, Gajewski et al. [38] achieved boron concentrations of about 10^{21} cm^{-3} for CVD-grown diamond films on quartz with [B]/[C] = 3000 ppm. However, the resistivity and mobility values for heavily boron-doped diamond films are comparable with their results. Janssens et al. [55] were able to achieve a boron concentration of $1.8 \cdot 10^{21}$ cm^{-3} when [B]/[C] = 5,000 using fused silica as a substrate. This concentration was obtained for fabricated FBDDF when the [B]/[C] ratio in the gas phase was equal to 20,000 ppm during CVD growth. Stuchliková et al. [214] observed the 'Fano effect' in the Raman spectrum corresponding to metallic conductivity for diamond films grown on fused silica by chemical vapour deposition with [B]/[C] = 2,000 ppm. For FBDDF, this effect was present for [B]/[C] ratios $\geq$ 10,000 ppm. In the case of microcrystalline free-standing diamond films with a thickness above 200 μm and comparable boron concentrations in the diamond lattice, they exhibited higher conductivity than the nanodiamond free-standing diamond films presented in this thesis. This is attributed to the higher number of defects and grain boundaries in the nanodiamond films [215]. Similarly higher conductivity was observed for comparable boron concentrations in synthetic diamond Ib crystals [35, 37]. It should be noted that the author of this dissertation used different process parameters, including temperature, power, dopant precursor, and methane concentration, which significantly affect the doping efficiency. Wang et al. [216] showed that growth on tantalum produces crystallites of a smaller size compared to silicone, but no significant differences were observed in the Raman spectrum.

However, the lower doping efficiency allows for improved control of the atomic concentration of boron and high values of carrier mobility. The calculated mobility values are in agreement with the results obtained for diamond films using Hall measurements [177], [MR3].

Controlling the electronic properties of free-standing diamond films is also possible by changing the methane concentration. An increase in fabricated boron-doped diamond film conductance was observed with an increase in the methane concentration in the gas phase [MR6]. This may be attributed to an increased number of defects caused by dislocations in the diamond film, which provide alternative conduction pathways as reported for polycrystalline and single-crystal

diamond [217,218].

For temperatures below 293K, the FBDDF exhibit a variable range hopping conduction mechanism (Fig. 3.16), which follows the Mott model [219]:

$$\sigma \cdot T^{\frac{1}{2}} = \sigma_0 \cdot \exp\left(-B \cdot T^{\frac{1}{4}}\right) \tag{3.8}$$

where σ_0 and B are constants that are estimated from the intercept and slope, respectively, of the curve that linearises the obtained data points (Fig. 3.16) [202].

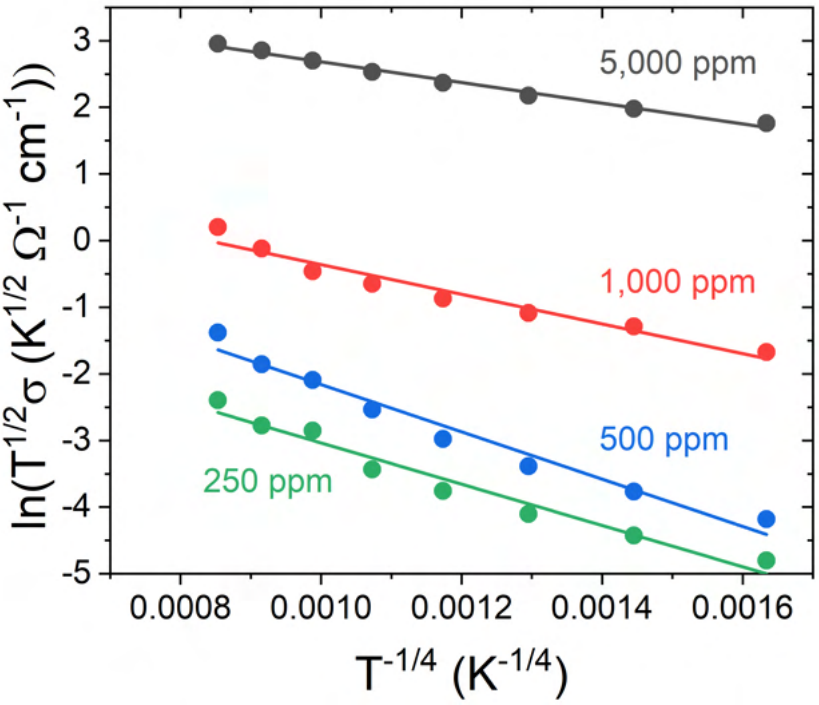

Fig. 3.16. Dependence of $\ln(T^{0.5}\sigma)$ vs. $1000T^{-0.25}$ of fabricated boron-doped free-standing diamond films as a function of the boron concentration in the gas phase.

An increase in boron doping during CVD growth results in a decrease in the slope of the curves and coefficient B, while the intercept and coefficient σ_0 increase. The hopping distance (D) and hopping energy (W) are calculated using formulas defined in [219–222] by Mott et al.:

$$D = \left(\frac{9}{8 \cdot \gamma \cdot \pi \cdot k \cdot T \cdot N(E_F)}\right)^{\frac{1}{4}} \tag{3.9}$$

$$W = \frac{3}{4 \cdot \pi \cdot D^3 \cdot N(E_F)} \tag{3.10}$$

Here, k represents the Boltzmann constant, T is the temperature, $N(E_F)$ describes the density of states at the Fermi level and γ is the measure of the extent of the localised function. γ

and $N(E_F)$ are obtained using the following equations:

$$\gamma = 22.52 \cdot \sigma_0 \cdot B^2. \tag{3.11}$$

$$N(E_F) = 2.12 \cdot 10^9 \cdot \sigma_0^3 \cdot B^2. \tag{3.12}$$

The calculated parameters for the fabricated free-standing diamond films with [B]/[C] = 250–5,000 ppm in the gas phase are presented in Table 3.4.

Table 3.4. Density of states at the Fermi level ($N(E_F)$), hopping energy (W), and distance (D) in FBDDF as a function of the boron concentration in the gas phase during diamond growth.

[B]/[C] in the gas phase (ppm)	$N(E_F)$ **(eV/cm^3)**	W **(eV)**	D **(nm)**
250	$2.43 \cdot 10^{16}$	0.07	52.2
500	$1.73 \cdot 10^{18}$	0.08	12.1
1,000	$2.87 \cdot 10^{18}$	0.05	11.9
5,000	$1.71 \cdot 10^{21}$	0.03	1.6

The increase in boron doping of FBDDF shifts the Fermi level towards the valence band and increases the density of states at the Fermi level. In addition, the hopping range and required energy decrease with the increasing boron concentration in CVD-grown diamond, which is in agreement with the increasing density of states in boron-doped diamond films.

The electrical resistance mapping of the diamond film ([B]/[C] = 10,000 ppm, 5h) was carried out using a two-point probe technique for both sides (growth and nucleation). The investigated area was 3.5 mm x 3.5 mm, and two micro-positioners (S-725, Signatone, USA) were mounted on the x-y stage to connect needles with a diameter of 20 μm to the SMU (2400, Keithley, USA) for these measurements. Additionally, a microscope (SZ-630, Delta, Poland) and a CMOS camera (DLT-Cam pro 20 MP, Delta, Poland) were employed to record the resistance contour mapping of the diamond film.

The resistance of both surfaces exhibits random variations due to the inhomogeneous incorporation of boron during the CVD process. An average resistance value of 66 Ω for the top surface (Fig. 3.17 (a)) and 4.4 kΩ (Fig. 3.17 (b)) for the nucleation side were obtained. The low conductance of the nucleation side is attributed to boron suppression during the initial growth due to the presence of oxygen [147], high number of grain boundaries [55] and defects introduced during the transfer.

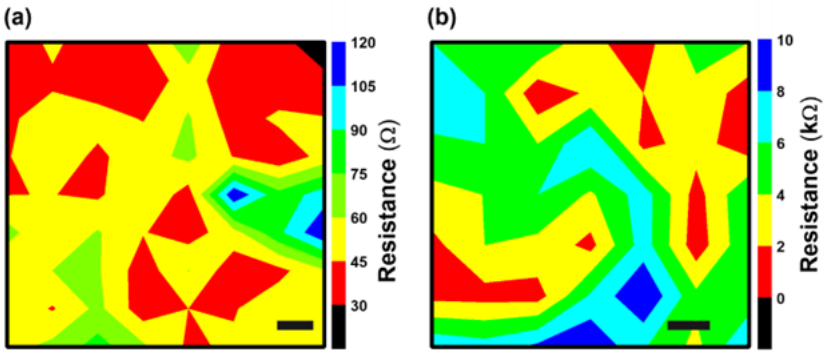

Fig. 3.17. Resistance map of growth (a) and nucleation surface (b). The scale bar is 500 μm [MR3]

In summary, electrical studies of FBDDF as a function of temperature were carried out. The highest boron-doped sample showed the lowest resistance that was virtually constant across the entire temperature range studied in comparison to lower doped samples. The higher doping level led to an increase in the density of states at the Fermi level and a decrease in both the energy and hopping distance. The increased number of grain boundaries resulting from the higher doping caused the carrier mobility to decrease from 421 to 0.16 $cm^2\ V^{-1}\ s^{-1}$. For lower doped samples ([B]/[C] < 20,000 ppm), two conductivity mechanisms were identified: thermal activation from the valence band to the impurity band at high temperatures and a variable hopping range at lower temperatures. During CVD growth of the FBDDF, an increase in the methane concentration resulted in an increase in sample conductance. This could be attributed to the increased number of defects caused by dislocations. Furthermore, it was demonstrated that heterogeneous boron incorporation during CVD growth leads to variations in resistance within a single film.

3.7. Nanoindentation tests of CVD-grown films

To study the mechanical properties, such as the elastic modulus and hardness, of the diamond films, nanoindentation tests were conducted using a three-sided Berkovich pyramidal diamond (NanoTest Vantage, Micro Materials, United Kingdom). The loading and unloading curves obtained during repeated loading cycles with increasing load for the diamond film are shown in Fig. 3.18 (a). The SEM micrographs obtained after the initial tests are presented in Fig. 3.18 (b). The study used a diamond film with a [B]/[C] ratio of 10,000 ppm in the gas phase and the longest process time of 12 hours. The goal was to study the mechanical parameters of the fabricated free-standing film with the largest thickness.

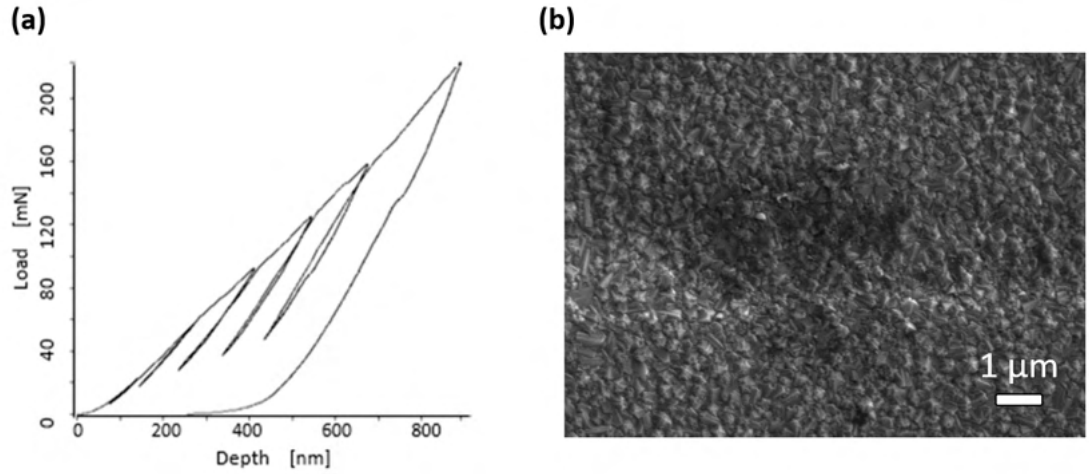

Fig. 3.18. (a) Load and unload curves of FBDDF (12 hours of growth time, [B]/[C]=10,000 ppm) collected during a multi-load cycle with increasing load and (b) SEM micrograph obtained after measurement (S-3400 N, HITACHI, Japan) [MR4].

Based on the recorded hysteresis loop, it is concluded that the fabricated CVD-grown diamond is characterised by its ability to dissipate energy elastically [223].

The reduced Young's modulus and hardness distribution profiles for the free-standing diamond film with [B]/[C] = 10 000 ppm and thickness of 4.2 µm are shown in Fig. 3.19 (A) and (B), respectively.

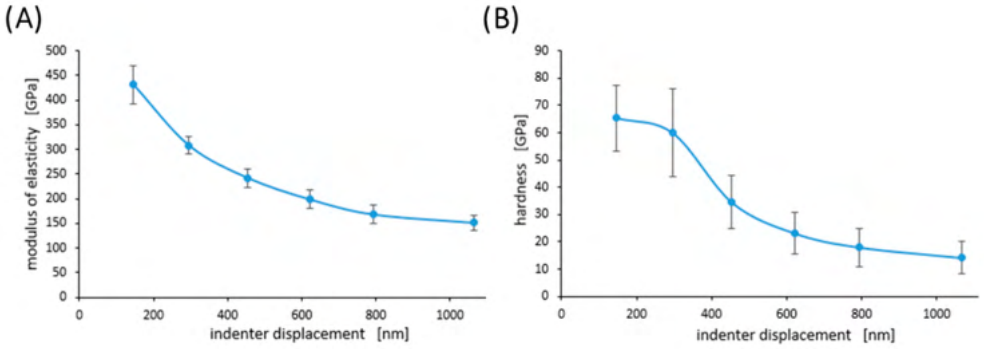

Fig. 3.19. (A) Modulus of elasticity and (B) hardness profile of diamond film with a [B]/[C] ratio of 10,000 ppm in the gas phase and the longest process time of 12 hours [MR4].

The modulus of elasticity and hardness exhibit nonlinear dependence on the load applied to the Berkovich indenter. Decreasing the maximum load during the nanoindentation test results in an increase in both modulus of elasticity and hardness. Additionally, the effect of the indentation size, where the hardness changes as the size of the indentation decreases, is observed in Fig. 3.19 [224]. This effect is related to geometrically necessary dislocations (GNDs), whose density is inversely proportional to the indentation depth [225]. These dislocations are generated in the tested material to conform to the shape of the indenter and enable crystal rotation. They can be stored in the material and interact with the dislocations generated during the CVD growth of the

diamond film (statistically-stored dislocations, SSDs) [226]. As a result, the hardness, as a function of the indentation depth, can be expressed as a linear combination of the density of geometrically necessary dislocations (GNDs) and statistically stored dislocations (SSDs) [227]:

$$H_{ISE} \propto \sqrt{p_{SSD} + p_{GND}} \tag{3.13}$$

In summary, a nanoindentation test was conducted on a diamond film with [B]/[C] = 10,000 ppm and a thickness of 4.2 μm. It was observed that increasing the maximum load caused a decrease in the hardness and elastic modulus. The maximum hardness of about 65 GPa was obtained for a sample with a deposition time of 12 h. During the measurements, the effect of the indentation size related to geometrically necessary dislocations was observed.

3.8. Electrochemical studies of free-standing diamond films

3.8.1. Cyclic Voltammetry and Chronoamperometry

To analyse the electrochemical behaviour of the fabricated FBDDF, cyclic voltammetry was first carried out. The working electrode was a diamond film, the counter-electrode was a platinum wire, and the reference electrode was an Ag/AgCl electrode. The measurements were performed in a 1M KNO_3 electrolyte and using a potentiostat-galvanostat (VMP-300, BioLogic, France). The results are shown in Fig. 3.20.

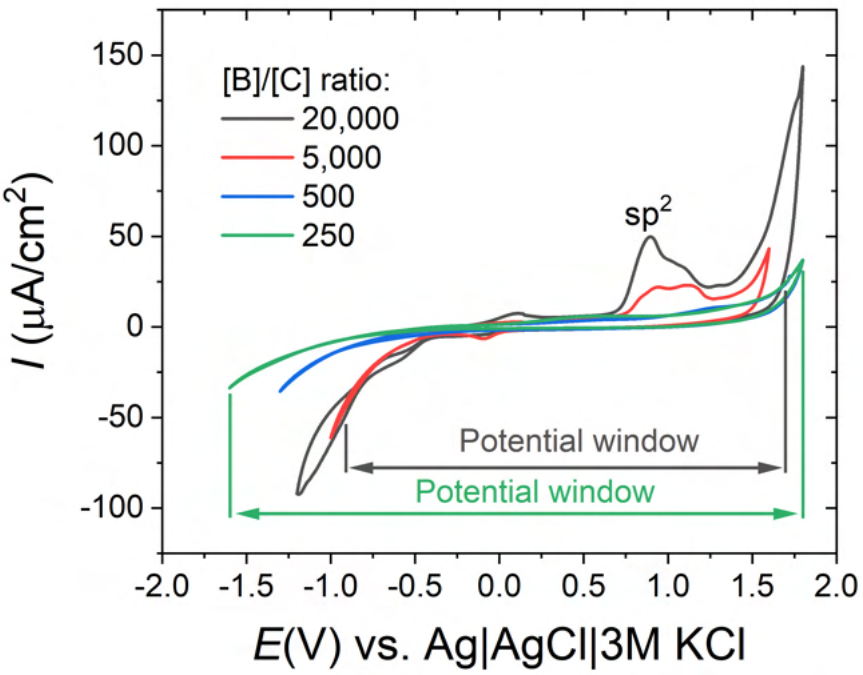

Fig. 3.20. Electrochemical window of FBDDF as a function of the boron concentration in the gas phase for boron-doped diamond films.

All CVD-grown diamond films show similar electrochemical behaviour between 0.75V and -0.5V. Samples with [B]/[C] ratios of 20,000 ppm and 5,000 ppm have the lowest potential for hydrogen and oxygen evolution reactions within the given potential windows. The electrochemical activity and current density increase with higher doping levels. The widest potential window was observed for samples with [B]/[C] ratios of 250 ppm and 500 ppm. This is caused by a lower content of the sp^2 phase at their surfaces [228, 229].

To compare the behaviour of the electrodes over time, boron-doped diamond film was tested with a time interval of 722 days (Fig. 3.21). The results indicate that the electrochemical behaviour of the sample is slightly affected by exposure to oxygen, resulting in a wider potential window, which is in agreement with the results obtained for boron-doped diamond [215, 230]. Spontaneous oxidation occurs when the FBDDF are exposed to air. It is worth adding that similar results can be obtained for anodic oxidation [231].

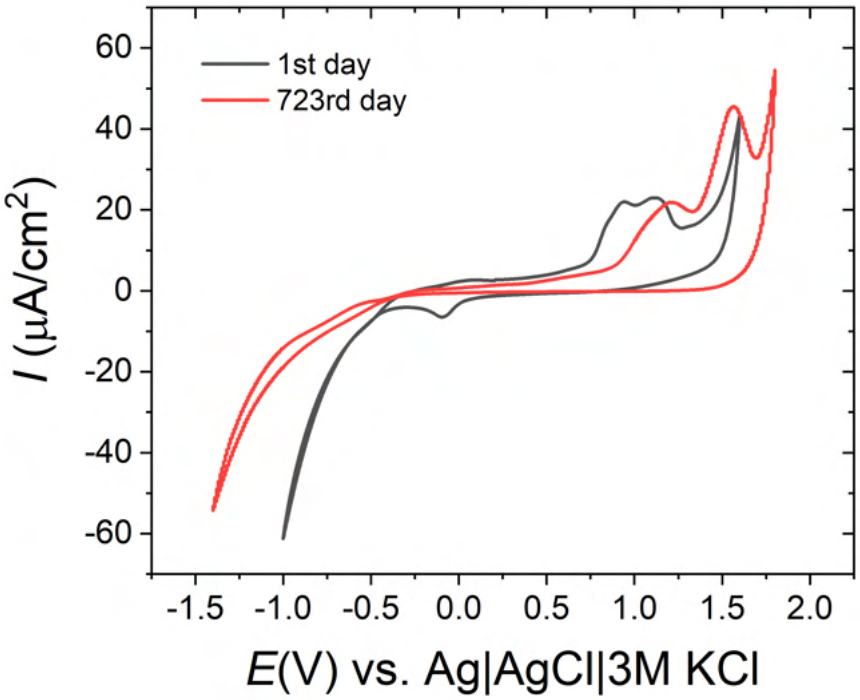

Fig. 3.21. Variation of potential window over time in 3M KCl for a boron-doped diamond film with [B]/[C] = 5,000 ppm. The CVD growth time did not exceed 3 hours.

To analyse electrochemical activity of the top and nucleation side of boron-doped diamond films, scan rate studies studies were carried out in 0.5M Na_2SO_4 electrolyte containing 5 mM K_4FeCN_6. Scan rates in the range of 10-100 mV/s were used. The results for the samples with [B]/[C] = 10,000 ppm and 20,000 ppm concentration in the gas phase are shown in Fig. 3.22. The measurements were performed using a PGStat 128 N potentiostat (Metrohm Autolab, The Netherlands).

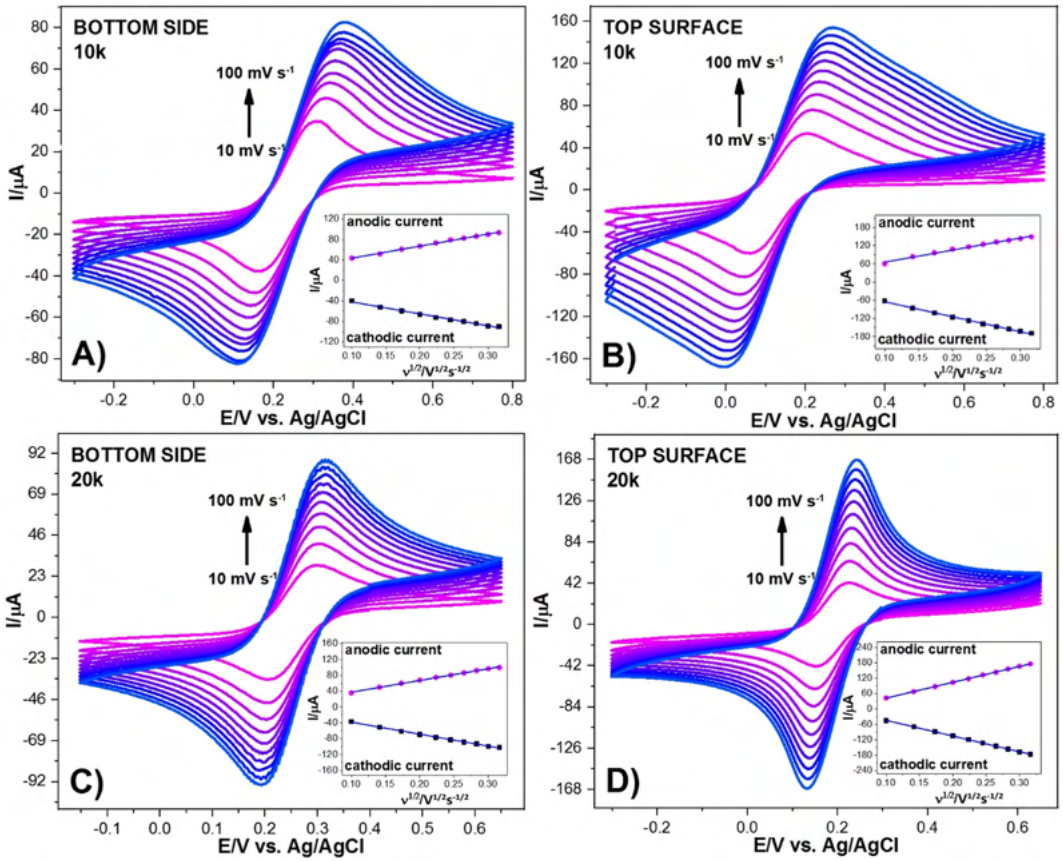

Fig. 3.22. Cyclic voltammograms of the 5 mM $Fe(CN)_6^{3-/4-}$ redox system in 0.5 M Na_2SO_4 were recorded for FBDDF at different scan rates. The results for the nucleation and growth sides of [B]/[C] = 10,000 and 20,000 ppm are shown in Figs. (A,C) and (B,D), respectively. Insets present the anodic and cathodic peak currents plotted against the square root of the scan rates [MR5].

The highest peak-to-peak separation of 149 mV at a 10 mV/s scan rate was found for the nucleation side of the 10,000 ppm film, while the top surface of the 20,000 ppm film showed the lowest peak-to-peak separation (73 mV). This means that the film with the lowest peak-to-peak separation exhibits the fastest electron transfer between the marker in the solution (in this case, $Fe(CN)_6^{3-/4-}$) and the electrode. Furthermore, the 20,000 ppm film exhibited the highest reversibility of the electrochemical process, since the peak-to-peak separation should be 57 mV for an electrochemically reversible process [161].

The top surfaces of the diamond films exhibited higher kinetics of the Faraday process than the nucleation sides, with higher peak currents. This suggests a higher charge transfer resistance of $Fe(CN)_6^{3-/4-}$ oxidation/reduction or a reduced reaction surface area for the nucleation side. Furthermore, an increase in the boron content of the diamond lattice results in an increase in capacitance [MR5]. The observed differences in electrochemical behaviuor can be attributed to various factors, including the sp^3/sp^2 ratio of the layers, crystal size, crystallographic orientation, boron concentration, or type of surface termination [232–237].

In summary, low-doped boron diamond films have a wider potential window, lower electro-

chemical activity, and current density compared to higher-doped samples. A longer exposure of FBDDF to oxygen results in a wider potential window and lower current values at certain voltages. An increase in the boron concentration results in higher Faraday process kinetics on the top surfaces of FBDDF compared to the nucleation side, which is agreement with the results for boron-doped polycrystalline diamond [197]. Additionally, the growth surface has a higher capacitance, which can be utilized in electrochemical double layer capacitors [238].

3.8.2. Mott-Schottky studies

Electrochemical impedance measurements were carried out to investigate the acceptor density (N_A) of the diamond films and evaluate the flat band potential (E_{FB}) at the semiconductor-electrolyte interface using an impedance analyser included in a potentiostat (VMP-300, BioLogic, France). These studies were performed using a 0.5 M Na_2SO_4 solution within a potential range of -1 to 0.8 V. The amplitude of the signal was 10 mV, and the frequency ranged from 30 kHz to 100 Hz. The inverse square capacitance as a function of applied potential for CVD-grown diamond film with [B]/[C] = 500 ppm and growth time = 3 h is shown in Fig. 3.23. The measurements were conducted on samples without metallic conductivity ([B]/[C] < 20,000 ppm). The acceptor density for FBDDF with [B]/[C] = 20,000 ppm was determined based on the Raman spectra (section 3.4).

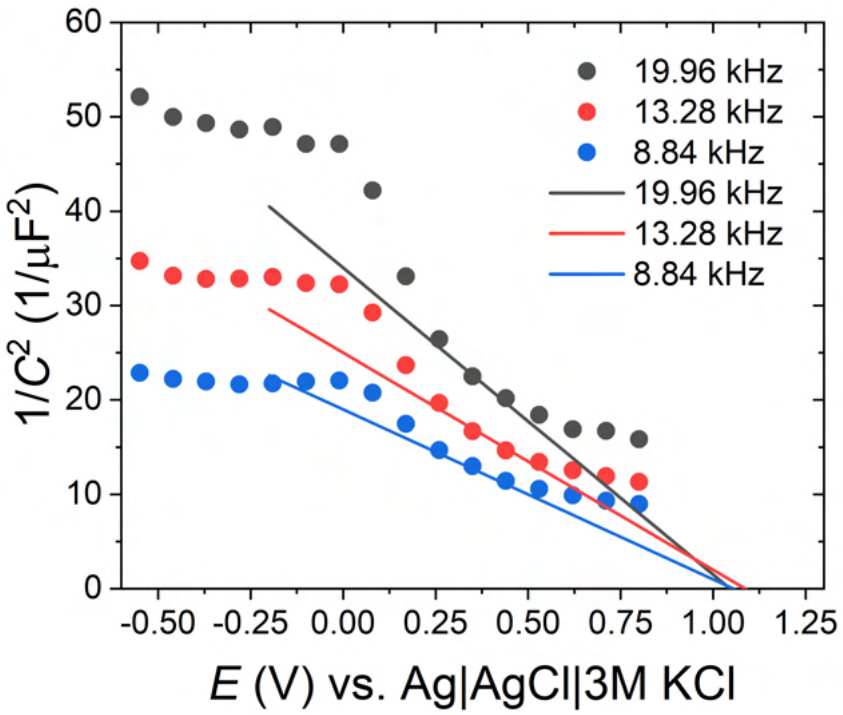

Fig. 3.23. Results of Mott-Schottky analysis for the growth side of boron-doped diamond with [B]/[C] = 500 ppm and a growth time of 3 h.

The observed variations in the slope and deviation of the points of the presented curves

may be attributed to either the presence of distributed resistance at a rough interface that separates two phases with different conductance, as reported in the literature [239–241], or a non-uniform carrier flow [242].

The flat band potential and acceptor concentration are calculated according to the equation:

$$\frac{1}{C^2} = \frac{2}{e\epsilon_0\epsilon_r N_A} \cdot (U - E_{FB} - \frac{kT}{e}) \tag{3.14}$$

where C is assumed to be the space-charge region capacitance, e is the electron charge, ϵ_r is the dielectric constant of diamond film, ϵ_0 is the permittivity of free space, U is defined as the applied voltage, k is Boltzmann's constant, and T is the temperature. The calculated acceptor density and flat band potential are listed in Table 3.5.

Table 3.5. Variation of acceptor density and flat band potential as a function of boron doping.

[B]/[C] in the gas phase (ppm)	N_A (atoms/cm^3)	E_{FB} (V)
250	$1.22 \cdot 10^{18}$	0.62
500	$4.31 \cdot 10^{18}$	1.14
1,000	$1.22 \cdot 10^{19}$	1.59
5,000	$3.16 \cdot 10^{19}$	3.85
10,000	$1.26 \cdot 10^{21}$	4.12

The calculations take into account the shift of the flat band potential by a potential of ΔE, which is given by the equation [242]:

$$\Delta E = \frac{e\epsilon_0\epsilon_r N_A}{2C_H^2} \tag{3.15}$$

where C_H (Helmholtz capacitance) is equal to 20μF cm^{-2} [243]. This equation was used because the calculated flat band potential assumes a potential-independent drop across the Helmholtz layer, which is not accurate for degenerated semiconductors [243]. The increase in the potential drop, as shown in Table 3.5, is associated with a higher presence of oxygen groups and a reduction of hydrogen atoms on the surface and subsurface [244–247]. Values from 0.99 to 0.49 V for H-terminated surfaces and from 3.73 to 2.65 for O-terminated surfaces (vs Ag/AgCl) are obtained for diamond films [244]. As a result, samples with lower doping have more hydrogen atoms on the surface and an increased carrier density is observed near it [245]. The factor affecting the level of oxidation is content of the sp^2 phase on the diamond surface [232,244,248]. It should be noted that these findings for highly boron-doped diamond must be taken with care, since the potential drop occurs primarily on the solution part of the interface [245]. Additionally, electrochemical impedance measurements were carried out at the final stage of the experiment, rather than immediately after

the diamond growth and the samples were not stored in an oxygen-free atmosphere. The results confirm the information obtained from Raman spectroscopy that the higher the [B]/[C] ratio in the gas phase, the more boron is incorporated into the diamond lattice. However, the results obtained for [B]/[C] = 10,000 suggest that the sample should exhibit metallic-like behaviour, which is not confirmed by the studies presented in section 3.6. It is important to note that electrical and chemical measurements require different sample preparation methods. Therefore, two samples from the same process were used; the first for performing the electrical measurements and the second for the electrochemical studies. Due to the inhomogeneous boron doping [MR3], it can be concluded that the samples produced at this boron concentration are on the borderline between metallic-like and semiconducting behaviour.

To sum up, the Mott-Schottky analysis showed that films with higher boron content are more oxidised. In addition, these measurements confirmed the Raman spectroscopy results that a higher boron content in the gas phase leads to greater boron incorporation into the diamond lattice.

3.9. Conclusions

Before fabricating the diamond heterostructures, it was necessary to synthesise diamond films. Microwave Plasma-Assisted Chemical Vapour Deposition technology was used for this purpose. Due to a mismatch in the thermal expansion coefficients, the boron-doped diamond film delaminated from the tantalum surface after CVD growth, resulting in the formation of a free-standing film. The gas concentrations and process time were varied to study their influence on the parameters of the films. The morphological, electrical, electrochemical, and mechanical properties of the fabricated films were determined.

An increase in the concentration of diborane during CVD growth results in a higher boron concentration in the diamond lattice, as confirmed by a shift of the diamond line towards lower frequencies and the appearance of new bands in the Raman spectra of the fabricated films. **Highly doped films exhibit lower resistance, and samples with [B]/[C] = 20,000 ppm in the gas phase and a growth time of 3 hours demonstrate metallic conductivity, which confirms the H1 hypothesis of this dissertation.** Lower boron-doped samples show two conductivity mechanisms: thermal activation from the valence band to the impurity band at high temperatures and variable range hopping at lower temperatures. The resistivity values obtained for similar concentrations of boron in the gas phase were higher compared to those reported previously for free-standing films [126, 131]. However, it should be noted that the fabricated samples in this study were more than 100 times larger than diamond membranes [131], and the non-uniform incorporation of boron into the samples had a significant impact on the observed conductivity values. The calculated carrier mobilities of free-standing diamond films decrease from 421 to 0.16 $cm^2\ V^{-1}s^{-1}$ as the

concentration of boron in the diamond lattice increases. The mobility values for [B]/[C] < 10,000 ppm in the gas phase were higher than for nanocrystalline films on quartz and comparable to those for [B]/[C] ≥ 10,000 ppm [38]. Higher boron-doped films exhibit a narrower potential window and higher electrochemical activity compared to lower boron-doped samples, and sp^2 peaks appear in their electrochemical potential windows, which is in agreement with the results obtained for boron-doped diamonds [249].

With the increasing boron doping, the surface roughness decreases. However, the nucleation side (in direct contact with tantalum during CVD growth) still exhibits lower surface roughness and more defects compared to the growth side. Furthermore, the top surface exhibits higher capacitance, conductance, and Faraday process kinetics than the nucleation side. This is attributed, among other factors, to a lower boron incorporation caused by residual oxygen in the chamber during the initial stage of CVD growth, as observed in previous studies on free-standing films [147].

Raman and electrical mapping studies have confirmed that doping is a heterogeneous process that can be controlled by varying the methane concentration and growth time. The hardness of the sample that underwent the longest CVD growth time was approximately 65 GPa, which is consistent with the findings of previous studies on nanocrystalline films [134, 195].

The above research required the development of new transfer techniques. The method, utilising PDMS and Kapton, is suitable for larger electronic devices, while the procedure that uses a transfer stage allows for fabrication with micrometric precision.

4. DIAMOND-COMPOSED HETEROSTRUCTURES

This chapter presents the heterostructures produced using diamond films. The application of diamond in heterostructures with other materials not only enables the tuning of diamond's electronic properties but also provides an excellent platform for enhancing or modifying the functionalities of the combined material [250]. A summary of the fabricated devices can be found in Table 4.1.

Table 4.1. Fabricated diamond-composed heterostructures.

ID	[B]/[C] ratio (ppm)	Growth time	Material	Application
Diamond-C:H:N:O	10,000	12 h	C:H:N:O	Durable electrode
Diamond-PDMS	0–20,000	3 h	Polydimethyl-siloxane	Transparent electrode
Diamond-Kapton	10,000	5 h	Polyimide	Strain sensor
Diamond-Graphene	500 and 20,000	3 h	Graphene	Electronic junction
G-PLA-NDF	500 and 10,000	5 h	Graphene and Polylactic acid	TNT sensor and Capacitor
Diamond-Black Phosphorus	0	1.5 h	Black phosphorus	Transistor

All of the heterostructures presented here, except for Diamond-C:H:N:O and Diamond-Graphene, were fabricated at the home department by the author of this dissertation. For the Diamond-C:H:N:O heterostructures, the diamond films were sent to the University of South Bohemia (Czech Republic) for the deposition of the C:H:N:O layer. The samples were then returned and tested in Gdańsk. The diamond-graphene heterostructures were fabricated during an internship with Professor Buijnsters' group at Delft University of Technology in collaboration with Professor Steeneken's group. In this study, the author was responsible for designing and fabricating the upper part of the device using diamond film. For the lower part of the device, which was fabricated using graphene, the author participated in the analysis and interpretation of the results obtained.

The Faculty of Mechanical Engineering at Gdańsk University of Technology performed the nanoindentation tests on the Diamond-C:H:N:O heterostructures, while Nanores (Wrocław, Poland) performed the scanning electron microscopy on the G-PLA-NDF (Graphene-Polylactic acid-Diamond). The author of this dissertation was involved in analysing and elaborating on the results obtained from both sets of tests.

The electrical and electrochemical measurements of the G-PLA-NDF heterostructures were performed in collaboration with employees of the Department of Metrology and Optoelectronics at Gdańsk University of Technology. During the collaboration for this study, the author was involved in

conducting the measurements and actively participated in the analysis and interpretation of the results obtained. Furthermore, the author of the research elaborated on the data obtained from the analysis of the capacitor.

The rest of the measurement results for all fabricated heterostructures, including those from electrical, optical tests, and the Raman spectroscopy, were obtained personally at Delft University of Technology and Gdańsk University of Technology. In these cases, the author was responsible for analysing, interpreting, and developing the measurement results, as well as designing and implementing the measurement and transfer systems presented in this chapter.

4.1. Diamond-C:H:N:O (Nylon-like) heterostructures

The use of nylon-like films makes it possible to achieve flexible and transparent electrodes [251]. The composite structure is less brittle and fragile compared to free-standing diamond film. The procedure of fabricating the nylon-coated boron-doped diamond film for the mechanical tests is shown in Fig. 4.1.

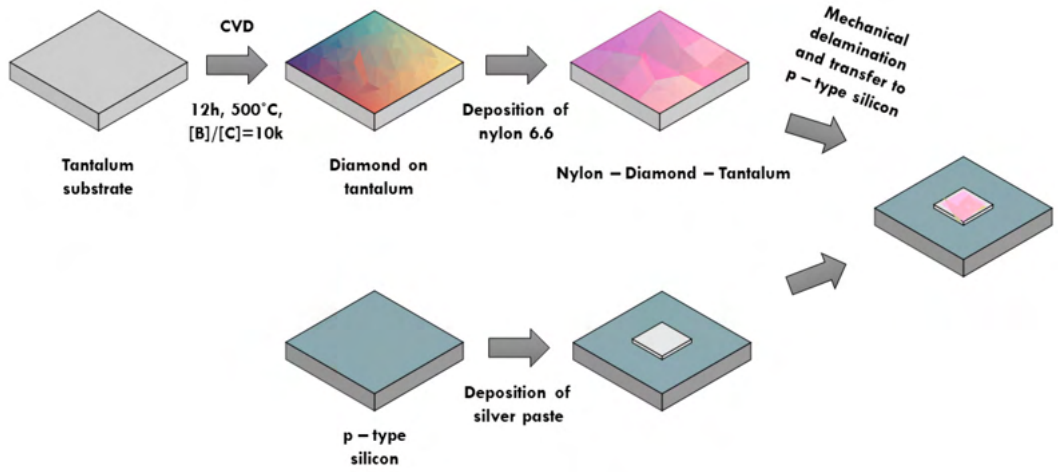

Fig. 4.1. Fabrication process of boron-doped diamond-C:H:N:O heterostructure for nanoindentation tests [MR4].

In the first step, boron-doped free-standing diamond film was synthesized on tantalum using the Microwave Plasma Assisted Chemical Vapour Deposition system at Gdańsk University of Technology. The growth time was 12 h and the [B]/[C] ratio in the gas phase was 10,000 ppm. As a result, the thickness of the film is 4.2 μm. The mechanical properties of this film are presented in section 3.7.

Next, C:H:N:O (nylon-like) film was deposited on the fabricated boron-doped diamond film via a 3" balanced magnetron equipped with a nylon 6.6 target (Goodfellow, Germany). The temperature of the substrate did not exceed 50 ℃ during the process. A radio-frequency generator working at a frequency of 13.56 MHz was used to deliver 50 W of power to the dielectric target

after pressure stabilisation ($5{\cdot}10^{-4}$ Pa). The deposition rate was approx. 8.4 ± 0.8 nm/min.

Due to delamination of the diamond film from the tantalum, it was possible to transfer the diamond:C:H:N:O structure to the surface of a silver paste (EPO-TEK H20E, Epoxy Technology, USA) deposited on silicone. The next step was to cure it for 3 hours in a vacuum oven (DZ-2BC II, Chemland, Poland) at 80℃. The SEM images of the heterostructure produced, obtained using an S-3400 N (HITACHI, Japan), are shown in Fig. 4.2.

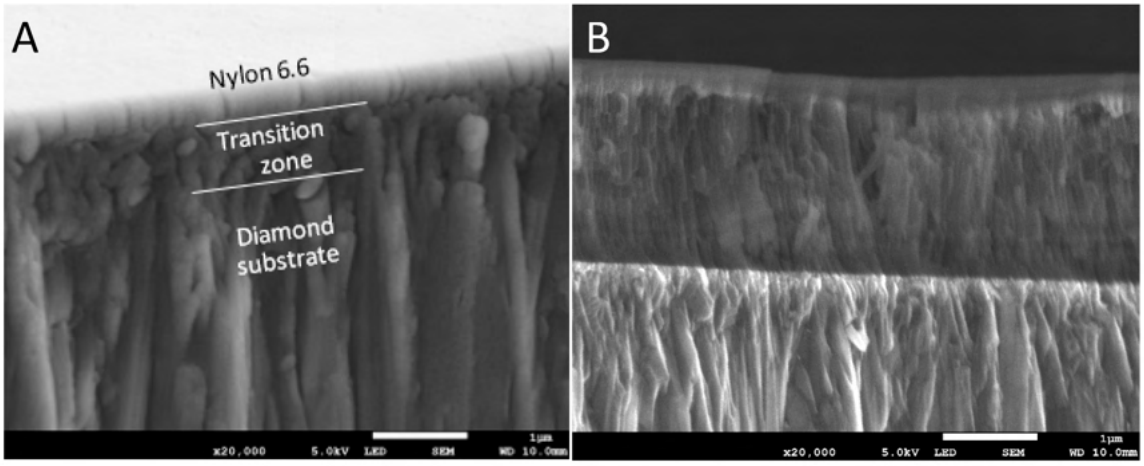

Fig. 4.2. Cross section of the diamond-C:H:N:O heterostructure. The thickness of the C:H:N:O is (A) 500 nm and (B) 2 μm [MR4].

As a result of the experiment, nylon covered most of the area. However, cracks induced by the roughness of the nanodiamond surface (section 3.5) are present. They are isotropic, which is common for films thicker than the size of grains [252]. Moreover, there is a transition zone between the C:H:N:O and the diamond film, whose hardness is higher than that of the nylon coating and lower than that of the diamond (Fig. 4.3).

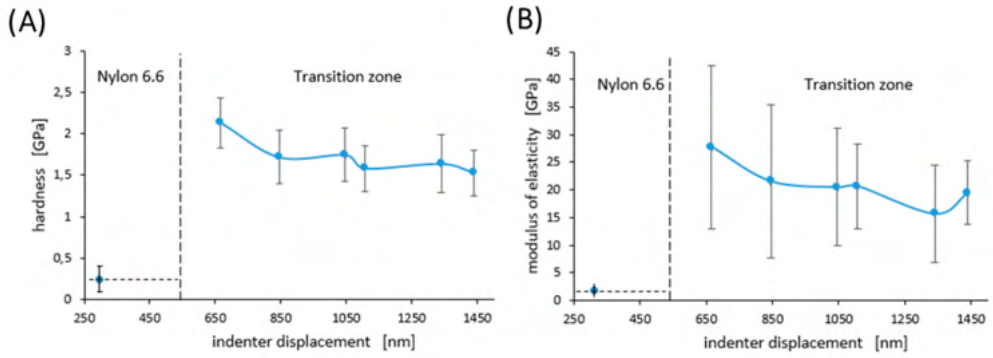

Fig. 4.3. Hardness (A) and modulus of elasticity (B) were measured for the 500 nm nylon coating and the transition zone. The results were acquired using a NanoTest Vantage (Micro Materials, United Kingdom) [MR4].

In summary, the deposition of C:H:N:O on the diamond surface resulted in a more durable and less fragile structure compared to the diamond film alone. This effect facilitated the transfer of

structures using tweezers. Additionally, it was shown that a transition zone with different mechanical properties can be fabricated between the diamond and polymer by sputtering polymer layers, however, the roughness of the growth surface induces isotropic cracks.

4.2. Diamond-Polydimethylsiloxane heterostructures

Polydimethylsiloxane (PDMS) is a material commonly used for transferring 2D materials [253, 254]. It also has a high transmittance of over 70% for the range of 400–1100 nm [255]. The mechanical properties of PDMS can be influenced by several factors, including the curing temperature, stress, and mixing ratio [255, 256]. It is possible that a free-standing diamond film transported on the surface of PDMS could enable simultaneous electrochemical and optical detection of the specific compounds [257].

The method illustrated in Fig. 3.2 (b) was used to fabricate the Diamond-PDMS structure. However, instead of Kapton, commercially available PDMS (PF X-4, Gel-Film) was used. The absorbance and optical band gap results for the diamond films with varying doping levels on PDMS are presented in Table 4.2. The optical band gaps were determined by identifying the intercept of the linear portion of the Tauc plot at $\alpha = 0$. To construct the Tauc plot, $(\alpha h\nu)^{\frac{1}{2}}$ was plotted against the photon energy $(h\nu)$. Here, α represents the optical absorption coefficient of the diamond films (calculated from the absorption spectra), h denotes Planck's constant, and ν represents the frequency of the photons.

Table 4.2. Optical band gap and absorbance of the diamond films on PDMS as a function of [B]/[C] ratio in the gas phase during CVD growth. Optical absorbance measurements were taken using a UV-9000 Metash system with a scan step of 1 nm in the range of 340 nm to 1100 nm [MR1].

[B]/[C] ratio in the gas phase (ppm)	Optical band gap (eV)	Absorbance (a.u.)		
		400 nm	700 nm	1000 nm
0	2.34	0.26	0.17	0.14
250	2.32	0.32	0.18	0.16
500	2.30	0.38	0.22	0.19
1000	2.09	0.33	0.22	0.20
5000	1.97	0.33	0.35	0.44
10 000	1.50	0.44	0.63	1.03
20 000	*	0.75	0.94	0.88

* FBDDF with a [B]/[C] ratio of 20,000 ppm exhibits metallic-like conductivity, and it was not possible to determine the optical band gap for this sample.

The optical band gap increases as the [B]/[C] ratio in the gas phase decreases (Table 4.2). This increase in the optical band gap is accompanied by an increase in ordered sp^3 carbon [258]. For undoped diamond, the optical band gap is 2.34 eV, while for [B]/[C] = 10,000 ppm, it is 1.50 eV. The low value, compared to single-crystal diamonds, is correlated with the size of sp^2 clusters, and their decrease causes an increase in the optical band gap of the diamond films [259–261]. Moreover, the H-terminated surface induces a p-type channel under atmospheric conditions, which

affects the value of the optical band gap [262].

The absorbance values obtained for the diamond film (B]/[C] = 20,000 ppm and 3 hours of CVD growth) with various methane concentrations in plasma are presented in Table 4.3.

Table 4.3. Absorbance of diamond films ([B]/[C] = 20,000 ppm and 3 hours of growth) on PDMS as a function of the methane concentration in the gas phase during CVD growth.

Methane concentration	**Absorbance (a.u.)**		
in the gas phase (%)	**400 nm**	**700 nm**	**1000 nm**
1	0.75	0.94	0.88
2	0.91	1.29	1.21
4	1.70	1.63	1.24

The samples synthesised with higher methane concentrations exhibit increased thickness, longer path lengths, and higher absorbance values. These properties are further influenced by variations in the boron concentration and the presence of defects (section 3.4), which in turn affect the samples' optical properties [263]. As a result, the absorbance value increases from 0.88 to 1.24 at 1000 nm, and from 0.75 to 1.7 at 400 nm for methane concentrations of 1% and 4%, respectively.

The obtained results are in agreement with those reported in [54, 264], where an increase in the dopant and methane concentration led to a decrease in the transmittance of the films. In comparison to Ficek et al. [54], who deposited boron-doped diamond layers on quartz, diamond films present lower values of the optical band gap. This is attributed to the longer process time, higher doping efficiency, and increased layer thickness of free-standing diamond [54, 265, 266]. Furthermore, the diamond-PMDS structures showed higher electrical conductivity.

In contrast, Stotter et al. [263] reported higher absorption values for samples with comparable thickness and a 10 ppm B_2H_6 concentration than for diamond films on PDMS with [B]/[C] = 1000 ppm in the gas phase. However, it should be noted that a different reactor, gas concentration (a total gas flow of 100 sccm), substrate temperature (800 °C), and microwave power (600 W) were employed in their study.

To conclude, Diamond-PDMS heterostructures were fabricated. By varying the boron and methane concentrations in the gas phase during CVD growth, it is possible to tune the optical band gap of the samples. The absorbance of the undoped sample did not exceed 0.3 in the visible range. The resulting transparent electrodes have the potential to be used in simultaneous electrochemical and optical detection devices.

4.3. Diamond-Polyimide devices

The diamond film transferred onto the Kapton surface, as shown in Fig. 3.2, opens up new possibilities for using boron-doped diamond to fabricate strain sensors. In order to analyse the resistance as a function of strain, a measurement system was designed, as presented in Fig. 4.4.

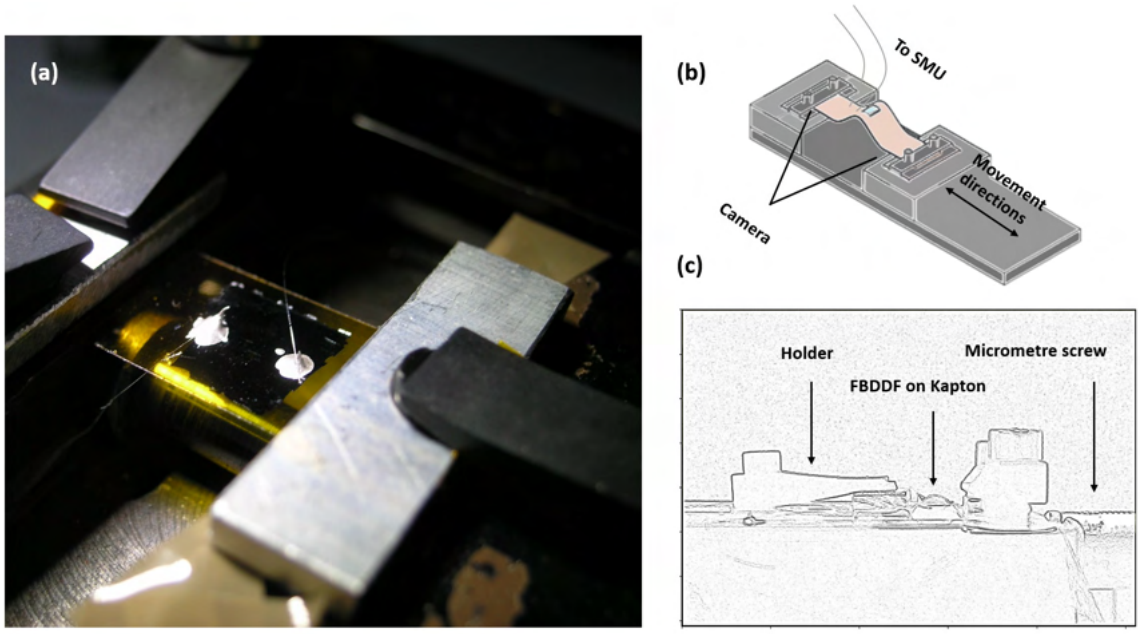

Fig. 4.4. (a) Diamond film on Kapton with connected platinum wires [MR3], (b) Schematic of the measuring system, (c) Photo of bent diamond film. An edge filter was applied.

After 5 hours of growth, the free-standing diamond film (with a [B]/[C] ratio of 10,000 ppm in the gas phase and a thickness of 1.5 μm) was transferred onto a Kapton substrate with a thickness of 25 μm (as shown in Fig. 3.2 (b)) and mounted onto a stage that moves along only one axis.

Platinum wires were then connected to the diamond film using silver paste (EPO-TEK H20E, Epoxy Technology, USA), which was cured for 18 hours in a vacuum oven (DZ-2BC II, Chemland, Poland) at 70℃ (as shown in Fig. 4.4 (a)). Next, the platinum wires were connected to a source/measure unit (2400, Keithley, USA). Strain was introduced using a micrometer screw, and the bend radius was imaged using a CMOS camera (DCC1240C, Thorlabs, USA) with a 1.8/125 mm lens (Meopta Largor, Czech Republic) (as shown in Fig. 4.4 (b)). To facilitate the calculations for some samples, an edge filter was applied using Python software version 2.7.2 (as shown in Fig. 4.4 (c)). The measurements were performed at room temperature (22℃ and 44 % RH).

The results of the electromechanical measurements are presented in Fig. 4.5. The strain was calculated according to the equation [267]:

$$\epsilon_s = \frac{d_f + d_s}{2r} \tag{4.1}$$

where d_f is the film thickness, d_s represents the substrate thickness and r is the radius.

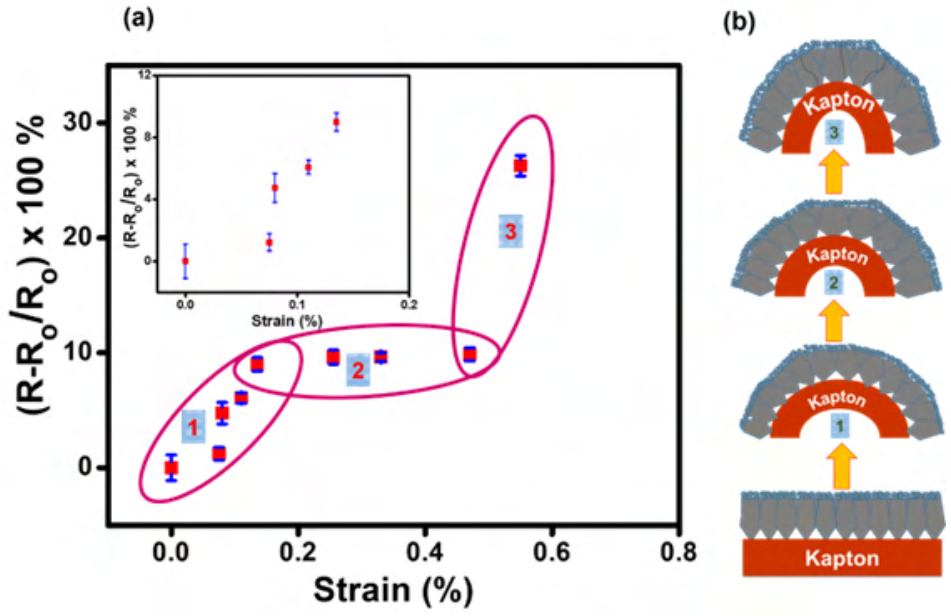

Fig. 4.5. (a) Normalised resistance of Diamond-Kapton as a function of the applied strain, (b) Schematic representation of heterostructure before and during the bending [MR3].

The application of stress causes the electrical resistance of the diamond film to increase. Moreover, the response is nonlinear and the device changes in three different stages.

'Stage 1' (Fig. 4.5 (b)) corresponds to the elongation of the diamond film grains, which generates tensile stress during the mechanical bending process. The externally applied strain induces an increase in the distance between the conductive grains and sp^2 clusters, resulting in an increase in the distance between the conductive states. Additionally, boron precipitation occurs at the grain boundaries, and the existence of dislocations suppresses grain boundary relaxation [268]. As a result, the resistance of the device increases.

In 'stage 2', there is a minor change in the residual resistance. The distance between the grains and sp^2 clusters could reach saturation and may no longer have a further influence on the electrical properties of the device.

The developed device was able to withstand measuring up to 0.55% strain. Further increments in strain lead to cracks forming on the diamond film and damage to the device ('stage 3'). However, the Diamond-Kapton device shows great potential for use in sensitive low-strain sensor applications. Further analysis is present in [MR3].

A comparison of selected strain sensors and the fabricated diamond device is shown in Table 4.4. The gauge factor was calculated by dividing the relative change in resistance ($\Delta R/R$) by

the applied strain (ϵ_s), as shown in the equation:

$$GF = \frac{\frac{\Delta R}{R}}{\epsilon_s} \tag{4.2}$$

where R represents the initial resistance of the device.

Table 4.4. An evaluation of strain sensors made from various materials.

Sensor	Strain range (%)	Linearity	Gauge Factor	Reference
Laser-Induced Graphene on PDMS	30	Linear	160	[269]
PDMS-BP-Paper	3	Nonlinear	6.1	[270]
MoS_2 on SiO_2	-0.03	Linear	104.26	[271]
Ag-PDMS	36	Linear	939	[272]
Graphene-PET	1.6	Linear	546	[273]
Graphene-PDMS	7.1	Two linear regions	2.4–14	[274]
This work	0.55	Nonlinear	16.26–66.74	[MR3]

The Diamond-Kapton device exhibits higher gauge factor values compared to devices made of graphene or black phosphorus. It should be noted that even higher gauge factor values can also be achieved by increasing the doping and conductivity of the sample (equation 4.2). Additionally, the strain range can be modified by altering the thickness of the films.

In summary, FBDDF films were used to fabricate a strain sensor with a nonlinear response that can sustain up to 0.55% of strain. The maximum obtained gauge factor was 66.74, but higher values may be obtained with more highly doped samples. However, the strain range was wider compared to MoS_2 on SiO_2 devices, with a gauge factor higher than that of Graphene-PDMS or PDMS-Black Phosphorus-Paper devices [270, 271, 274].

4.4. Diamond-Graphene

As mentioned in the introduction, the interactions between graphene and boron-doped diamond have not been fully explored. This chapter aims to study the interaction of low and highly boron-doped diamond with this two-dimensional material. Before fabricating diamond-graphene devices, research was conducted on graphene produced by various methods, including chemical vapour deposition on copper, silicone dioxide, molybdenum, and graphite exfoliation.

Exfoliated graphene has high carrier mobility and a low D-to-G band ratio (I_D/I_G), which is advantageous compared to other methods of fabrication [275–278]. However, the surface area is relatively small and the procedure to achieve a monolayer is time-consuming.

Chemical vapour deposition can be used to obtain graphene with a larger surface area. Fig. 4.6 shows the Raman spectra of graphene deposited directly on silicone dioxide, molybdenum, and copper. The samples on copper and silicone dioxide were obtained from Graphenea (Spain), while the sample on molybdenum was provided by Prof. Vollebregt (Delft University of Technology). The fabrication and transfer procedure of graphene on molybdenum is described in [279]. Graphene on copper shows a lower D-to-G band ratio and a shift of the G line towards lower frequencies compared to graphene directly deposited on silicone dioxide. This shift indicates a lower number of graphene layers [277]. It should be noted that transferring graphene onto copper is a complicated process, as it requires etching the copper and rinsing it in deionised water. Then, the sample must be placed on a hot plate for 12 hours at 120℃. The layer deposited on the surface of molybdenum is characterised by a thickness of 10 nm (as confirmed by AFM studies). In this case, it is not appropriate to refer to this layer as graphene, and the term 'nanographite' is more accurate. One advantage of films deposited on molybdenum is the transfer methodology, which is relatively simple due to the thickness of the layer. After being soaked in 30% H_2O_2 for 12 hours and diluted in deionised water, the sample can be transferred to the desired substrate.

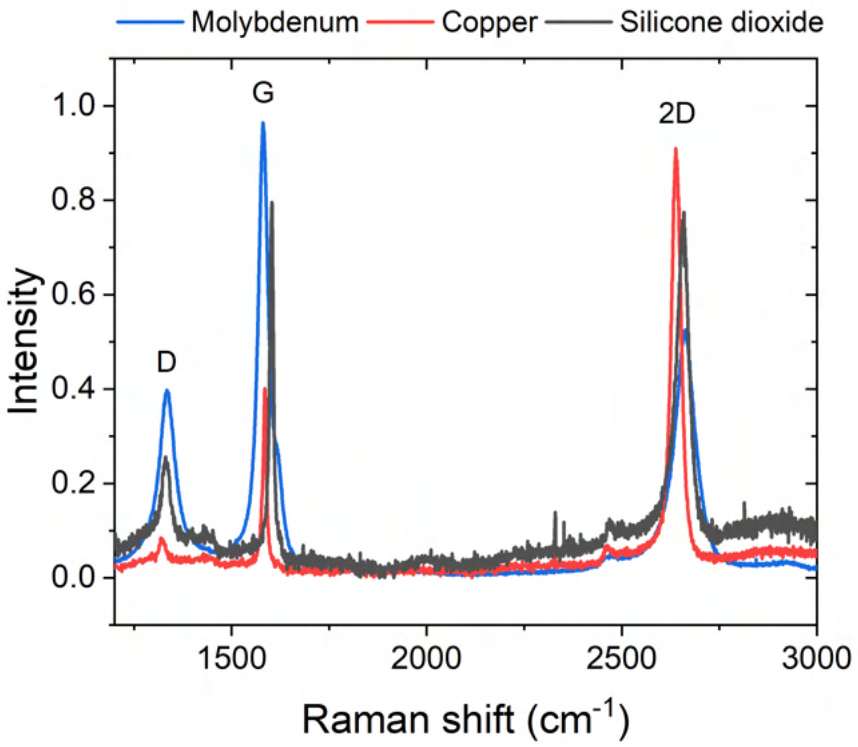

Fig. 4.6. Raman spectra of graphene deposited on silicone dioxide, copper, and molybdenum. The experimental data was acquired utilising a LabRAM HR (Horiba Scientific, Japan). The laser operated at a wavelength of 514 nm, a power of 450 μW.

Since graphene patterning was required at a later stage, it was decided to use graphene on silicone dioxide to reduce the impact of the transfer on the implemented interface.

In the next step, three methods of selective patterning of graphene were compared:

- Scotch tape method using commercially available tape,
- Etching through a mask without resist,
- Etching with resist.

The scotch-tape method allows for the removal of graphene from the surface of silicone dioxide, but significant residues remain, making it unsuitable for later use. With oxygen plasma etching through a mask, etching of the graphene surface occurs under the mask, resulting in a structure that does not meet the dimensional requirements. Additionally, the etching of graphene is not uniform, which can cause short-circuit problems between not fully isolated graphene films. The best results are obtained using a method that involves coating graphene with a layer of resist. The uncovered graphene is then etched using oxygen plasma. The resist is removed using 1-Methyl-2-pyrrolidone, as the use of acetone leads to the removal of both the resist and the underlying graphene layer.

After developing the method for patterning graphene, the fabrication of heterojunctions was initiated, and its procedure is presented in Fig. 4.7.

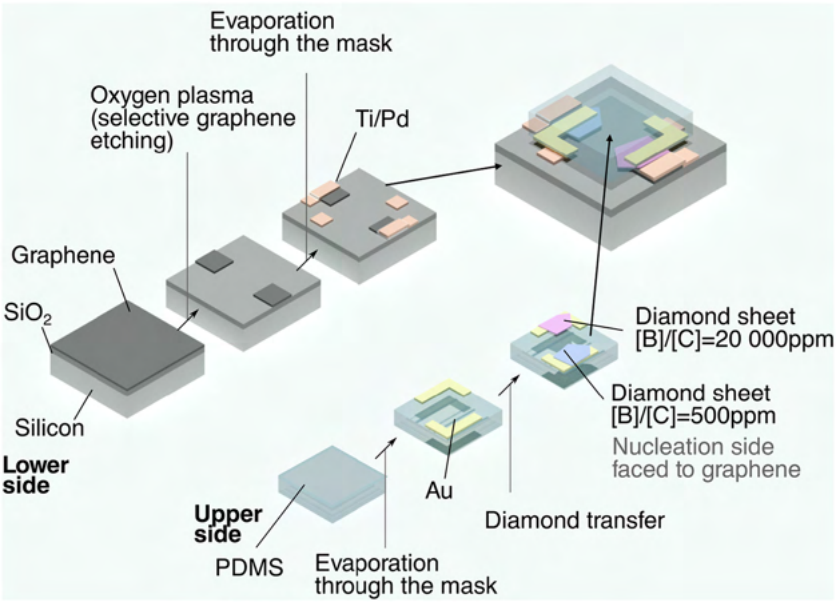

Fig. 4.7. Fabrication procedure of diamond-graphene junctions [MR1].

In the first step, graphene on SiO_2/Si was patterned by lithography and etched by oxygen plasma to form 2.5 μm x 0.8 mm lines (Etchlab 200, Sentech Instruments, Germany). Drain and source contacts were fabricated from 5 nm of titanium and 95 nm of palladium (FC-2000, Temescal, USA). In the last step, free-standing diamond films ([B]/[C] = 500 ppm and 20,000 ppm, growth time = 3 h) with gold contacts (17 nm) on PDMS were transferred onto the graphene surface. The fabricated diamond-graphene device is shown in Fig. 4.8 (a), while the patterned graphene with

and without resist is shown in Figs. 4.8 (b) and (c), respectively.

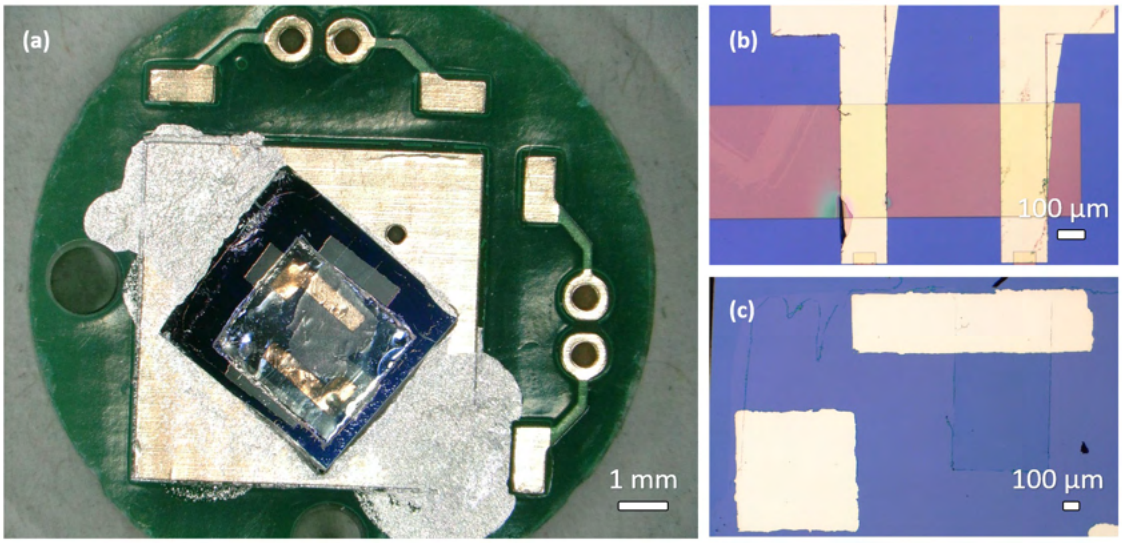

Fig. 4.8. (a) Fabricated diamond-graphene device, (b) Patterned graphene with resist, (c) Uncovered patterned graphene.

The current-voltage characteristics of the fabricated devices were obtained using a probe station (PM5, SÜSS MicroTec, Germany) and a source/measure unit (B2912A, Keysight, USA). These results are presented in Fig. 4.9.

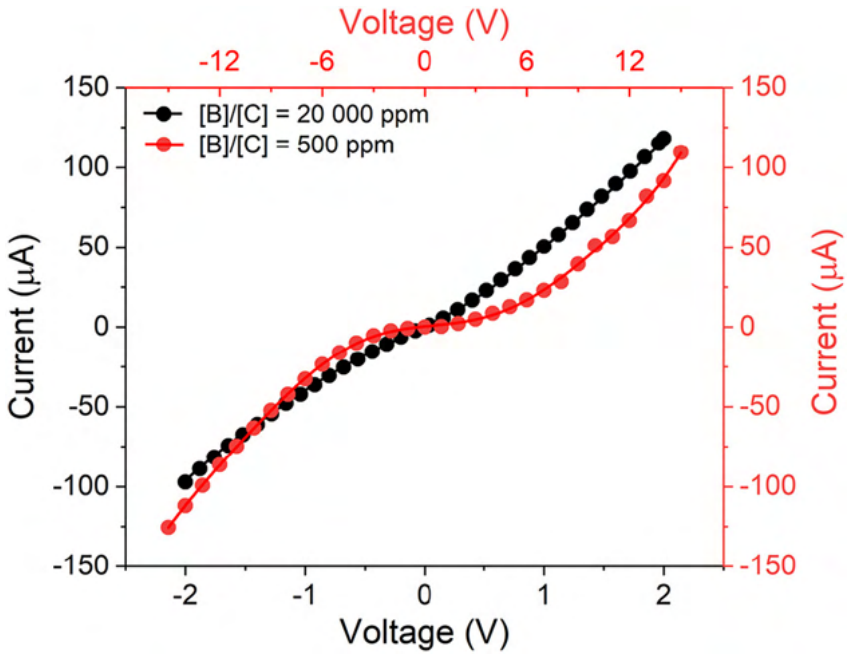

Fig. 4.9. Current-voltage characteristics obtained for diamond-graphene devices with varying boron concentrations during diamond growth [MR1].

The transport of charges is facilitated for the device with higher doping. The obtained current (at 2 V applied voltage) for the device with [B]/[C] = 20,000 ppm is 118 µA, while it is only 2.2 µA for the one realised with [B]/[C] = 500 ppm.

The behaviour of graphene-diamond vertical junctions is influenced by key factors such as the surface termination and boron doping. The work function of the nucleation side of a FBDDF with [B]/[C] = 10,000 ppm, as measured by Kelvin probe atomic force microscopy, was approximately 4.7 eV [MR3]. In comparison, conventional graphene has a work function of 4.61 eV [280]. Doping changes the Fermi level, leading to a decrease in the work function of the diamond film [281]. As a result, the heavily boron-doped film exhibits an almost ohmic contact response, while the heterojunction with a lower boron concentration resembles a Schottky junction. According to Wan et al. [114], the presence of graphene on the hydrogen-terminated diamond surface results in a significant band bending, leading to a reduction in the binding energy of the valence band by approximately 150 meV. Moreover, the lattice defects and sp^2 bonds induced by the dopants should facilitate charge transfer between the materials [115, 116].

The next step involved analysing the impact of oxidation on the diamond film, as shown in Fig. 4.10. To oxidise the free-standing diamond film, an oxygen plasma was used at a gas flow rate of 5 cm^3/min and a power of 80 W for a duration of 5 minutes (using a Zepto Plasma Cleaner by Diener, Germany).

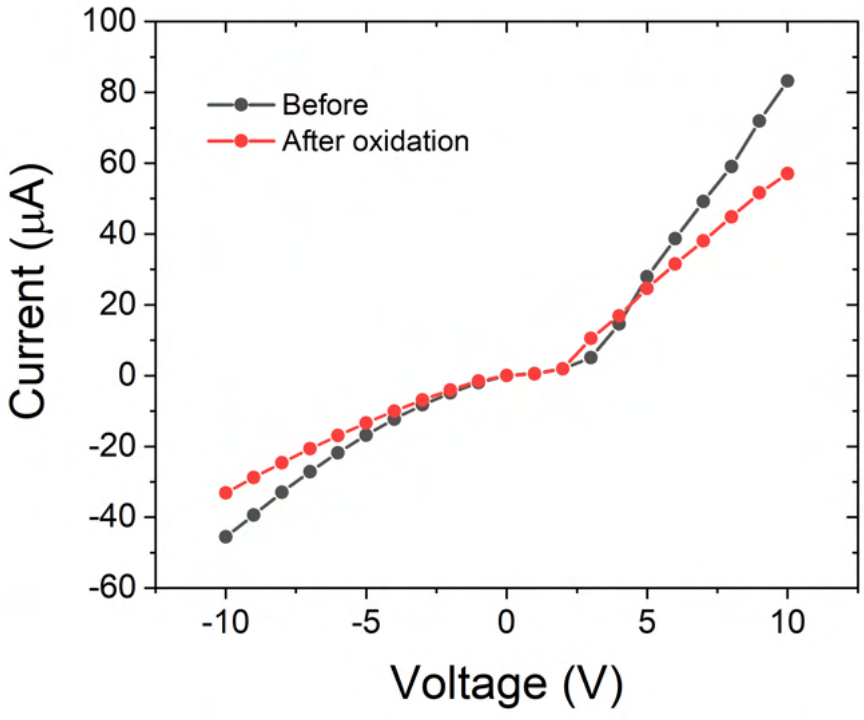

Fig. 4.10. Effect of diamond surface termination on the current-voltage characteristic of diamond-graphene heterostructures.

The surface of the grown diamond films is mostly covered with hydrogen, which leads to the formation of a surface channel that is highly conductive [113]. The oxidation of the diamond surface leads to reduction of surface conductivity [282], and increases the resistance of the whole

structure. However, the character does not transform from a Schottky to an Ohmic junction.

In conclusion, diamond-graphene heterostructures using diamond films with various levels and types of conductivity were successfully fabricated. The results show that the junction using a heavily boron-doped diamond film had an almost Ohmic contact response, whereas the junction with a lower concentration of boron during CVD growth resembled a Schottky junction. Additionally, oxidation of the diamond surface led to a decrease in the conductivity of the entire structure. Further analysis of the diamond-graphene junctions is presented in [MR1].

4.5. Diamond-Graphene-Polylactic acid composite devices

In recent years, there have been significant developments in 3D printing technology. Conductive filaments have emerged in the market that can be used to manufacture sensors and electronic components [283, 284]. However, the conductivity of these filaments is limited by the use of PLA and acrylonitrile butadiene styrene polymers in their structure [285, 286]. The goal is to activate 3D-printed electrodes for detecting nitro-explosive compounds and fabricating electronic components. As mentioned in the Introduction, diamond can be integrated with 3D printing technology. The use of free-standing diamond films should enable the fabrication of capacitors and sensing devices in a quick and cost-effective way. Furthermore, the currently employed methods (for example, for 2,4,6-trinitrotoluene detection), such as chromatographic analyses, are expensive and time-consuming [287, 288].

The procedure for modifying 3D printed graphene-polylactic acid electrodes is illustrated in Fig. 4.11(a). As the diamond delaminates from the tantalum surface, it can be transferred to the printed electrode using tweezers while heating it to 200℃. The required temperature may vary depending on the filament used. In this study, FBDDF with [B]/[C] ratios of 500 ppm and 10,000 ppm were employed, and the growth time was 5 hours. The graphene-PLA electrodes were designed using a CAD application and printed with a 3D printer (Ender 3 Pro, Creality, China). Conductive graphene-PLA filament from Black Magic 3D (USA) was employed as the substrate for the FBDDF.

SEM micrographs of the realised diamond-graphene-PLA structures and their cross-section are shown in Figs. 4.11 (c) and (d), respectively. To analyse the interface, a portion of the diamond film was removed. The G-PLA surface revealed the texture of the top surface of the diamond film, confirming electrical contact between the two layers. No visible gaps were present that could impede the flow of charge. The colour variations in the SEM micrographs are attributable to differences in the surface potentials of the layers.

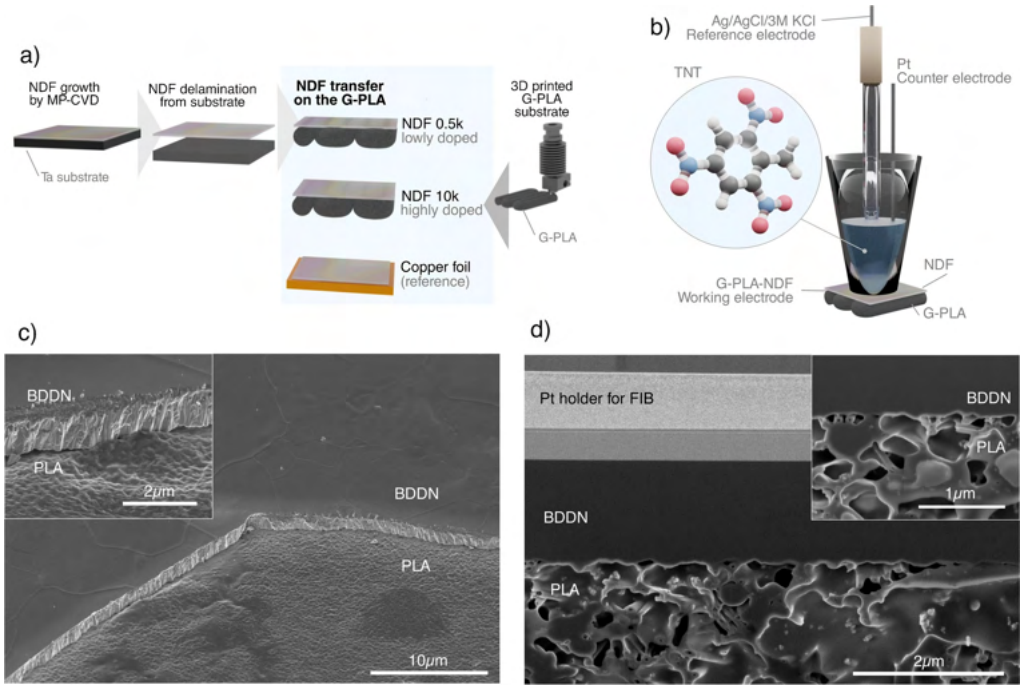

Fig. 4.11. (a) Schematic illustration of the method used to fabricate diamond-graphene-polylactic acid electrodes (G-PLA-NDF). (b) Overview of the setup used for TNT sensing. (c) SEM micrograph of the electrode structure. (d) Cross-sectional view of the sensor. The images were obtained utilising a scanning electron microscope (Helios NanoLab 600i, FEI, USA) [MR2].

The resistance of graphene-PLA-diamond devices as a function of temperature is presented in Table 4.5. The measurements were performed using a HFS600E-PB4 Linkam system (United Kingdom), employing a sandwich configuration.

Table 4.5. Electrical resistance of diamond-graphene-polylactic acid structures fabricated using diamond films with different boron concentrations during CVD growth.

Temperature	**Resistance (kΩ)**	**Resistance (Ω)**
	G-PLA-NDF-0.5k	**G-PLA-NDF-10k**
-50℃	20.231	511
25℃	6.696	405
100℃	1.684	232

As the diamond films display semiconducting properties, their resistance decreases noticeably with the increasing temperature (Fig. 3.14). It is noteworthy that an increase in the temperature can also improve the adhesion of diamond to the graphene-PLA layer, which has a resistivity of 0.6 Ω cm, resulting in an overall increase in conductivity of the structure.

4.5.1. Trinitrotoluene sensor

The fabricated structure was utilised for 2,4,6-trinitrotoluene detection. The measurements were conducted using a potentiostat-galvanostat (VMP-300, BioLogic, France) and boron-doped diamond films with [B]/[C] = 10,000 ppm as the working electrodes, chosen for their superior conductance (see Table 4.5). The standard three-electrode electrochemical setup, shown in Fig. 4.11(b), was used in 0.1 M phosphate buffer solution with varying concentrations of TNT. The results of detecting 2,4,6-trinitrotoluene using the differential pulse voltammetry technique are presented in Fig. 4.12.

The electrode with the nucleation side in direct contact with the solution showed greater electrocatalytic activity towards TNT determination due to the presence of oxygen functional groups that facilitate adsorption and electrochemical reduction, as noted in [147, 289]. The wide linearity range (0.064–64 ppm) and low limit of detection (87 ppb) enable these electrodes to be used for monitoring explosive compounds in the environment at a relatively low cost and in a short time.

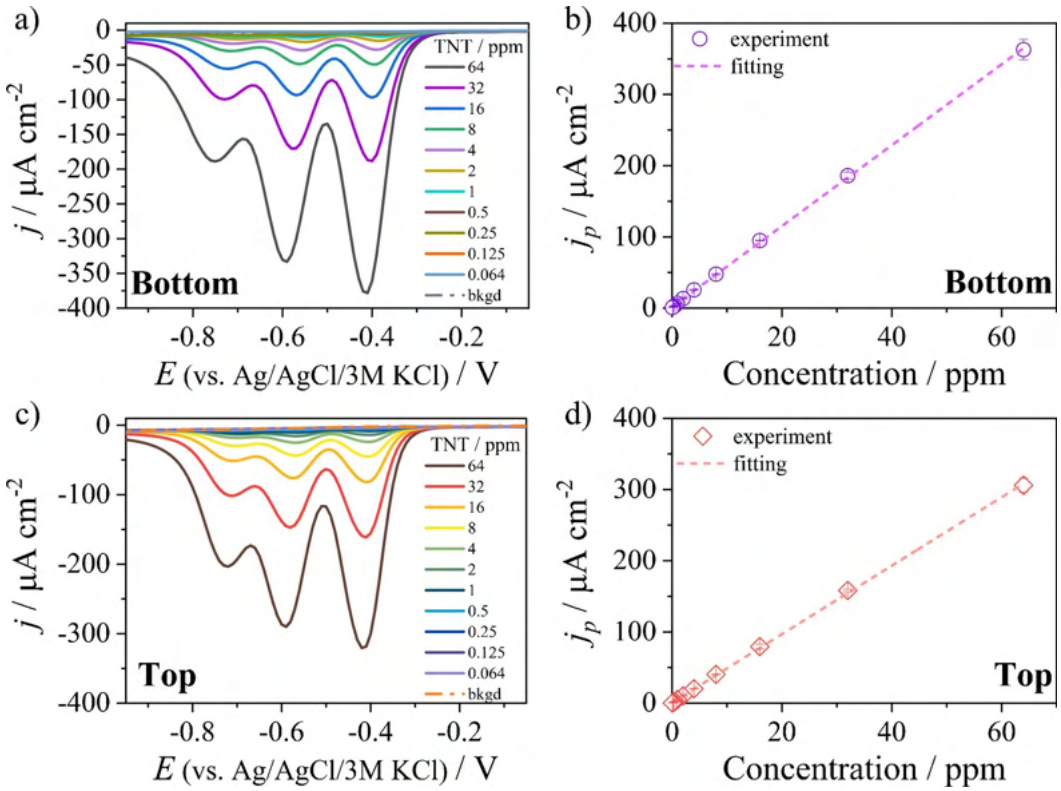

Fig. 4.12. TNT detection using the nucleation (a) and growth side (b) of boron-doped diamond electrode. Calibration curves were generated based on the peak occurring at a potential of approximately -0.4 V vs. Ag|AgCl|3 M KCl for (b) G-PLA-NDF-10 k-bottom and (d) G-PLA-NDF-10 k-top [MR2].

More information about TNT detection, the diamond-graphene-PLA heterojunction, and a comparison with other materials can be found in [MR2].

4.5.2. Electrochemical Double Layer Capacitor

The electrodes described in this study can also be used for fabricating capacitors. A polymer gel with ionic conductivity (PVA/H_2SO_4), which is used for the fabrication of flexible solid-state supercapacitors [290, 291], was sandwiched between two symmetric diamond films with [B]/[C] = 10,000 ppm in the gas phase (on the top surface) on graphene-PLA. The top surface was chosen for the study because of its higher capacitance compared to the nucleation side (section 3.8). The working area was approximately 0.36 cm^2. The measurements were carried out using a potentiostat-galvanostat (VMP-300, BioLogic, France). Cyclic voltammetry studies were conducted at different scan rates, as shown in Fig. 4.13.

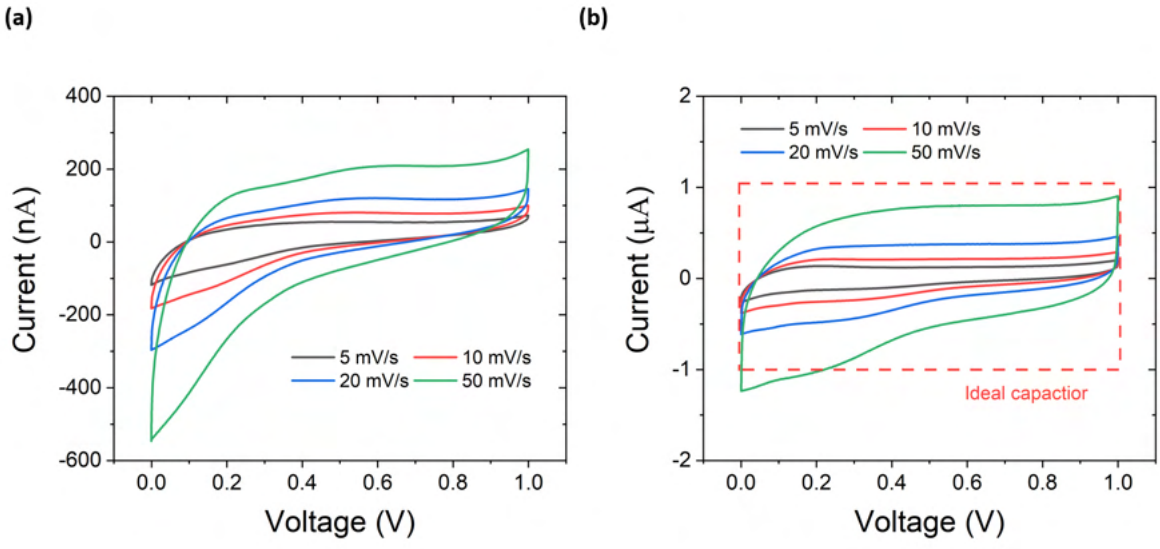

Fig. 4.13. Cyclic voltammetry studies of (a) G-PLA and (b) G-PLA-NDF-10k at different scan rates.

The diamond capacitor has the largest loop area and a more quasi-rectangular shape (Fig. 4.13 (b)), highlighting its superiority over the capacitor with G-PLA alone (Fig. 4.13 (a)). For each scan rate, the capacitor utilising free-standing diamond film exhibits a quasi-rectangular shape (Fig. 4.13 (b)), which is typical for the electrochemical double-layer capacitors [292, 293]. Table 4.6 shows the capacitance values determined for different scan rates using the formula:

$$C = \frac{\int_{V_a}^{V_b} I(V)dV}{2 \cdot A \cdot S_R \cdot \Delta V}, \tag{4.3}$$

where I is the current, A is the surface area, S_R is the scan rate, and ΔV is the voltage range $(V_b - V_a)$.

The capacitance values obtained for the capacitor using diamond films are about 10 times higher compared to the reference sample using two G-PLA electrodes, as a result of different resistances, wettability, and ion diffusion in the fabricated capacitors [294, 295].

Table 4.6. Capacitance of the fabricated devices as a function of the scan rate.

Scan rate (mV/s)	Capacitance (μF/cm^2) G-PLA	Capacitance (μF/cm^2) G-PLA-NDF-10k
50	2.8	36.1
20	3.7	42.2
10	4.7	46.9
5	5.9	51.7

The charging and discharging curves of the capacitor using two G-PLA-NDF-10k electrodes and two G-PLA electrodes (reference sample) are shown in Figs. 4.14 (a) and (b), respectively.

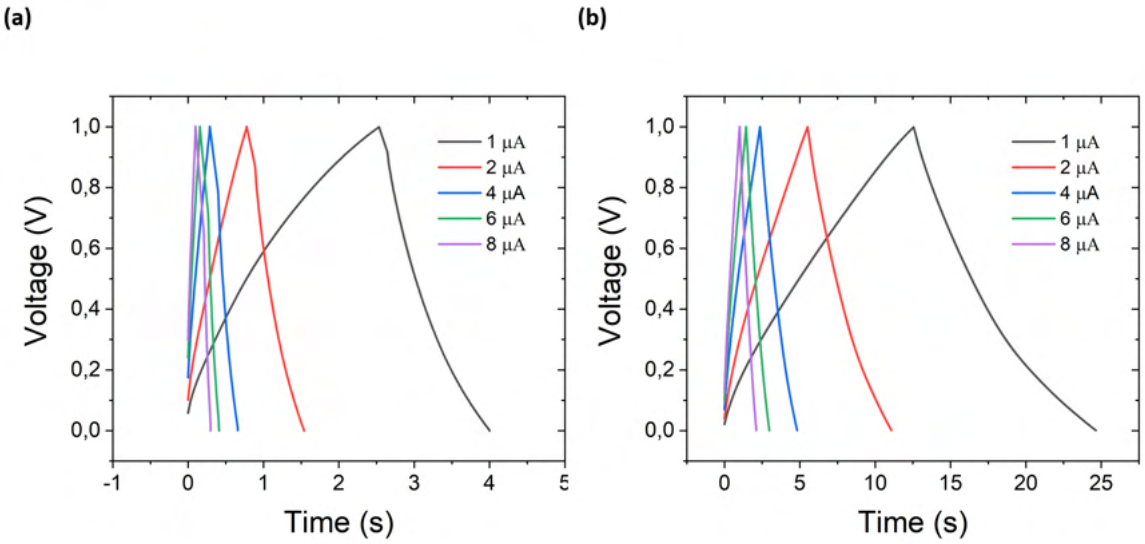

Fig. 4.14. Charging and discharging curves of (a) G-PLA and (b) G-PLA-NDF-10k at different currents.

The charge and discharge curves for G-PLA (Fig. 4.14(a)) and G-PLA-NDF (Fig. 4.14(b)) are both quasi-linear and quasi-symmetrical. The longer charging and discharging times of the capacitor using diamond films confirm its higher capacitance, as capacitance is inversely proportional to the voltage slope. These capacitance values are calculated using the equation:

$$C = \frac{I}{A\frac{dV}{dt}}, \tag{4.4}$$

where I is the discharging current and $\frac{dV}{dt}$ is the slope of the discharging curve. Both are shown in Table 4.7.

Table 4.7. Discharging capacitance of G-PLA and G-PLA-NDF-10k at different currents.

Discharging current (μA)	Capacitance (μF/cm^2) G-PLA	Capacitance (μF/cm^2) G-PLA-NDF-10k
1	12.2	33.7
2	11.2	30.7
4	9.8	27.6
6	9.5	25.8
8	9.2	24.7

The investigation of the discharging curves confirmed that the capacitance of the capacitor utilising G-PLA-NDF-10k is higher compared to the capacitor using bare electrodes. Increasing the discharging current from 1 μA to 8 μA results in a decrease in capacitance of approximately 25% for both types of capacitors. This phenomenon arises due to the limited ion diffusion at higher currents [296]. The cyclic stability of the fabricated capacitors is presented in Fig. 4.15.

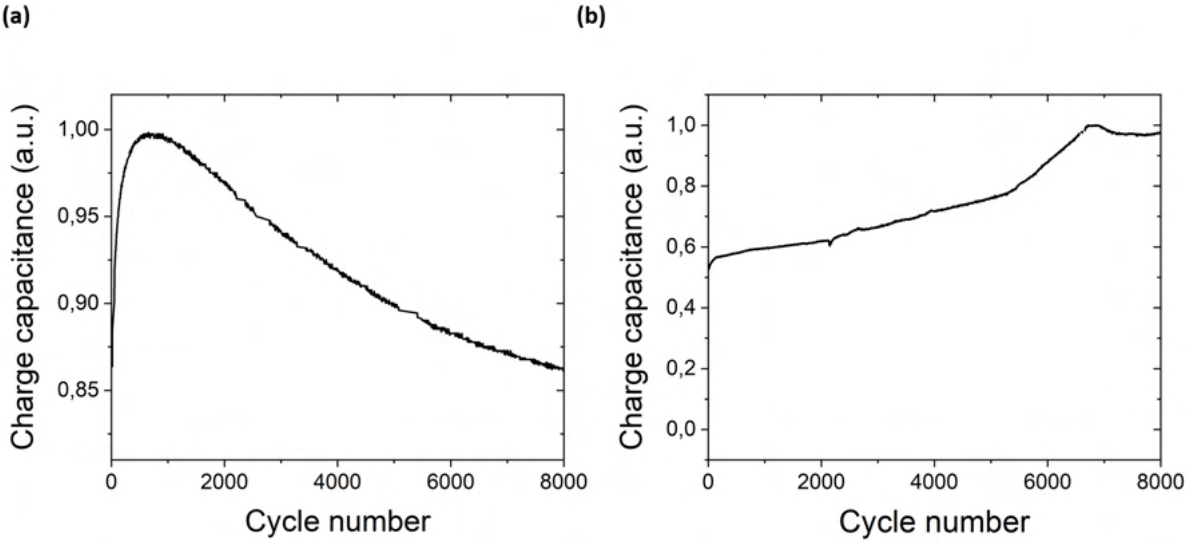

Fig. 4.15. Cyclic stability of (a) G-PLA and (b) G-PLA-NDF-10k capacitors. The capacitance values were calculated based on the charging curves.

After 8,000 cycles, the capacitor using only G-PLA stopped working. For the same number of cycles, the diamond capacitor stabilised. The increase in capacitance over time can be attributed to the absorption of charges [297, 298]. When an electric field is applied, mobile charge carriers move through the material, generating a space charge that causes the formation of macroscopic dipoles. These charge carriers have the potential to get trapped either in the material or at interfaces [299]. As a result, this effect can lead to an increase in capacitance. Another possible explanation is oxidation of the diamond surface, which leads to increased double-layer capacitance [300]. However, further research is needed to fully understand the presented phenomena.

The increase in capacitance of the electrodes with diamond film is more pronounced compared to bare electrodes than to activated electrodes when polar protic solvents are used [286].

Similarly, this increase is more pronounced when the electrodes are functionalised with two-dimensional materials such as MXene [301], while the total capacitance of the manufactured electrodes is lower than that of other carbon materials [292].

To summarise, free-standing boron-doped diamond films were employed to activate 3D-printed electrodes. These activated electrodes were then used to fabricate a TNT sensor and an electrolytic capacitor. For sensing purposes, a layer in direct contact with tantalum during growth was utilised, as it exhibited a higher oxygen concentration, and a detection limit of 0.383 µM was achieved. On the other hand, the growth side, which had higher capacitance, was used to produce the capacitor, with a more than twofold increase in capacitance observed for different the discretisation currents.

4.6. Diamond-Black Phosphorus heterostructures

Phosphorus monolayer is a two-dimensional material whose theoretical mobility is $3 \cdot 10^5 cm^2/(Vs)$ [302]. However, it is not stable under ambient conditions [124] and is often encapsulated using h-BN or graphene [303]. Furthermore, its interaction with diamond has not been fully explored. The goal of this part of the research was to determine the feasibility of integrating free-standing diamond with black phosphorus and to evaluate the possibility of protecting it with diamond films.

To transfer black phosphorus, a modification of the method presented in [128, 186, 187] is used, as shown in Fig. 4.16.

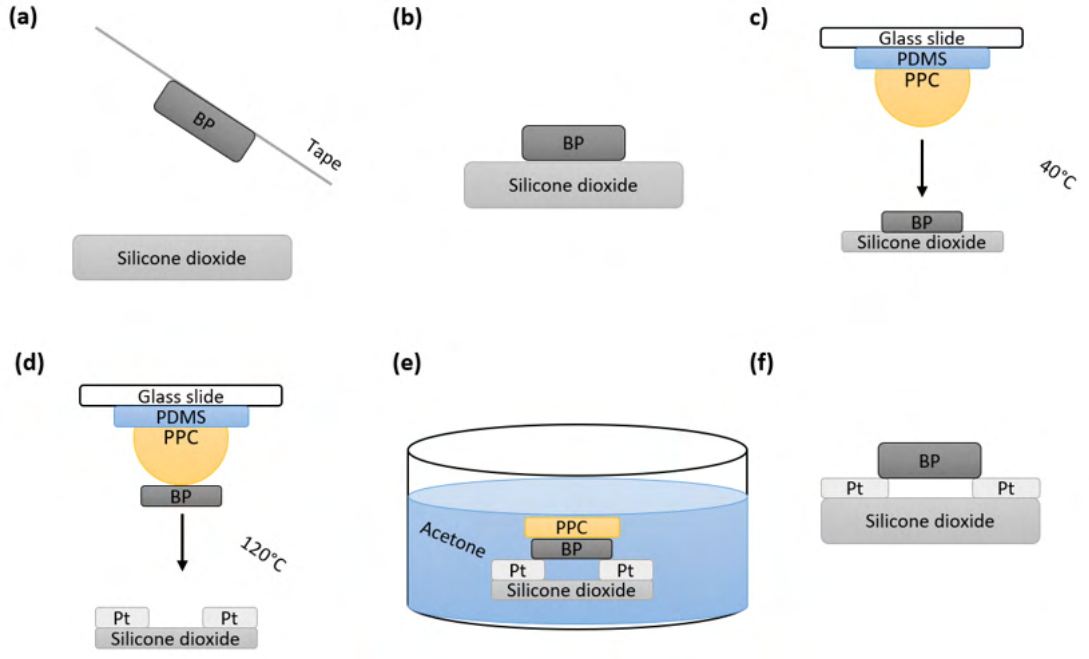

Fig. 4.16. Schematic diagram of the black phosphorus transfer method modified by the author of this dissertation. PPC represents polypropylene carbonate, while BP refers to black phosphorus.

In the first step, a few-layer black phosphorus is exfoliated onto a silicone dioxide substrate using commercially available Scotch tape (Fig. 4.16(a–b)). A polydimethylsiloxane droplet (manufactured using a Sylgard 184 kit with a hardener/base ratio of 1:10) is then deposited onto a flat PDMS surface (PF X-4, Gel-Film, USA) in direct contact with a transparent microscope slide. After 3 hours at 60℃, the hemisphere is coated with a thin layer of polycarbonate (5% in anisole). Next, the black phosphorus is transferred onto pre-fabricated platinum electrodes from Ossila (Fig. 4.16(c–d)). The channel length is 2 µm, and the width is 1 mm, with source and drain contacts consisting of 5 nm of titanium and 100 nm of platinum. The temperature for the pick-up and drop-down steps was 25℃ and 120℃, respectively. Any remaining polymer residues are removed using acetone (see Fig. 4.16(e)). The silicone dioxide sample containing black phosphorus is then connected to a standard circuit board. To transfer the undoped diamond film, which was grown for 1.5 hours using chemical vapour deposition, to the surface of the black phosphorus, the method outlined in section 3.3 is used. The nucleation side of the CVD-grown diamond film was in direct contact with the BP. An image of the fabricated diamond-on-black-phosphorus field-effect transistor and the output characteristics with and without diamond film are shown in Figs. 4.17 (a) and (b), respectively.

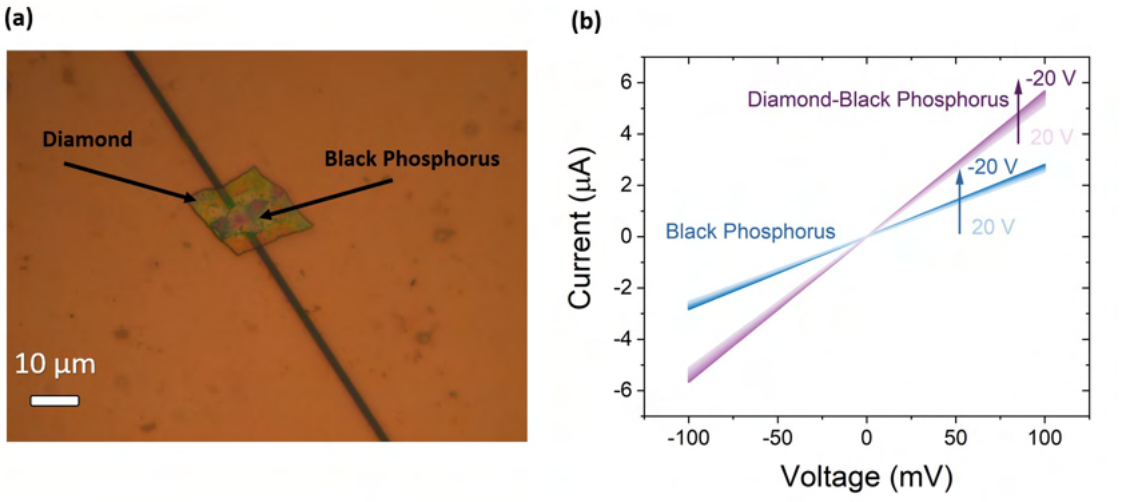

Fig. 4.17. (a) Fabricated diamond-on-black phosphorus back-gated field-effect transistor. (b) Output characteristic of black phosphorus and diamond-on-black phosphorus transistor. Drain current as a function of the drain and gate voltage.

The measurements were performed using a source/measure unit (2604b, Keithley, USA). Initially, measurements were taken for the black phosphorus transistor, and subsequently, measurements were taken again after the diamond was transferred to its surface. FDF improves the adhesion of BP to the pre-fabricated electrodes, increasing the conductivity of the whole device. The realised transistor is normally turned on and exhibits p-type behaviour. The mobility of the carriers in the transistor can be calculated using the equation:

$$\mu = \frac{dI_D}{dV_G} \cdot \frac{L}{WC_{OX}V_D} \tag{4.5}$$

where $\frac{dI_D}{dV_G}$ is the change in the drain current as a function of the gate voltage, L is the length (2 μm) and W is the width (5.5 μm) of the transistor channel, V_D is the drain voltage (0.1 V), and C_{OX} is the capacitance of the gate dielectric (12 nF). The calculated mobility is approximately 3 cm^2/(Vs) and is lower than both the theoretical and experimentally obtained values [90, 302]. This is due to the following factors:

- Exfoliation was performed outside the glove box, exposing the black phosphorus sample to ambient conditions and oxidation.
- The sample was heated to 120℃, first to perform the drop-down of BP, and then the diamond film, which may have further increased the oxidation of the structure.

It should be noted that modifying the transfer procedure is possible. First, the FDF would have to be picked up, followed by the black phosphorus. Then, the transfer would require only a single heating step to 120℃.

The resistance of black-phosphorus and diamond-on-black phosphorus over time is presented in Fig. 4.18. Based on the measurements taken, two characteristic stages can be identified in the behaviour of the systems. During the first stage, there is an increase in conductivity due to the surface O_2 doping effect caused by chemical reactions [304, 305]. In addition, the threshold voltage shifts towards the positive direction [124]. In the subsequent stage, an oxide passivation layer is formed on the surface, which compensates for the effective volume of the BP [124]. This results in an increase in the device's resistance. The decrease in conductivity can also be attributed to covalent modification or transformation of the BP [306]. The diamond-on-black phosphorus device exhibits an increase in resistance at a significantly longer time scale compared to the black phosphorus alone. This suggests that the free-standing diamond provides a longer protection time against ambient conditions for the layered structure.

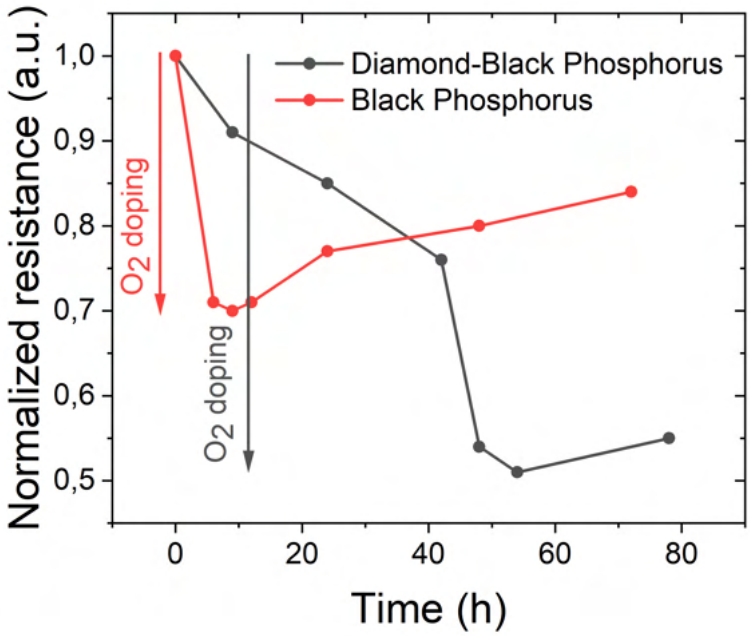

Fig. 4.18. Resistance of the black phosphorus and diamond-on-black phosphorus device measured as a function of time.

In conclusion, the study demonstrates the successful integration of diamond films and black phosphorus in the form of a transistor. The transfer of diamond onto the black phosphorus surface results in increased conductivity due to enhanced adhesion of the film to pre-fabricated electrodes. The introduction of stresses during the transfer process may also contribute to a reduction in resistance, but this requires further investigation. The study reveals that diamond film provides longer protection to layers against ambient conditions, approximately five times longer than black phosphorus alone. Although the protection time is shorter when compared to h-BN and graphene encapsulation [307, 308], it should be possible to use highly boron-doped diamond instead of undoped diamond to achieve superconducting junctions utilising BP in the future.

4.7. Conclusions

In order to investigate and analyze the interaction between free-standing diamond films and polymers and materials that are not heat-resistant, the following six diamond-based heterostructures were fabricated: Diamond-C:H:N:O, Diamond-PDMS, Diamond-Kapton, Diamond-Graphene, Diamond-Graphene-Polylactic acid, and Diamond-Black Phosphorus. The heterostructures were fabricated using various methods and have potential applications as sensors, and micro- and nanoelectronic devices.

The presence of C:H:N:O on the diamond surface enhances its durability and reduces its fragility compared to free-standing diamond film alone. The study demonstrated that polymer

deposition creates a transitional zone between the diamond and the C:H:N:O, which exhibits higher hardness than nylon but lower hardness than free-standing diamond films.

Transferring diamond films onto PDMS, which unlike C:H:N:O does not require magnetron sputtering, may enable simultaneous optical and electrochemical detection of organic compounds in the future. Shaping their optical and electrical parameters can be achieved by boron doping. The obtained results are in agreement with the studies conducted by Ficek et al. [54] on boron-doped diamond films on fused silica, which showed that an increase in the boron and methane concentration leads to a decrease in the films' transmittance. The absorbance values of free-standing boron-doped diamond films are even lower than those previously reported by Stotter et al. [263].

Transferring diamond onto PDMS or directly onto Kapton tape enables the creation of flexible strain sensors. **The electrical resistance of boron-doped free-standing diamond films can be modified by applying stress that modifies inter-grain charge transfer mechanisms, confirming the H2 hypothesis of this thesis**. The realised sensor was able to detect up to 0.55% strain with a gauge factor higher than the Graphene-PDMS device or the PDMS-Black Phosphorus-Paper device [270, 274]. However, this value may increase by changing the level of doping.

Producing gold contacts on PDMS and transferring free-standing diamond film onto them makes it possible to fabricate diamond-graphene junctions. **By modifying the work function of diamond, it is possible to obtain an almost Ohmic contact response or Schottky junctions, confirming the H3 hypothesis.** As a result, it is possible to shape the I-V characteristics of junctions in electronic devices and circuits using differently boron-doped diamonds. Furthermore, the conductivity of the junctions can be controlled through diamond surface termination.

Transferring the free-standing diamond films onto 3D-printed electrodes instead of PDMS activates their surfaces. The top surface of the diamond films on the printed electrodes allows for the fabrication of capacitors, while utilising the nucleation side with low surface roughness and minimal structural defects facilitates efficient electron transfer for sensing nitro compounds. **This confirms the H4 hypothesis of the dissertation.** The obtained limit of detection for TNT is lower than the requirement of the United States Environmental Protection Agency for freshwater screening [309]. The capacitance of the fabricated capacitors is higher than that of bare electrodes but lower than capacitors based on laser-induced graphene on polyimide [292]. However, the total capacitance of the fabricated capacitor can be tuned by adjusting the boron-doping levels, which can modify the surface capacitance and roughness of the free-standing diamond films.

The use of PDMS and PPC to place diamond films onto black phosphorus protects the film for five times longer against ambient conditions than the bare film. Although the protection time is

shorter than using h-BN and graphene encapsulation [307,308], this is because the exfoliation was performed outside the glove box and the sample was heated twice to 120℃ to perform drop-down of the BP, and then the diamond film. Furthermore, using highly doped diamond instead of undoped diamond may make it possible to produce superconducting junctions utilising BP in the future.

5. CONCLUSIONS AND OUTLOOK

Diamond is a promising material for 21st century electronics due to its high electrical and thermal conductivity, possibility of doping, biocompatibility, and high wear resistance. However, the semiconductor properties of free-standing and thin diamond films have not been fully revealed, along with their integration with polymers and non-heat-resistant materials. Based on this, the aim of the dissertation was to fabricate heterostructures containing diamond films on flexible surfaces for application in electronic devices using the change of electrical parameters under the influence of external factors (e.g. pressure, temperature, an stress). The specific goal was to fabricate heterostructures for sensing applications at low temperatures. To overcome this scientific challenge, boron-doped diamonds were grown using chemical vapour deposition on tantalum substrates. The process parameters, such as time and boron/methane concentration in the gas phase, were varied. Due to a mismatch in the thermal expansion coefficient, the diamond films delaminated from the tantalum surfaces. The resulting free-standing diamond films, before being utilised in the fabrication of heterostructures, were analysed using various techniques such as Raman spectroscopy, scanning electron microscopy, atomic force microscopy, nanoindentation tests, and electrical and electrochemical measurements. The most effective free-standing diamond films were used to fabricate electronic devices, utilising two transfer methods designed by the author. The first method was suitable for transferring larger diamond films, while the second method was more appropriate for transferring micrometre-sized devices.

The first fabricated heterostructure was Diamond-C:H:N:O, which is used as a durable electrode. The C:H:N:O layer on the diamond surface reduces its fragility compared to free-standing diamond film alone. A transitional zone occurred between the C:H:N:O layer and the diamond, which exhibits higher hardness than C:H:N:O but lower hardness than free-standing diamond film. Deposition of a nylon-like layer on the growth surface of the diamond, which has higher roughness than the nucleation side, causes cracks to form on the polymer surface. They can be reduced through boron doping, which causes the formation of smaller crystal sizes.

Another realised heterostructure was Diamond-PDMS. Unlike C:H:N:O, it does not require magnetron sputtering. By increasing the boron concentration during CVD growth, it is possible to obtain smaller optical bandgap values. However, this causes a decrease in the transmittance of the free-standing diamond film and, consequently, the entire heterostructure. The increase in absorbance is also correlated with a decrease in resistivity. The obtained surface resistivity ranged from 1605 to 0.38 Ω cm for [B]/[C] = 250 ppm and 20,000 ppm, respectively. The highest mobility was 421 $cm^2\ V^{-1}\ s^{-1}$ for the lowest doped film. As a result, fabricated transparent electrodes can

be used for simultaneous optical and electrochemical detection of organic compounds in the future. Moreover, electrical measurements as a function of temperature showed that all the fabricated diamond films (except the samples with [B]/[C] = 20,000 ppm, which are characterised by metallic conductivity) exhibit two conductivity mechanisms: thermal activation from the valence band to the impurity band at high temperatures and variable range hopping at lower temperatures. **The findings for the most heavily boron-doped diamond films confirm the H1 hypothesis.**

The transfer of free-standing diamond films using PDMS and Kapton provides the choice of the side of the free-standing diamond film (growth or nucleation surface) and also makes it possible to produce Diamond-Kapton heterostructures, which can be used as flexible strain sensors. **Modifying the electrical resistance is possible by changing the inter-grain charge transfer mechanism, confirming the H2 hypothesis.** The realised device is able to detect up to 0.55% strain with a maximum gauge factor of 66.74. It is still possible to increase this by obtaining a higher boron concentration in the diamond lattice through the use of higher methane concentrations during growth, as shown in section 3.6. This consequently leads to an increase in device conductivity and gauge factor.

The integration of PDMS, graphene, and free-standing diamond films makes it possible to obtain almost Ohmic and Schottky junctions, which confirms the H3 hypothesis of this thesis. To achieve this, free-standing diamond films with various boron concentrations, confirmed by Mott-Schottky and Raman studies, were transferred onto prefabricated gold electrodes and then onto graphene. The graphene-diamond device with a film of [B]/[C] = 20,000 ppm in the gas phase, whose dependence on resistance is virtually constant in the range of 153–473 K, exhibits an almost Ohmic response, while the device with [B]/[C] = 500 ppm resembles a Schottky junction.

Transferring the free-standing diamond films onto 3D-printed electrodes (Graphene-Polylactic acid) instead of PDMS allows for the fabrication of electrochemical double layer capacitors and the detection of nitro compounds. In this case, it is necessary to choose the side of the free-standing diamond film that has direct contact with the electrolyte/printed electrode. Electrochemical studies have shown that the growth surface has a higher capacitance than the nucleation side and exhibits higher conductance and Faraday process kinetics. Moreover, it contains more boron atoms, which is attributed to a lower boron incorporation caused by residual oxygen in the chamber during the initial stage of CVD growth. As a result, the growth surface was utilised for the fabrication of the electrochemical double-layer capacitor. The capacitance values of the fabricated device are higher than those utilising bare electrodes. **Furthermore, the nucleation side with low surface roughness was used to detect TNT, which confirms the H4 hypothesis.** The obtained limit of detection for TNT is higher than the requirements of the U.S. Environmental Protection Agency for

freshwater screening.

Finally, undoped free-standing diamond films were transferred onto black phosphorus field-effect transistor to provide longer protection of the BP against ambient conditions. An increase in transistor resistance occurred after five times longer exposure compared to black phosphorus alone. This experiment opens up new possibilities for integrating black phosphorus with diamond and even for producing superconducting junctions by utilising these two materials.

Further research will concentrate on improving the performance of the demonstrated heterostructures, as well as on deriving heterostructures for new and novel applications. There are plans to implement the Josephson junction in a diamond-graphene-diamond structure. The function of the superconductor can be performed by boron-doped diamond. Graphene should act as the insulating layer. This device could be used to realise quantum bits and, consequently, quantum computers in the future. Finally, machine learning algorithms could be used to develop new process parameters [310].

LIST OF PUBLISHED PAPERS INCLUDED IN THE DISSERTATION

[MR1] **M. Rycewicz**, A. Nosek, D. Shin, M. Ficek, J. Buijnsters, and R. Bogdanowicz, “The effect of boron concentration on the electrical, morphological and optical properties of boron- doped nanocrystalline diamond sheets: Tuning the diamond-on-graphene vertical junction,” Diamond and Related Materials, vol. 128, 2022.

[MR2] A. Dettlaff, **M. Rycewicz**, M. Ficek, A. Wieloszyńska, M. Szala, J. Ryl, and R. Bogdanowicz, “Conductive printable electrodes tuned by boron-doped nanodiamond foil additives for nitroexplosive detection,” Microchimica Acta, vol. 189, no. 8, 2022.

[MR3] **M. Rycewicz**, M. Ficek, K. Gajewski, S. Kunuku, J. Karczewski, T. Gotszalk, I. Wlasny, A. Wysmołek, and R. Bogdanowicz, “Low-strain sensor based on the flexible boron-doped diamond-polymer structures,” Carbon, vol. 173, pp. 832–841, 2021.

[MR4] **M. Rycewicz**, Ł. Macewicz, J. Kratochvil, A. Stanisławska, M. Ficek, M. Sawczak, V. Stranak, M. Szkodo, and R. Bogdanowicz, “Physicochemical and mechanical performance of free- standing boron-doped diamond nanosheets coated with c:h:n:o plasma polymer,” Materials, vol. 13, no. 8, 2020.

[MR5] R. Bogdanowicz, M. Ficek, N. Malinowska, S. Gupta, R. Meek, P. Niedziałkowski, **M. Rycewicz**, M. Sawczak, J. Ryl, and T. Ossowski, “Electrochemical performance of thin free-standing boron-doped diamond nanosheet electrodes,” Journal of Electroanalytical Chemistry, vol. 862, 2020.

[MR6] **M. Rycewicz**, A. Nosek, M. Sawczak, J. Ryl, and R. Bogdanowicz, “The electrical, morphological, and optical properties of heavily boron-doped diamond sheets as a function of methane concentration in the gas phase, ”Proceedings of SPIE - The International Society for Optical Engineering," vol. 12200, 2022.

RESEARCH ACTIVITIES AND AWARDS

Internships

02.2021–02.2022: Delft University of Technology, Department of Precision and Microsystems Engineering, Delft, The Netherlands.

Funding: Polish National Agency for Academic Exchange, the Iwanowska Program.

06.2019–07.2019: University of California, Department of Physics and Astronomy, Riverside, USA.

Funding: Polish National Agency for Academic Exchange, PROM Program.

Participation in Research Projects

2022–present: Thermoplastics/ground tire rubber/carbon fillers systems – novel approach for development of low-cost flexible electronics with tailored performance properties (Platinum, DEC No. 1/2021/IDUB/I.1/Pt).

2021–present: Microfluidic cells for high-throughput multiple response analyses (EEA and Norway grants - Applied Research Programme, NOR/POLNOR/UPTURN/0060/2019-00).

2018–2022: 2D phosphorene nanostructures - synthesis and analysis of opto-electrochemical properties towards biosensing systems (SONATA-BIS, UMO-2016/22/E/ST7/00102).

2018–2021: DIAMSEC - ultrasensitive sensing platform for rapid detection of epidemiological and pandemic threats (TECHMATSTRATEG, 1/347324/12/NCBR/2017).

Conferences

2023: Integrated Optics – Sensors, Sensing Structures and Methods 2023, 'Tuning optoelectronic properties of semiconducting diamond sheets for microfluidic devices' (poster).

2022: SPIE Optics + Photonics 2022, 'The electrical, morphological and optical properties of heavily boron-doped diamond sheets as a function of methane concentration in the gas phase' (poster).

2022: Hasselt Diamond Workshop – SBDD XXVI, 'The electrical, morphological and optical properties of nanocrystalline diamond sheets as a function of boron doping: Tuning the graphene-diamond junction' (poster).

2022: Modern Research Techniques for Physicochemical characterization of the Potential Application Systems, 'The effect of boron concentration on the electrical, electrochemical, morphological and optical properties of boron-doped diamond sheets' (oral presentation).

2022: International (Indo – Poland) Workshop on Functional Materials for Sensor and Energy Applications (FM-SEA), 'The effect of boron concentration and strain on the electrical, morphological and optical properties of boron-doped diamond sheets' (invited oral presentation).

2022: Polish Conference on Crystal Growth 2022, 'Effects of boron doping on the electrical, optical and morphological properties of nanocrystalline diamond sheets: Tunning the diamond-on-graphene vertical structure' (oral presentation).

2022: Materials Research Society Fall Meeting.

2020: Interdyscyplinarna Akademicka Konferencja Ochrony Środowiska 2020, 'Wytwarzanie elastycznych i transparentnych elektrod diamentowych służących oczyszczaniu odcieków wodnych' (oral presentation).

2019: Hasselt Diamond Workshop – SBDD XXIV, 'Optimization of the conductivity of diamond nanosheets transferred to a flexible polymer substrate' (poster).

2019: Integrated Optics - Sensors, Sensing Structures and Methods 2019, 'Tuning optical properties of fluorescent nanodiamonds: influence of solvent polarity and pH' (poster).

2018: Saratov Fall Meeting 2018, 'An electrochemical nano-scale boron-doped diamond surface biosensor for influenza virus detection' (poster).

2018: 5th International Conference on Nanotechnology in Medicine (Nanomed-2018), 'Influenza determination by means of electrochemical impedance studies at nanocrystalline boron-doped diamond electrodes' (poster).

2018: NANOSMAT 2018 (Member of the Organizing Committee).

2018: Opto2018 (Member of the Organizing Committee).

Awards

2022: Scholarship to attend the conference 'SPIE Optics + Photonics', under the POWER program.

2022: Best oral presentation during 'Modern Research Techniques for Physicochemical characterization of the Potential Application Systems'.

2020: Scholarship to attend the research project at Delft University of Technology, under the Iwanowska program.

2020: 2nd oral presentation during 'Interdyscyplinarna Akademicka Konferencja Ochrony Środowiska'.

2019: Scholarship to attend the research project at University of California, Riverside under the POWER program (NAWA).

2018: Student Travel Grant (NANOMED 2018 conference).

Published papers

[1] **M. Rycewicz**, A. Nosek, D. Shin, M. Ficek, J. Buijnsters, and R. Bogdanowicz, "The effect of boron concentration on the electrical, morphological and optical properties of boron-doped nanocrystalline diamond sheets: Tuning the diamond-on-graphene vertical junction," Diamond and Related Materials, vol. 128, 2022.

[2] **M. Rycewicz**, A. Nosek, M. Sawczak, J. Ryl, and R. Bogdanowicz, "The electrical, morphological, and optical properties of heavily boron-doped diamond sheets as a function of methane concentration in the gas phase, "Proceedings of SPIE - The International Society for Optical Engineering, vol. 12200, 2022.

[3] A. Dettlaff, **M. Rycewicz**, M. Ficek, A. Wieloszyńska, M. Szala, J. Ryl, and R. Bogdanowicz, "Conductive printable electrodes tuned by boron-doped nanodiamond foil additives for nitroexplosive detection," Microchimica Acta, vol. 189, no. 8, 2022.

[4] W. Białobrzeska, M. Ficek, B. Dec, S. Osella, B. Trzaskowski, A. Jaramillo-Botero, M. Pierpaoli, **M. Rycewicz**, Y. Dashkevich, T. Łęga, N. Malinowska, Z. Cebula, D. Bigus, D. Firganek, E. Bięga, K. Dziąbowska, M. Brodowski, M. Kowalski, M. Panasiuk, B. Gromadzka, S. Żołędowska, D. Nidzworski, K. Pyrć, W. Goddard, and R. Bogdanowicz, "Performance of electrochemical immunoassays for clinical diagnostics of sars-cov-2 based on selective nucleocapsid n protein detection: Boron-doped diamond, gold and glassy carbon evaluation," Biosensors and Bioelectronics, vol. 209, 2022.

[5] M. Kosowska, A. Mallik, **M. Rycewicz**, K. Haenen, and M. Szczerska, "Diamond structures for tuning of the finesse coefficient of photonic devices," Materials, vol. 15, no. 7, 2022.

[6] M. Szczerska, M. Kosowska, P. Listewnik, **M. Rycewicz**, M. Bechelany, Y. Fleger, D. Fixler, and P. Jakóbczyk, "Diamond protection for reusable zno coated fiber-optic measurement head in optoelectrochemical investigation of bisphenol a," Measurement: Journal of the International Measurement Confederation, vol. 189, 2022.

[7] M. Kosowska, P. Jakóbczyk, M. Rycewicz, A. Vitkin, and M. Szczerska, “Low-coherence photonic method of electrochemical processes monitoring,” Scientific Reports, vol. 11, no. 1, 2021.

[8] M. Pierpaoli, C. Giosuè, N. Czerwińska, **M. Rycewicz**, A. Wieloszyńska, R. Bogdanowicz, and M. Ruello, “Characterization and filtration efficiency of sustainable pla fibers obtained via a hybrid 3d-printed/electrospinning technique,” Materials, vol. 14, no. 22, 2021.

[9] **M. Rycewicz**, M. Ficek, K. Gajewski, S. Kunuku, J. Karczewski, T. Gotszalk, I. Wlasny, A. Wysmołek, and R. Bogdanowicz, “Low-strain sensor based on the flexible boron-doped diamond-polymer structures,” Carbon, vol. 173, pp. 832–841, 2021.

[10] M. Kosowska, P. Listewnik, D. Majchrowicz, **M. Rycewicz**, M. Bechelany, Y. Fleger, M. Chen, D. Fixler, K. Dholakia, and M. Szczerska, “Microscale diamond protection for a zno coated fiber optic sensor,” Scientific Reports, vol. 10, no. 1, 2020.

[11] **M. Rycewicz**, L. Macewicz, J. Kratochvil, A. Stanisławska, M. Ficek, M. Sawczak, V. Stranak, M. Szkodo, and R. Bogdanowicz, “Physicochemical and mechanical performance of free-standing boron-doped diamond nanosheets coated with c:h:n:o plasma polymer,” Materials, vol. 13, no. 8, 2020.

[12] R. Bogdanowicz, M. Ficek, N. Malinowska, S. Gupta, R. Meek, P. Niedziałkowski, **M. Rycewicz**, M. Sawczak, J. Ryl, and T. Ossowski, “Electrochemical performance of thin free-standing boron-doped diamond nanosheet electrodes,” Journal of Electroanalytical Chemistry, vol. 862, 2020.

[13] M. Pierpaoli, A. Lewkowicz, **M. Rycewicz**, K. Szczodrowski, M. Ruello, and R. Bogdanowicz, “Enhanced photocatalytic activity of transparent carbon nanowall/tio2 heterostructures,” Materials Letters, vol. 262, 2020.

[14] M. Pierpaoli, **M. Rycewicz**, A. Łuczkiewicz, S. Fudala-Książek, R. Bogdanowicz, and M. Ruello, “Electrodes criticality: The impact of crms in the leachate electrochemical oxidation,” Manufacturing Review, vol. 7, 2020.

[15] M. Pierpaoli, M. Ficek, **M. Rycewicz**, M. Sawczak, J. Karczewski, M. Ruello, and R. Bogdanowicz, “Tailoring electro/optical properties of transparent boron-doped carbon nanowalls grown on quartz,” Materials, vol. 12, no. 3, 2019.

[16] B. Dec, M. Ficek, **M. Rycewicz**, Macewicz, M. Gnyba, M. Sawczak, M. Sobaszek, and R. Bogdanowicz, “Gas composition influence on the properties of boron-doped diamond films deposited on the fused silica,” Materials Science- Poland, vol. 36, no. 2, pp. 288–296, 2018.

ACKNOWLEDGMENTS

Joshua Tree National Park, 2022.

I am incredibly grateful to my thesis advisor, Prof. Robert Bogdanowicz, for his guidance and unwavering encouragement.

I also want to express my appreciation to Prof. Josephus (Ivan) Buijnsters, Prof. Marc Bockrath, and my friends and colleagues, who have given me so much inspiration and help throughout my journey.

Without a doubt, I want to end by thanking my family for their unending love and unwavering assistance.

BIBLIOGRAPHY

[1] G. Cicala, V. Magaletti, G. Carbone, and G. S. Senesi, "Load sensitive super-hardness of nanocrystalline diamond coatings," *Diamond and Related Materials*, vol. 101, p. 107653, 2020.

[2] A. Erdemir and J. M. Martin, "Superior wear resistance of diamond and dlc coatings," *Current Opinion in Solid State and Materials Science*, vol. 22, no. 6, pp. 243–254, 2018.

[3] J. Graebner, S. Jin, G. Kammlott, J. Herb, and C. Gardinier, "Unusually high thermal conductivity in diamond films," *Applied physics letters*, vol. 60, no. 13, pp. 1576–1578, 1992.

[4] H. Kozak, Z. Remes, J. Houdkova, S. Stehlik, A. Kromka, and B. Rezek, "Chemical modifications and stability of diamond nanoparticles resolved by infrared spectroscopy and kelvin force microscopy," *Journal of nanoparticle research*, vol. 15, pp. 1–9, 2013.

[5] U. Choi, T. Kwak, S. Han, S.-W. Kim, and O. Nam, "High breakdown voltage of boron-doped diamond metal semiconductor field effect transistor grown on freestanding heteroepitaxial diamond substrate," *Diamond and Related Materials*, vol. 121, p. 108782, 2022.

[6] R. Kalish, "Doping of diamond," *Carbon*, vol. 37, no. 5, pp. 781–785, 1999.

[7] P. W. May, "Cvd diamond: a new technology for the future?" *Endeavour*, vol. 19, no. 3, pp. 101–106, 1995.

[8] D. Duan, G. Du, V. K. Kavatamane, S. Arumugam, Y.-K. Tzeng, H.-C. Chang, and G. Balasubramanian, "Efficient nitrogen-vacancy centers' fluorescence excitation and collection from micrometer-sized diamond by a tapered optical fiber in endoscope-type configuration," *Optics Express*, vol. 27, no. 5, pp. 6734–6745, 2019.

[9] M. Kosowska, D. Majchrowicz, M. Ficek, P. Wierzba, Y. Fleger, D. Fixler, and M. Szczerska, "Nanocrystalline diamond sheets as protective coatings for fiber-optic measurement head," *Carbon*, vol. 156, pp. 104–109, 2020.

[10] A. M. Jetpurwala and M. Dikshit, "Chemical vapor deposition diamond dental burs for high speed air turbine handpieces," *Surface and Coatings Technology*, vol. 418, p. 127244, 2021.

[11] S. Chauhan, N. Jain, and U. Nagaich, "Nanodiamonds with powerful ability for drug delivery and biomedical applications: Recent updates on in vivo study and patents," *Journal of pharmaceutical analysis*, vol. 10, no. 1, pp. 1–12, 2020.

[12] M. Liao, “Progress in semiconductor diamond photodetectors and mems sensors,” *Functional Diamond*, vol. 1, no. 1, pp. 29–46, 2022.

[13] J. Zalieckas, P. Pobedinskas, M. M. Greve, K. Eikehaug, K. Haenen, and B. Holst, “Large area microwave plasma cvd of diamond using composite right/left-handed materials,” *Diamond and Related Materials*, vol. 116, p. 108394, 2021.

[14] A. Bolshakov, V. Ralchenko, V. Yurov, G. Shu, E. Bushuev, A. Khomich, E. Ashkinazi, D. Sovyk, I. Antonova, S. Savin *et al.*, “Enhanced deposition rate of polycrystalline cvd diamond at high microwave power densities,” *Diamond and Related Materials*, vol. 97, p. 107466, 2019.

[15] X. Song, H. Wang, X. Wang, and F. Sun, “Fabrication and evaluation of diamond thick film-si3n4 brazed cutting tool by microwave plasma chemical vapor deposition method,” *Journal of Materials Processing Technology*, vol. 291, p. 117034, 2021.

[16] A. Kromka, O. Babchenko, T. Izak, K. Hruska, and B. Rezek, “Linear antenna microwave plasma cvd deposition of diamond films over large areas,” *Vacuum*, vol. 86, no. 6, pp. 776–779, 2012.

[17] J. Butler, Y. A. Mankelevich, A. Cheesman, J. Ma, and M. Ashfold, “Understanding the chemical vapor deposition of diamond: recent progress,” *Journal of Physics: Condensed Matter*, vol. 21, no. 36, p. 364201, 2009.

[18] J. Asmussen and D. Reinhard, *Diamond films handbook*. CRC Press, 2002.

[19] O. A. Williams and M. Nesládek, “Growth and properties of nanocrystalline diamond films,” *physica status solidi (a)*, vol. 203, no. 13, pp. 3375–3386, 2006.

[20] E. Six. The element six cvd diamond handbook. [Online]. Available: https://e6cvd.com/media/wysiwyg/pdf/E6_CVD_Diamond_Handbook_A5_v10X.pdf

[21] P. Strobel, M. Riedel, J. Ristein, and L. Ley, “Surface transfer doping of diamond,” *Nature*, vol. 430, no. 6998, pp. 439–441, 2004.

[22] F. Maier, M. Riedel, B. Mantel, J. Ristein, and L. Ley, “Origin of surface conductivity in diamond,” *Physical review letters*, vol. 85, no. 16, p. 3472, 2000.

[23] S. A. Russell, S. Sharabi, A. Tallaire, and D. A. Moran, “Hydrogen-terminated diamond field-effect transistors with cutoff frequency of 53 ghz,” *IEEE Electron Device Letters*, vol. 33, no. 10, pp. 1471–1473, 2012.

[24] Y. Li, J.-F. Zhang, G.-P. Liu, Z.-Y. Ren, J.-C. Zhang, and Y. Hao, “Mobility of two-dimensional hole gas in h-terminated diamond,” *physica status solidi (RRL)–Rapid Research Letters*, vol. 12, no. 3, p. 1700401, 2018.

[25] N. I. Polushin, A. I. Laptev, B. V. Spitsyn, A. E. Alexenko, A. M. Polyansky, A. L. Maslov, and T. V. Martynova, "Deposition of boron-doped thin cvd diamond films from methane-triethyl borate-hydrogen gas mixture," *Processes*, vol. 8, no. 6, p. 666, 2020.

[26] S. B. van Dam, M. Walsh, M. J. Degen, E. Bersin, S. L. Mouradian, A. Galiullin, M. Ruf, M. IJspeert, T. H. Taminiau, R. Hanson *et al.*, "Optical coherence of diamond nitrogen-vacancy centers formed by ion implantation and annealing," *Physical Review B*, vol. 99, no. 16, p. 161203, 2019.

[27] H. Umezawa, "Recent advances in diamond power semiconductor devices," *Materials Science in Semiconductor Processing*, vol. 78, pp. 147–156, 2018.

[28] S. Koizumi, H. Umezawa, J. Pernot, and M. Suzuki, *Power electronics device applications of diamond semiconductors*. Woodhead publishing, 2018.

[29] J. Tasselli, L. Fontaine, K. Isoird, and P. Austin, "Ohmic contacts by phosphorous ion implantation on (111) n-type cvd diamond," in *31st International Conference on Diamond and Carbon Materials*, 2021.

[30] T. Matsumoto, T. Mukose, T. Makino, D. Takeuchi, S. Yamasaki, T. Inokuma, and N. Tokuda, "Diamond schottky-pn diode using lightly nitrogen-doped layer," *Diamond and Related Materials*, vol. 75, pp. 152–154, 2017.

[31] Z. M. Shah and A. Mainwood, "A theoretical study of the effect of nitrogen, boron and phosphorus impurities on the growth and morphology of diamond surfaces," *Diamond and related materials*, vol. 17, no. 7-10, pp. 1307–1310, 2008.

[32] M. Hasegawa, D. Takeuchi, S. Yamanaka, M. Ogura, H. Watanabe, N. Kobayashi, H. Okushi, and K. Kajimura, "N-type control by sulfur ion implantation in homoepitaxial diamond films grown by chemical vapor deposition," *Japanese Journal of Applied Physics*, vol. 38, no. 12B, p. L1519, 1999.

[33] J. F. Prins, "N-type semiconducting diamond by means of oxygen-ion implantation," *Physical review B*, vol. 61, no. 11, p. 7191, 2000.

[34] D. Liu, L. Hao, Y. Teng, F. Qin, Y. Shen, K. Tang, J. Ye, S. Zhu, R. Zhang, Y. Zheng *et al.*, "Nitrogen modulation of boron doping behavior for accessible n-type diamond," *APL Materials*, vol. 9, no. 8, p. 081106, 2021.

[35] V. Mortet, Z. V. Živcová, A. Taylor, O. Frank, P. Hubík, D. Trémouilles, F. Jomard, J. Barjon, and L. Kavan, "Insight into boron-doped diamond raman spectra characteristic features," *Carbon*, vol. 115, pp. 279–284, 2017.

[36] H. Kato, D. Takeuchi, N. Tokuda, H. Umezawa, H. Okushi, and S. Yamasaki, "Characterization of specific contact resistance on heavily phosphorus-doped diamond films," *Diamond and Related Materials*, vol. 18, no. 5-8, pp. 782–785, 2009.

[37] J.-P. Lagrange, A. Deneuville, and E. Gheeraert, "Activation energy in low compensated homoepitaxial boron-doped diamond films," *Diamond and Related Materials*, vol. 7, no. 9, pp. 1390–1393, 1998.

[38] W. Gajewski, P. Achatz, O. A. Williams, K. Haenen, E. Bustarret, M. Stutzmann, and J. A. Garrido, "Electronic and optical properties of boron-doped nanocrystalline diamond films," *Physical Review B*, vol. 79, no. 4, p. 045206, 2009.

[39] M. Ullah, E. Ahmed, F. Hussain, A. M. Rana, and R. Raza, "Electrical conductivity enhancement by boron-doping in diamond using first principle calculations," *Applied Surface Science*, vol. 334, pp. 40–44, 2015.

[40] E. Ekimov, V. Sidorov, E. Bauer, N. Mel'Nik, N. Curro, J. Thompson, and S. Stishov, "Superconductivity in diamond," *nature*, vol. 428, no. 6982, pp. 542–545, 2004.

[41] T. Yokoya, T. Nakamura, T. Matsushita, T. Muro, Y. Takano, M. Nagao, T. Takenouchi, H. Kawarada, and T. Oguchi, "Origin of the metallic properties of heavily boron-doped superconducting diamond," *Nature*, vol. 438, no. 7068, pp. 647–650, 2005.

[42] V. Mortet, A. Taylor, Z. V. Živcová, D. Machon, O. Frank, P. Hubík, D. Trémouilles, and L. Kavan, "Analysis of heavily boron-doped diamond raman spectrum," *Diamond and Related Materials*, vol. 88, pp. 163–166, 2018.

[43] J. E. Butler, A. Vikharev, A. Gorbachev, M. Lobaev, A. Muchnikov, D. Radischev, V. Isaev, V. Chernov, S. Bogdanov, M. Drozdov *et al.*, "Nanometric diamond delta doping with boron," *physica status solidi (RRL)–Rapid Research Letters*, vol. 11, no. 1, p. 1600329, 2017.

[44] E. Schubert, "Delta doping of iii–v compound semiconductors: Fundamentals and device applications," *Journal of Vacuum Science & Technology A: Vacuum, Surfaces, and Films*, vol. 8, no. 3, pp. 2980–2996, 1990.

[45] A. Denisenko and E. Kohn, "Diamond power devices. concepts and limits," *Diamond and related materials*, vol. 14, no. 3-7, pp. 491–498, 2005.

[46] A. Fiori, J. Pernot, E. Gheeraert, and E. Bustarret, "Simulations of carrier confinement in boron δ-doped diamond devices," *physica status solidi (a)*, vol. 207, no. 9, pp. 2084–2087, 2010.

[47] R. S. Sussmann, *CVD diamond for electronic devices and sensors*. John Wiley & Sons, 2009.

[48] J. A. Cuenca, T. Brien, S. Mandal, S. Manifold, S. Doyle, A. Porch, G. M. Klemencic, and O. A. Williams, "Superconducting boron doped nanocrystalline diamond microwave coplanar resonator," *Carbon*, vol. 201, pp. 251–259, 2023.

[49] G. Klemencic, D. Perkins, J. Fellows, C. Muirhead, R. Smith, S. Mandal, S. Manifold, M. Salman, S. Giblin, and O. Williams, "Phase slips and metastability in granular boron-doped nanocrystalline diamond microbridges," *Carbon*, vol. 175, pp. 43–49, 2021.

[50] C. Liu, X. Song, Q. Li, Y. Ma, and C. Chen, "Superconductivity in compression-shear deformed diamond," *Physical Review Letters*, vol. 124, no. 14, p. 147001, 2020.

[51] Z. Shi, M. Dao, E. Tsymbalov, A. Shapeev, J. Li, and S. Suresh, "Metallization of diamond," *Proceedings of the National Academy of Sciences*, vol. 117, no. 40, pp. 24 634–24 639, 2020.

[52] A. Nie, Y. Bu, P. Li, Y. Zhang, T. Jin, J. Liu, Z. Su, Y. Wang, J. He, Z. Liu *et al.*, "Approaching diamond's theoretical elasticity and strength limits," *Nature communications*, vol. 10, no. 1, p. 5533, 2019.

[53] A. Banerjee, D. Bernoulli, H. Zhang, M.-F. Yuen, J. Liu, J. Dong, F. Ding, J. Lu, M. Dao, W. Zhang *et al.*, "Ultralarge elastic deformation of nanoscale diamond," *Science*, vol. 360, no. 6386, pp. 300–302, 2018.

[54] M. Ficek, M. Sobaszek, M. Gnyba, J. Ryl, M. Smietana, J. Jasiński, P. Caban, R. Bogdanowicz *et al.*, "Optical and electrical properties of boron doped diamond thin conductive films deposited on fused silica glass substrates," *Applied Surface Science*, vol. 387, pp. 846–856, 2016.

[55] S. Janssens, P. Pobedinskas, J. Vacik, V. Petráková, B. Ruttens, J. D'Haen, M. Nesládek, K. Haenen, and P. Wagner, "Separation of intra-and intergranular magnetotransport properties in nanocrystalline diamond films on the metallic side of the metal–insulator transition," *New Journal of Physics*, vol. 13, no. 8, p. 083008, 2011.

[56] X. Jia, N. Huang, Y. Guo, L. Liu, P. Li, Z. Zhai, B. Yang, Z. Yuan, D. Shi, and X. Jiang, "Growth behavior of cvd diamond films with enhanced electron field emission properties over a wide range of experimental parameters," *Journal of Materials Science & Technology*, vol. 34, no. 12, pp. 2398–2406, 2018.

[57] R. Rouzbahani, S. S. Nicley, D. E. Vanpoucke, F. Lloret, P. Pobedinskas, D. Araujo, and K. Haenen, "Impact of methane concentration on surface morphology and boron incorporation of heavily boron-doped single crystal diamond layers," *Carbon*, vol. 172, pp. 463–473, 2021.

[58] T. Klein, P. Achatz, J. Kacmarcik, C. Marcenat, F. Gustafsson, J. Marcus, E. Bustarret, J. Pernot, F. Omnès, B. E. Sernelius *et al.*, "Metal-insulator transition and superconductivity in boron-doped diamond," *Physical Review B*, vol. 75, no. 16, p. 165313, 2007.

[59] E. Bushuev, V. Y. Yurov, A. Bolshakov, V. Ralchenko, A. Khomich, I. Antonova, E. Ashkinazi, V. Shershulin, V. Pashinin, and V. Konov, "Express in situ measurement of epitaxial cvd diamond film growth kinetics," *Diamond and Related Materials*, vol. 72, pp. 61–70.

[60] M. Ficek, S. Drijkoningen, J. Karczewski, R. Bogdanowicz, and K. Haenen, "Low temperature growth of diamond films on optical fibers using linear antenna cvd system," in *IOP Conference Series: Materials Science and Engineering*, vol. 104, no. 1. IOP Publishing, 2016, p. 012025.

[61] K. Hassouni, G. Lombardi, X. Duten, G. Haagelar, F. Silva, A. Gicquel, T. Grotjohn, M. Capitelli, and J. Röpcke, "Overview of the different aspects in modelling moderate pressure h2 and h2/ch4 microwave discharges," *Plasma Sources Science and Technology*, vol. 15, no. 1, p. 117, 2006.

[62] A. Tallaire, J. Achard, O. Brinza, V. Mille, M. Naamoun, F. Silva, and A. Gicquel, "Growth strategy for controlling dislocation densities and crystal morphologies of single crystal diamond by using pyramidal-shape substrates," *Diamond and Related Materials*, vol. 33, pp. 71–77, 2013.

[63] M. Schreck, J. Asmussen, S. Shikata, J.-C. Arnault, and N. Fujimori, "Large-area high-quality single crystal diamond," *Mrs Bulletin*, vol. 39, no. 6, pp. 504–510.

[64] S. Zhao and K. Larsson, "Theoretical study of the energetic stability and geometry of terminated and b-doped diamond (111) surfaces," *The Journal of Physical Chemistry C*, vol. 118, no. 4, pp. 1944–1957, 2014.

[65] S. Chowdhury, "Gan-on-gan power device design and fabrication," in *Wide Bandgap Semiconductor Power Devices*. Elsevier, 2019, pp. 209–248.

[66] M. Bevilacqua, N. Tumilty, C. Mitra, H. Ye, T. Feygelson, J. E. Butler, and R. B. Jackman, "Nanocrystalline diamond as an electronic material: An impedance spectroscopic and hall effect measurement study," *Journal of Applied Physics*, vol. 107, no. 3, p. 033716, 2010.

[67] J. Nakanishi, A. Otsuki, T. Oku, O. Ishiwata, and M. Murakami, “Formation of ohmic contacts to p-type diamond using carbide forming metals,” *Journal of Applied Physics*, vol. 76, no. 4, pp. 2293–2298, 1994.

[68] C. Schreyvogel, V. Polyakov, R. Wunderlich, J. Meijer, and C. Nebel, “Active charge state control of single nv centres in diamond by in-plane al-schottky junctions,” *Scientific reports*, vol. 5, no. 1, pp. 1–12, 2015.

[69] C. Yu, Z. He, C. Zhou, J. Guo, X. Song, S. Cai, and Z. Feng, “High frequency hydrogen-terminated diamond mesfet with an fmax of 103ghz,” *Materials Today Communications*, vol. 28, p. 102489, 2021.

[70] T. Iwasaki, Y. Hoshino, K. Tsuzuki, H. Kato, T. Makino, M. Ogura, D. Takeuchi, H. Okushi, S. Yamasaki, and M. Hatano, “High-temperature operation of diamond junction field-effect transistors with lateral pn junctions,” *IEEE electron device letters*, vol. 34, no. 9, pp. 1175–1177, 2013.

[71] Y.-F. Wang, W. Wang, X. Chang, X. Zhang, J. Fu, Z. Liu, D. Zhao, G. Shao, S. Fan, R. Bu *et al.*, “Hydrogen-terminated diamond field-effect transistor with alox dielectric layer formed by autoxidation,” *Scientific reports*, vol. 9, no. 1, p. 5192, 2019.

[72] C. Masante, J. Pernot, J. Letellier, D. Eon, and N. Rouger, “175v,> 5.4 mv/cm, 50m$\omega\cdot$ cm^2 at 250℃ diamond mosfet and its reverse conduction,” in *2019 31st International Symposium on Power Semiconductor Devices and ICs (ISPSD)*. IEEE, 2019, pp. 151–154.

[73] H. Kato, K. Oyama, T. Makino, M. Ogura, D. Takeuchi, and S. Yamasaki, “Diamond bipolar junction transistor device with phosphorus-doped diamond base layer,” *Diamond and related materials*, vol. 27, pp. 19–22, 2012.

[74] S. J. Cho, D. Liu, A. Hardy, J. Kim, J. Gong, C. J. Herrera-Rodriguez, E. Swinnich, X. Konstantinou, G.-Y. Oh, D. G. Kim *et al.*, “Fabrication of algaas/gaas/diamond heterojunctions for diamond-collector hbts,” *AIP Advances*, vol. 10, no. 12, p. 125226, 2020.

[75] M. Dankerl, S. Eick, B. Hofmann, M. Hauf, S. Ingebrandt, A. Offenhäusser, M. Stutzmann, and J. A. Garrido, “Diamond transistor array for extracellular recording from electrogenic cells,” *Advanced functional materials*, vol. 19, no. 18, pp. 2915–2923, 2009.

[76] N. A. Ahmad, R. A. Rahim, B. Rezek, A. Kromka, N. S. Ismail, S. C. B. Gopinath, T. Izak, V. Procházka, F. N. M. Faudzi, A. S. Z. Abidin *et al.*, “Nanocrystalline diamond electrolyte-gates in field effect transistor for a prolific aptasensing hiv-1 tat on hydrogen-terminated surface.” *International Journal of Nanoelectronics & Materials*, vol. 13, no. 2, 2020.

[77] Q. Zhang, X. Chang, B. Xu, Y. Wang, D. Zhang, Y. Feng, S. He, G. Chen, Q. Li, J. Wang *et al.*, "Detection of glucose using diamond solution-gate field-effect transistor," *IEEE Transactions on Electron Devices*, vol. 69, no. 8, pp. 4534–4539, 2022.

[78] B. Huang, X. Bai, S. K. Lam, and K. K. Tsang, "Diamond finfet without hydrogen termination," *Scientific Reports*, vol. 8, no. 1, p. 3063, 2018.

[79] B. Huang, X. Bai, S. K. Lam, and S. J. Kim, "Diamond lateral finfet with triode-like behavior," *Scientific Reports*, vol. 10, no. 1, p. 2279, 2020.

[80] J. Szmidt, R. Beck, S. Mitura, and A. Sokołowska, "Application of diamond-like layers as gate dielectric in metal/insulator/semiconductor transistor," *Diamond and Related Materials*, vol. 3, no. 4-6, pp. 853–857, 1994.

[81] M. Suzuki, "High voltage diamond pin diodes: feasibility study on ultimate properties of diamond toward ultimate power devices," *Oyo Buturi*, vol. 85, pp. 218–222, 2016.

[82] K. Bray, H. Kato, R. Previdi, R. Sandstrom, K. Ganesan, M. Ogura, T. Makino, S. Yamasaki, A. P. Magyar, M. Toth *et al.*, "Single crystal diamond membranes for nanoelectronics," *Nanoscale*, vol. 10, no. 8, pp. 4028–4035, 2018.

[83] S. Koizumi, K. Watanabe, M. Hasegawa, and H. Kanda, "Ultraviolet emission from a diamond pn junction," *Science*, vol. 292, no. 5523, pp. 1899–1901, 2001.

[84] P. Avouris, T. F. Heinz, and T. Low, *2D Materials*. Cambridge University Press, 2017.

[85] J. Wang, F. Ma, W. Liang, and M. Sun, "Electrical properties and applications of graphene, hexagonal boron nitride (h-bn), and graphene/h-bn heterostructures," *Materials Today Physics*, vol. 2, pp. 6–34, 2017.

[86] C. Yuan, J. Li, L. Lindsay, D. Cherns, J. W. Pomeroy, S. Liu, J. H. Edgar, and M. Kuball, "Modulating the thermal conductivity in hexagonal boron nitride via controlled boron isotope concentration," *Communications physics*, vol. 2, no. 1, p. 43, 2019.

[87] D. Gupta, V. Chauhan, and R. Kumar, "A comprehensive review on synthesis and applications of molybdenum disulfide (mos2) material: Past and recent developments," *Inorganic Chemistry Communications*, vol. 121, p. 108200, 2020.

[88] J. You, S. Bongu, Q. Bao, and N. Panoiu, "Nonlinear optical properties and applications of 2d materials: theoretical and experimental aspects," *Nanophotonics*, vol. 8, no. 1, pp. 63–97, 2018.

[89] X. Gu, Y. Wei, X. Yin, B. Li, and R. Yang, “Phononic thermal properties of two-dimensional materials,” in *APS March Meeting Abstracts*, vol. 2018, 2018, pp. X29–001.

[90] X. Ling, H. Wang, S. Huang, F. Xia, and M. S. Dresselhaus, “The renaissance of black phosphorus,” *Proceedings of the National Academy of Sciences*, vol. 112, no. 15, pp. 4523–4530, 2015.

[91] A. K. Geim, “Graphene: status and prospects,” *science*, vol. 324, no. 5934, pp. 1530–1534, 2009.

[92] H. Jang, J. D. Wood, C. R. Ryder, M. C. Hersam, and D. G. Cahill, “Anisotropic thermal conductivity of exfoliated black phosphorus,” *arXiv preprint arXiv:1510.00051*, 2015.

[93] R. Zhang, J. Waters, A. K. Geim, and I. V. Grigorieva, “Intercalant-independent transition temperature in superconducting black phosphorus,” *Nature communications*, vol. 8, no. 1, p. 15036, 2017.

[94] Y. Cao, V. Fatemi, S. Fang, K. Watanabe, T. Taniguchi, E. Kaxiras, and P. Jarillo-Herrero, “Unconventional superconductivity in magic-angle graphene superlattices,” *Nature*, vol. 556, no. 7699, pp. 43–50, 2018.

[95] J. Biscaras, Z. Chen, A. Paradisi, and A. Shukla, “Onset of two-dimensional superconductivity in space charge doped few-layer molybdenum disulfide,” *Nature communications*, vol. 6, no. 1, p. 8826, 2015.

[96] J. Qiao, X. Kong, Z.-X. Hu, F. Yang, and W. Ji, “High-mobility transport anisotropy and linear dichroism in few-layer black phosphorus,” *Nature communications*, vol. 5, no. 1, p. 4475, 2014.

[97] C. Cai, T. Wang, G. Qu, and Z. Feng, “High thermal conductivity of graphene and structure defects: Prospects for thermal applications in graphene sheets,” *Chinese Chemical Letters*, vol. 32, no. 4, pp. 1293–1298, 2021.

[98] L. Banszerus, M. Schmitz, S. Engels, J. Dauber, M. Oellers, F. Haupt, K. Watanabe, T. Taniguchi, B. Beschoten, and C. Stampfer, “Ultrahigh-mobility graphene devices from chemical vapor deposition on reusable copper,” *Science advances*, vol. 1, no. 6, p. e1500222, 2015.

[99] X. Qi, X. Li, H. Jo, K. S. Bhat, S. Kim, J. An, J.-W. Kang, and S. Lim, “Mulberry paper-based graphene strain sensor for wearable electronics with high mechanical strength,” *Sensors and Actuators A: Physical*, vol. 301, p. 111697, 2020.

[100] F. Schwierz, “Graphene transistors,” *Nature nanotechnology*, vol. 5, no. 7, pp. 487–496, 2010.

[101] Y. Wu, Y.-m. Lin, A. A. Bol, K. A. Jenkins, F. Xia, D. B. Farmer, Y. Zhu, and P. Avouris, “High-frequency, scaled graphene transistors on diamond-like carbon,” *Nature*, vol. 472, no. 7341, pp. 74–78, 2011.

[102] J. Yu, G. Liu, A. V. Sumant, V. Goyal, and A. A. Balandin, “Graphene-on-diamond devices with increased current-carrying capacity: carbon sp2-on-sp3 technology,” *Nano letters*, vol. 12, no. 3, pp. 1603–1608, 2012.

[103] S. Majdi, V. Djurberg, M. Asad, A. Aitkulova, N. Suntornwipat, J. Stake, and J. Isberg, “Mobility enhancement in graphene-on-diamond heterostructures,” *Available at SSRN 4305764*.

[104] F. Zhao, A. Vrajitoarea, Q. Jiang, X. Han, A. Chaudhary, J. O. Welch, and R. B. Jackman, “Graphene-nanodiamond heterostructures and their application to high current devices,” *Scientific Reports*, vol. 5, no. 1, p. 13771, 2015.

[105] E. J. Lee, K. Balasubramanian, R. T. Weitz, M. Burghard, and K. Kern, “Contact and edge effects in graphene devices,” *Nature nanotechnology*, vol. 3, no. 8, pp. 486–490, 2008.

[106] Y. Wang, M. Jaiswal, M. Lin, S. Saha, B. Ozyilmaz, and K. P. Loh, “Electronic properties of nanodiamond decorated graphene,” *ACS nano*, vol. 6, no. 2, pp. 1018–1025, 2012.

[107] K. Ueda, S. Aichi, and H. Asano, “Photo-controllable memristive behavior of graphene/diamond heterojunctions,” *Applied Physics Letters*, vol. 108, no. 22, p. 222102, 2016.

[108] K. Ueda, H. Itou, and H. Asano, “Photomemristors using carbon nanowall/diamond heterojunctions,” *Journal of Materials Research*, vol. 34, no. 4, pp. 626–633, 2019.

[109] Y. Mizuno, Y. Ito, and K. Ueda, “Optoelectronic synapses using vertically aligned graphene/-diamond heterojunctions,” *Carbon*, vol. 182, pp. 669–676, 2021.

[110] S. Konabe, N. T. Cuong, M. Otani, and S. Okada, “High-efficiency photoelectric conversion in graphene–diamond hybrid structures: Model and first-principles calculations,” *Applied Physics Express*, vol. 6, no. 4, p. 045104, 2013.

[111] T. Shiga, S. Konabe, J. Shiomi, T. Yamamoto, S. Maruyama, and S. Okada, “Graphene-diamond hybrid structure as spin-polarized conducting wire with thermally efficient heat sinks,” *Applied Physics Letters*, vol. 100, no. 23, p. 233101, 2012.

[112] B. Shen, Z. Ji, Q. Lin, P. Gong, N. Xuan, S. Chen, H. Liu, Z. Huang, T. Xiao, and Z. Sun, “Graphenization of diamond,” *Chemistry of Materials*, vol. 34, no. 9, pp. 3941–3947, 2022.

[113] T. Yamada, T. Masuzawa, H. Mimura, and K. Okano, "Field emission spectroscopy measurements of graphene/n-type diamond heterojunction," *Applied Physics Letters*, vol. 114, no. 23, p. 231601, 2019.

[114] G. Wan, S. Panditharatne, N. A. Fox, and M. Cattelan, "Graphene-diamond junction photoemission microscopy and electronic interactions," *Nano Express*, vol. 1, no. 2, p. 020011, 2020.

[115] S. Zhao and K. Larsson, "First principle study of the attachment of graphene onto non-doped and doped diamond (111)," *Diamond and Related Materials*, vol. 66, pp. 52–60, 2016.

[116] C. Lu, H. Yang, J. Xu, L. Xu, M. Chshiev, S. Zhang, and C. Gu, "Spontaneous formation of graphene on diamond (111) driven by b-doping induced surface reconstruction," *Carbon*, vol. 115, pp. 388–393, 2017.

[117] Y. Kim, D. Lee, S. Y. Kim, E. Kang, and C. K. Kim, "Nanocomposite synthesis of nanodiamond and molybdenum disulfide," *Nanomaterials*, vol. 9, no. 7, p. 927, 2019.

[118] Y. Sasama, K. Komatsu, S. Moriyama, M. Imura, T. Teraji, K. Watanabe, T. Taniguchi, T. Uchihashi, and Y. Takahide, "High-mobility diamond field effect transistor with a monocrystalline h-bn gate dielectric," *APL Materials*, vol. 6, no. 11, p. 111105, 2018.

[119] S. Vishwakarma, J. M. Brown, A. Patel, M. R. McCartney, R. J. Nemanich, and D. J. Smith, "Growth and characterization of boron nitride/diamond heterostructures," *Microscopy and Microanalysis*, vol. 28, no. S1, pp. 2830–2831, 2022.

[120] A. Dettlaff, G. Skowierzak, Ł. Macewicz, M. Sobaszek, J. Karczewski, M. Sawczak, J. Ryl, T. Ossowski, and R. Bogdanowicz, "Electrochemical stability of few-layered phosphorene flakes on boron-doped diamond: a wide potential range of studies in aqueous solutions," *The Journal of Physical Chemistry C*, vol. 123, no. 33, pp. 20 233–20 240, 2019.

[121] N. Mao, J. Tang, L. Xie, J. Wu, B. Han, J. Lin, S. Deng, W. Ji, H. Xu, K. Liu *et al.*, "Optical anisotropy of black phosphorus in the visible regime," *Journal of the American Chemical Society*, vol. 138, no. 1, pp. 300–305, 2016.

[122] B. Deng, V. Tran, Y. Xie, H. Jiang, C. Li, Q. Guo, X. Wang, H. Tian, S. J. Koester, H. Wang *et al.*, "Efficient electrical control of thin-film black phosphorus bandgap," *Nature communications*, vol. 8, no. 1, p. 14474, 2017.

[123] Y. Du, H. Liu, Y. Deng, and P. D. Ye, "Device perspective for black phosphorus field-effect transistors: contact resistance, ambipolar behavior, and scaling," *ACS nano*, vol. 8, no. 10, pp. 10 035–10 042, 2014.

[124] B. C. Lee, C. M. Kim, H.-K. Jang, J. W. Lee, M.-K. Joo, and G.-T. Kim, "Degradation pattern of black phosphorus multilayer field- effect transistors in ambient conditions: Strategy for contact resistance engineering in bp transistors," *Applied Surface Science*, vol. 419, pp. 637–641, 2017.

[125] S. Handschuh-Wang, T. Wang, and Y. Tang, "Ultrathin diamond nanofilms—development, challenges, and applications," *Small*, vol. 17, no. 30, p. 2007529, 2021.

[126] V. Seshan, J. Island, R. Van Leeuwen, W. Venstra, B. Schneider, S. D. Janssens, K. Haenen, E. Sudhölter, L. De Smet, H. Van Der Zant *et al.*, "Pick-up and drop transfer of diamond nanosheets," *Nanotechnology*, vol. 26, no. 12, p. 125706, 2015.

[127] H. Jang, I.-S. Kang, Y. Lee, Y. J. Cha, D. K. Yoon, C. W. Ahn, and W. Lee, "Direct transfer of multilayer graphene grown on a rough metal surface using pdms adhesion engineering," *Nanotechnology*, vol. 27, no. 36, p. 365705, 2016.

[128] K. Kinoshita, R. Moriya, M. Onodera, Y. Wakafuji, S. Masubuchi, K. Watanabe, T. Taniguchi, and T. Machida, "Dry release transfer of graphene and few-layer h-bn by utilizing thermoplasticity of polypropylene carbonate," *npj 2D Materials and Applications*, vol. 3, no. 1, p. 22, 2019.

[129] J. Davidson, D. Wur, W. Kang, D. Kinser, and D. Kerns, "Polycrystalline diamond pressure microsensor," *Diamond and related Materials*, vol. 5, no. 1, pp. 86–92, 1996.

[130] A. Yamamoto, N. Norio, and T. Takahiro, "Evaluation of diamond gauge factor up to 500° c," *Diamond and related materials*, vol. 16, no. 8, pp. 1670–1675, 2007.

[131] S. Janssens, S. Drijkoningen, and K. Haenen, "Ultra-thin nanocrystalline diamond membranes as pressure sensors for harsh environments," *Applied Physics Letters*, vol. 104, no. 7, p. 073107, 2014.

[132] K. Bray, B. Regan, A. Trycz, R. Previdi, G. Seniutinas, K. Ganesan, M. Kianinia, S. Kim, and I. Aharonovich, "Single crystal diamond membranes and photonic resonators containing germanium vacancy color centers," *ACS Photonics*, vol. 5, no. 12, pp. 4817–4822, 2018.

[133] C. Dang, J.-P. Chou, B. Dai, C.-T. Chou, Y. Yang, R. Fan, W. Lin, F. Meng, A. Hu, J. Zhu *et al.*, "Achieving large uniform tensile elasticity in microfabricated diamond," *Science*, vol. 371, no. 6524, pp. 76–78, 2021.

[134] M. A. Lodes, S. M. Rosiwal, and R. F. Singer, "Self-supporting nanocrystalline diamond foils–a new concept for crystalline diamond on any technical surface," in *Key Engineering Materials*, vol. 438. Trans Tech Publ, 2010, pp. 163–169.

[135] R. Ramakrishnan, M. A. Lodes, S. M. Rosiwal, and R. F. Singer, "Self-supporting nanocrystalline diamond foils: Influence of template morphologies on the mechanical properties measured by ball on three balls testing," *Acta Materialia*, vol. 59, no. 9, pp. 3343–3351, 2011.

[136] S. Böttner, M. R. Jorgensen, and O. G. Schmidt, "Rolled-up nanotechnology: 3d photonic materials by design," *Scripta Materialia*, vol. 122, pp. 119–124, 2016.

[137] D. Briukhanova, M. Habib, I. Issah, and H. Caglayan, "Low loss fishnet metamaterial via self-rolled nanotechnology," *Applied Physics Letters*, vol. 119, no. 14, p. 141101, 2021.

[138] C. Vervacke, C. C. B. Bufon, D. J. Thurmer, and O. G. Schmidt, "Three-dimensional chemical sensors based on rolled-up hybrid nanomembranes," *RSC Advances*, vol. 4, no. 19, pp. 9723–9729, 2014.

[139] G. Huang, V. A. Bolanos Quinones, F. Ding, S. Kiravittaya, Y. Mei, and O. G. Schmidt, "Rolled-up optical microcavities with subwavelength wall thicknesses for enhanced liquid sensing applications," *Acs Nano*, vol. 4, no. 6, pp. 3123–3130, 2010.

[140] W. Si, I. Mönch, C. Yan, J. Deng, S. Li, G. Lin, L. Han, Y. Mei, and O. G. Schmidt, "A single rolled-up si tube battery for the study of electrochemical kinetics, electrical conductivity, and structural integrity," *Advanced Materials*, vol. 26, no. 47, pp. 7973–7978, 2014.

[141] Z. Tian, L. Zhang, Y. Fang, B. Xu, S. Tang, N. Hu, Z. An, Z. Chen, and Y. Mei, "Deterministic self-rolling of ultrathin nanocrystalline diamond nanomembranes for 3d tubular/helical architecture," *Advanced Materials*, vol. 29, no. 13, p. 1604572, 2017.

[142] F. S. Kachold, M. A. Lodes, S. M. Rosiwal, and R. F. Singer, "Direct measurement of young's modulus, fracture strength and fracture toughness of nanocrystalline diamond foil by means of tensile testing," *Acta materialia*, vol. 61, no. 18, pp. 7000–7008, 2013.

[143] S. Sobolewski, M. A. Lodes, S. M. Rosiwal, and R. F. Singer, "Surface energy of growth and seeding side of free standing nanocrystalline diamond foils," *Surface and Coatings Technology*, vol. 232, pp. 640–644, 2013.

[144] M. Tsigkourakos, T. Hantschel, C. Bangerter, and W. Vandervorst, "Electrical probing of b-doped diamond seeds embedded into the interfacial layer of a conductive diamond film," *physica status solidi (a)*, vol. 211, no. 10, pp. 2284–2289, 2014.

[145] L. Ostrovskaya, V. Perevertailo, V. Ralchenko, A. Dementjev, and O. Loginova, "Wettability and surface energy of oxidized and hydrogen plasma-treated diamond films," *Diamond and Related Materials*, vol. 11, no. 3-6, pp. 845–850, 2002.

[146] R. Bogdanowicz, A. Fabiańska, L. Golunski, M. Sobaszek, M. Gnyba, J. Ryl, K. Darowicki, T. Ossowski, S. D. Janssens, K. Haenen *et al.*, "Influence of the boron doping level on the electrochemical oxidation of the azo dyes at si/bdd thin film electrodes," *Diamond and Related Materials*, vol. 39, pp. 82–88, 2013.

[147] M. Tsigkourakos, T. Hantschel, Z. Xu, B. Douhard, J. Meersschaut, Y. Zou, K. Larsson, M. Boman, and W. Vandervorst, "Suppression of boron incorporation at the early growth phases of boron-doped diamond thin films," *physica status solidi (a)*, vol. 212, no. 11, pp. 2595–2599, 2015.

[148] Z. Jian, J. Xu, N. Yang, S. Han, and X. Jiang, "A perspective on diamond composites and their electrochemical applications," *Current Opinion in Electrochemistry*, vol. 30, p. 100835, 2021.

[149] P. Rath, S. Khasminskaya, C. Nebel, C. Wild, and W. H. Pernice, "Diamond-integrated optomechanical circuits," *Nature communications*, vol. 4, no. 1, p. 1690, 2013.

[150] O. Babchenko, A. Kromka, J. P. Conde, V. Chu, T. Schmiedinger, and B. Rezek, "Optically transparent diamond–pdms microfluidic system for electronic monitoring of cells," *physica status solidi (b)*, vol. 251, no. 12, pp. 2593–2598, 2014.

[151] Y. Xie, H. Wang, D. Cheng, H. Ding, D. Kong, L. Li, L. Yin, G. Zhao, L. Liu, G. Zou *et al.*, "Diamond thin films integrated with flexible substrates and their physical, chemical and biological characteristics," *Journal of Physics D: Applied Physics*, vol. 54, no. 38, p. 384004, 2021.

[152] B. Fan, Y. Zhu, R. Rechenberg, C. A. Rusinek, M. F. Becker, and W. Li, "Large-scale, all poly-crystalline diamond structures transferred onto flexible parylene-c films for neurotransmitter sensing," *Lab on a Chip*, vol. 17, no. 18, pp. 3159–3167, 2017.

[153] H. Li, K. Zhou, J. Cao, Q. Wei, C.-T. Lin, S. E. Pei, L. Ma, N. Hu, Y. Guo, Z. Deng *et al.*, "A novel modification to boron-doped diamond electrode for enhanced, selective detection of dopamine in human serum," *Carbon*, vol. 171, pp. 16–28, 2021.

[154] C. Martínez-Huitle, N. S. Fernandes, S. Ferro, A. De Battisti, and M. Quiroz, "Fabrication and application of nafion®-modified boron-doped diamond electrode as sensor for detecting caffeine," *Diamond and Related Materials*, vol. 19, no. 10, pp. 1188–1193, 2010.

[155] P. Bergonzo, A. Bongrain, E. Scorsone, A. Bendali, L. Rousseau, G. Lissorgues, P. Mailley, Y. Li, T. Kauffmann, F. Goy *et al.*, "3d shaped mechanically flexible diamond microelectrode

arrays for eye implant applications: The medinas project," *Irbm*, vol. 32, no. 2, pp. 91–94, 2011.

[156] A. E. Hess, D. M. Sabens, H. B. Martin, and C. A. Zorman, "Diamond-on-polymer microelectrode arrays fabricated using a chemical release transfer process," *Journal of microelectromechanical systems*, vol. 20, no. 4, pp. 867–875, 2011.

[157] U. Kalsoom, A. Peristyy, P. Nesterenko, and B. Paull, "A 3d printable diamond polymer composite: a novel material for fabrication of low cost thermally conducting devices," *RSC advances*, vol. 6, no. 44, pp. 38 140–38 147, 2016.

[158] U. Kalsoom, S. Waheed, and B. Paull, "Fabrication of humidity sensor using 3d printable polymer composite containing boron-doped diamonds and licl," *ACS applied materials & interfaces*, vol. 12, no. 4, pp. 4962–4969, 2020.

[159] J. H. Luong, K. B. Male, and J. D. Glennon, "Boron-doped diamond electrode: synthesis, characterization, functionalization and analytical applications," *Analyst*, vol. 134, no. 10, pp. 1965–1979, 2009.

[160] K. Muzyka, J. Sun, T. H. Fereja, Y. Lan, W. Zhang, and G. Xu, "Boron-doped diamond: Current progress and challenges in view of electroanalytical applications," *Analytical methods*, vol. 11, no. 4, pp. 397–414, 2019.

[161] N. Elgrishi, K. J. Rountree, B. D. McCarthy, E. S. Rountree, T. T. Eisenhart, and J. L. Dempsey, "A practical beginner's guide to cyclic voltammetry," *Journal of chemical education*, vol. 95, no. 2, pp. 197–206, 2018.

[162] A. Hanawa, K. Asai, G. Ogata, H. Hibino, and Y. Einaga, "Electrochemical measurement of lamotrigine using boron-doped diamond electrodes," *Electrochimica Acta*, vol. 271, pp. 35–40, 2018.

[163] K. Bakowicz-Mitura, G. Bartosz, and S. Mitura, "Influence of diamond powder particles on human gene expression," *Surface and Coatings Technology*, vol. 201, no. 13, pp. 6131–6135, 2007.

[164] D. Pappalardo, T. Mathisen, and A. Finne-Wistrand, "Biocompatibility of resorbable polymers: a historical perspective and framework for the future," *Biomacromolecules*, vol. 20, no. 4, pp. 1465–1477, 2019.

[165] D. Nidzworski, K. Siuzdak, P. Niedziałkowski, R. Bogdanowicz, M. Sobaszek, J. Ryl, P. Weiher, M. Sawczak, E. Wnuk, W. A. Goddard *et al.*, "A rapid-response ultrasensitive biosensor for

influenza virus detection using antibody modified boron-doped diamond," *Scientific reports*, vol. 7, no. 1, pp. 1–10, 2017.

[166] P. F. Pereira, M. C. Marra, A. B. Lima, W. T. P. dos Santos, R. A. A. Munoz, and E. M. Richter, "Fast and simultaneous determination of nimesulide and paracetamol by batch injection analysis with amperometric detection on bare boron-doped diamond electrode," *Diamond and Related Materials*, vol. 39, pp. 41–46, 2013.

[167] Z. Liu, A. F. Sartori, and J. G. Buijnsters, "Role of sp2 carbon in non-enzymatic electrochemical sensing of glucose using boron-doped diamond electrodes," *Electrochemistry Communications*, vol. 130, p. 107096, 2021.

[168] F. Gao and C. E. Nebel, "Electrically conductive diamond membrane for electrochemical separation processes," *ACS Applied Materials & Interfaces*, vol. 8, no. 28, pp. 18 640–18 646, 2016.

[169] S. Ruffinatto, H. Girard, F. Becher, J.-C. Arnault, D. Tromson, and P. Bergonzo, "Diamond porous membranes: A material toward analytical chemistry," *Diamond and Related Materials*, vol. 55, pp. 123–130, 2015.

[170] L. Jiang, I. Santiago, and J. Foord, "A comparative study of fouling-free nanodiamond and nanocarbon electrochemical sensors for sensitive bisphenol a detection," *Carbon*, vol. 174, pp. 390–395, 2021.

[171] B. B. Petković, M. Ognjanović, M. Krstić, V. Stanković, L. Babincev, M. Pergal, and D. M. Stanković, "Boron-doped diamond electrode as efficient sensing platform for simultaneous quantification of mefenamic acid and indomethacin," *Diamond and Related Materials*, vol. 105, p. 107785, 2020.

[172] M. Burian and G. Geisslinger, "Cox-dependent mechanisms involved in the antinociceptive action of nsaids at central and peripheral sites," *Pharmacology & therapeutics*, vol. 107, no. 2, pp. 139–154, 2005.

[173] M. Mahadik, S. Dhaneshwar, and R. Bhavsar, "A high performance liquid chromatography–tandem mass spectrometric method for the determination of mefenamic acid in human plasma: application to pharmacokinetic study," *Biomedical Chromatography*, vol. 26, no. 10, pp. 1137–1142, 2012.

[174] S. N. Shah, A. Z. Mirza, H. Shamshad, N. Shafi, and M. A. Naz, "Physical and chemical characterization of mefenamic acid in different pharmaceutical dosage forms and their

stability studies using novel rp-hplc method," *Medicinal Chemistry Research*, vol. 21, pp. 3591–3597, 2012.

[175] S. Husain, M. Kifayatullah, and R. Sekar, "Simultaneous determination of mefenamic acid and paracetamol in pharmaceutical preparations by 1 h-nuclear magnetic resonance spectroscopy," 2001.

[176] W. Isaacson, *Steve Jobs*. Little, Brown, 2013. [Online]. Available: https://books.google.pl/books?id=hFm3lwEACAAJ

[177] R. Bogdanowicz, M. Ficek, M. Sobaszek, A. Nosek, Ł. Gołuński, J. Karczewski, A. Jaramillo-Botero, W. A. Goddard III, M. Bockrath, and T. Ossowski, "Growth and isolation of large area boron-doped nanocrystalline diamond sheets: a route toward diamond-on-graphene heterojunction," *Advanced Functional Materials*, vol. 29, no. 3, p. 1805242, 2019.

[178] A. A. S. Bhagat, P. Jothimuthu, and I. Papautsky, "Photodefinable polydimethylsiloxane (pdms) for rapid lab-on-a-chip prototyping," *Lab on a Chip*, vol. 7, no. 9, pp. 1192–1197, 2007.

[179] K. Raj M and S. Chakraborty, "Pdms microfluidics: A mini review," *Journal of Applied Polymer Science*, vol. 137, no. 27, p. 48958, 2020.

[180] A. Hammoud, E. Baumann, E. Overton, I. Myers, J. Suthar, W. Khachen, and J. Laghari, "High temperature dielectric properties of apical, kapton, peek, teflon af, and upilex polymers," in *[Proceedings] 1992 Annual Report: Conference on Electrical Insulation and Dielectric Phenomena*. IEEE, 1992, pp. 549–554.

[181] L. M. Júnior, L. M. de Oliveira, P. F. J. Bócoli, M. Cristianini, M. Padula, and C. A. R. Anjos, "Morphological, thermal and mechanical properties of polyamide and ethylene vinyl alcohol multilayer flexible packaging after high-pressure processing," *Journal of Food Engineering*, vol. 276, p. 109913, 2020.

[182] J. Faist, F. Capasso, D. L. Sivco, C. Sirtori, A. L. Hutchinson, and A. Y. Cho, "Quantum cascade laser," *Science*, vol. 264, no. 5158, pp. 553–556, 1994.

[183] K. S. Novoselov, A. Mishchenko, o. A. Carvalho, and A. Castro Neto, "2d materials and van der waals heterostructures," *Science*, vol. 353, no. 6298, p. aac9439, 2016.

[184] N. Woehrl, T. Hirte, O. Posth, and V. Buck, "Investigation of the coefficient of thermal expansion in nanocrystalline diamond films," *Diamond and related materials*, vol. 18, no. 2-3, pp. 224–228, 2009.

[185] A. Jain, P. Bharadwaj, S. Heeg, M. Parzefall, T. Taniguchi, K. Watanabe, and L. Novotny, "Minimizing residues and strain in 2d materials transferred from pdms," *Nanotechnology*, vol. 29, no. 26, p. 265203, 2018.

[186] F. Pizzocchero, L. Gammelgaard, B. S. Jessen, J. M. Caridad, L. Wang, J. Hone, P. Bøggild, and T. J. Booth, "The hot pick-up technique for batch assembly of van der waals heterostructures," *Nature communications*, vol. 7, no. 1, p. 11894, 2016.

[187] K. Kim, M. Yankowitz, B. Fallahazad, S. Kang, H. C. Movva, S. Huang, S. Larentis, C. M. Corbet, T. Taniguchi, K. Watanabe *et al.*, "van der waals heterostructures with high accuracy rotational alignment," *Nano letters*, vol. 16, no. 3, pp. 1989–1995, 2016.

[188] A. Castellanos-Gomez, M. Buscema, R. Molenaar, V. Singh, L. Janssen, H. S. Van Der Zant, and G. A. Steele, "Deterministic transfer of two-dimensional materials by all-dry viscoelastic stamping," *2D Materials*, vol. 1, no. 1, p. 011002, 2014.

[189] Q. Zhao, T. Wang, Y. K. Ryu, R. Frisenda, and A. Castellanos-Gomez, "An inexpensive system for the deterministic transfer of 2d materials," *Journal of Physics: Materials*, vol. 3, no. 1, p. 016001, 2020.

[190] Z. Sun, J. Shi, B. Tay, and S. P. Lau, "Uv raman characteristics of nanocrystalline diamond films with different grain size," *Diamond and related materials*, vol. 9, no. 12, pp. 1979–1983, 2000.

[191] Y. Namba, E. Heidarpour, and M. Nakayama, "Size effects appearing in the raman spectra of polycrystalline diamonds," *Journal of Applied Physics*, vol. 72, no. 5, pp. 1748–1751, 1992.

[192] J. Michler, Y. Von Kaenel, J. Stiegler, and E. Blank, "Complementary application of electron microscopy and micro-raman spectroscopy for microstructure, stress, and bonding defect investigation of heteroepitaxial chemical vapor deposited diamond films," *Journal of applied physics*, vol. 83, no. 1, pp. 187–197, 1998.

[193] H. Li, T. Zhang, L. Li, X. Lü, B. Li, Z. Jin, and G. Zou, "Investigation on crystalline structure, boron distribution, and residual stresses in freestanding boron-doped cvd diamond films," *Journal of crystal growth*, vol. 312, no. 12-13, pp. 1986–1991, 2010.

[194] M. Bernard, A. Deneuville, and P. Muret, "Non-destructive determination of the boron concentration of heavily doped metallic diamond thin films from raman spectroscopy," *Diamond and Related Materials*, vol. 13, no. 2, pp. 282–286, 2004.

[195] J. G. Buijnsters, M. Tsigkourakos, T. Hantschel, F. O. Gomes, T. Nuytten, P. Favia, H. Bender, K. Arstila, J.-P. Celis, and W. Vandervorst, "Effect of boron doping on the wear behavior of the

growth and nucleation surfaces of micro-and nanocrystalline diamond films," *ACS Applied Materials & Interfaces*, vol. 8, no. 39, pp. 26 381–26 391, 2016.

[196] P. May, W. Ludlow, M. Hannaway, P. Heard, J. Smith, and K. Rosser, "Raman and conductivity studies of boron-doped microcrystalline diamond, facetted nanocrystalline diamond and cauliflower diamond films," *Diamond and Related Materials*, vol. 17, no. 2, pp. 105–117, 2008.

[197] B. Fan, C. A. Rusinek, C. H. Thompson, M. Setien, Y. Guo, R. Rechenberg, Y. Gong, A. J. Weber, M. F. Becker, E. Purcell *et al.*, "Flexible, diamond-based microelectrodes fabricated using the diamond growth side for neural sensing," *Microsystems & nanoengineering*, vol. 6, no. 1, p. 42, 2020.

[198] M. Daenen, O. A. Williams, J. D'Haen, K. Haenen, and M. Nesládek, "Seeding, growth and characterization of nanocrystalline diamond films on various substrates," *physica status solidi (a)*, vol. 203, no. 12, pp. 3005–3010, 2006.

[199] L. Mosińska, "Badanie właściwości warstw diamentowych otrzymanych metodą chemicznego osadzania z fazy gazowej pod kątem zastosowań w elektrochemii," Ph.D. dissertation, Poznań, 2018.

[200] B. Massarani, J. Bourgoin, and R. Chrenko, "Hopping conduction in semiconducting diamond," *Physical review B*, vol. 17, no. 4, p. 1758, 1978.

[201] T. Borst and O. Weis, "Boron-doped homoepitaxial diamond layers: Fabrication, characterization, and electronic applications," *physica status solidi (a)*, vol. 154, no. 1, pp. 423–444, 1996.

[202] A. Banaszak-Piechowska, K. Fabisiak, E. Staryga, and K. Paprocki, "Electrical properties and mott parameters of polycrystalline diamond films synthesized by hf cvd method from hydrogen/methanol gas mixture," *Materials Science-Poland*, vol. 35, no. 4, pp. 830–837, 2017.

[203] M. Werner and R. Locher, "Growth and application of undoped and doped diamond films," *Reports on Progress in Physics*, vol. 61, no. 12, p. 1665, 1998.

[204] T. Wakita, K. Terashima, and T. Yokoya, "Physics of heavily doped diamond: Electronic states and superconductivity," *Physics and Chemistry of Carbon-Based Materials: Basics and Applications*, pp. 65–96, 2019.

[205] T. Lee and T. McGill, "Variation of impurity- to- band activation energies with impurity density," *Journal of applied physics*, vol. 46, no. 1, pp. 373–380, 1975.

[206] F. Fontaine, “Calculation of the hole concentration in boron-doped diamond,” *Journal of applied physics*, vol. 85, no. 3, pp. 1409–1422, 1999.

[207] K. Tsukioka and H. Okushi, “Hall mobility and scattering mechanism of holes in boron-doped homoepitaxial chemical vapor deposition diamond thin films,” *Japanese journal of applied physics*, vol. 45, no. 11R, p. 8571, 2006.

[208] V. Bormashov, S. Tarelkin, S. Buga, M. Kuznetsov, S. Terentiev, A. Semenov, and V. Blank, “Electrical properties of the high quality boron-doped synthetic single-crystal diamonds grown by the temperature gradient method,” *Diamond and related materials*, vol. 35, pp. 19–23, 2013.

[209] G. Zhang, S. Janssens, J. Vanacken, M. Timmermans, J. Vacík, G. Ataklti, W. Decelle, W. Gillijns, B. Goderis, K. Haenen *et al.*, “Role of grain size in superconducting boron-doped nanocrystalline diamond thin films grown by cvd,” *Physical Review B*, vol. 84, no. 21, p. 214517, 2011.

[210] O. A. Williams, M. Nesladek, M. Daenen, S. Michaelson, A. Hoffman, E. Osawa, K. Haenen, and R. Jackman, “Growth, electronic properties and applications of nanodiamond,” *Diamond and Related Materials*, vol. 17, no. 7-10, pp. 1080–1088, 2008.

[211] A. Zieliński, R. Bogdanowicz, J. Ryl, L. Burczyk, and K. Darowicki, “Local impedance imaging of boron-doped polycrystalline diamond thin films,” *Applied Physics Letters*, vol. 105, no. 13, p. 131908, 2014.

[212] C. E. Nebel, “Electronic properties of cvd diamond,” *Semiconductor Science and Technology*, vol. 18, no. 3, p. S1, 2003.

[213] E. Conwell and V. Weisskopf, “Theory of impurity scattering in semiconductors,” *Physical review*, vol. 77, no. 3, p. 388, 1950.

[214] T. Stuchliková, Z. Remes, V. Mortet, A. Taylor, P. Ashcheulov, J. Stuchlik, and V. Volodin, “Electrical and optical characteristics of boron doped nanocrystalline diamond films,” *Vacuum*, vol. 168, p. 108813, 2019.

[215] L. A. Hutton, J. G. Iacobini, E. Bitziou, R. B. Channon, M. E. Newton, and J. V. Macpherson, “Examination of the factors affecting the electrochemical performance of oxygen-terminated polycrystalline boron-doped diamond electrodes,” *Analytical chemistry*, vol. 85, no. 15, pp. 7230–7240, 2013.

[216] X. C. Wang, B. Shen, and F. H. Sun, “Deposition and characterization of boron-doped hfcvd diamond films on ti, sic, si and ta substrates,” in *Applied Mechanics and Materials*, vol. 217. Trans Tech Publ, 2012, pp. 1062–1067.

[217] A. Tallaire, M. Kasu, K. Ueda, and T. Makimoto, “Origin of growth defects in cvd diamond epitaxial films,” *Diamond and Related Materials*, vol. 17, no. 1, pp. 60–65, 2008.

[218] S. Samsonenko and N. Samsonenko, “Dislocation electrical conductivity of synthetic diamond films,” *Semiconductors*, vol. 43, no. 5, pp. 594–598, 2009.

[219] N. Mott and E. Davis, *Electronic process in non-crystalline materials*. Oxford University Press, 1971.

[220] N. Mott, “Conduction in non-crystalline systems ix. the minimum metallic conductivity,” *Philosophical Magazine*, vol. 26, no. 4, pp. 1015–1026, 1972.

[221] E. Davis and N. Mott, “Conduction in non-crystalline systems v. conductivity, optical absorption and photoconductivity in amorphous semiconductors,” *Philosophical magazine*, vol. 22, no. 179, pp. 0903–0922, 1970.

[222] N. F. Mott, “Conduction in non-crystalline materials: Iii. localized states in a pseudogap and near extremities of conduction and valence bands,” *Philosophical Magazine*, vol. 19, no. 160, pp. 835–852, 1969.

[223] A. Fischer-Cripps, “Handbook of nanoindentation,” *Fischer-Cripps Laboratories Pty Ltd, Forestville, Australia*, 2013.

[224] S. Bull, “On the origins and mechanisms of the indentation size effect,” *International Journal of Materials Research*, vol. 94, no. 7, pp. 787–792, 2022.

[225] W. D. Nix and H. Gao, “Indentation size effects in crystalline materials: a law for strain gradient plasticity,” *Journal of the Mechanics and Physics of Solids*, vol. 46, no. 3, pp. 411–425, 1998.

[226] G. He, C. Xu, C. Liu, H. Liu, and H. Wang, “Grain size and temperature effects on the indentation induced plastic deformations of nano polycrystalline diamond,” *Applied Surface Science*, vol. 480, pp. 349–360, 2019.

[227] K. Durst, B. Backes, O. Franke, and M. Göken, “Indentation size effect in metallic materials: Modeling strength from pop-in to macroscopic hardness using geometrically necessary dislocations,” *Acta Materialia*, vol. 54, no. 9, pp. 2547–2555, 2006.

[228] Z. Liu, S. Baluchová, A. F. Sartori, Z. Li, Y. Gonzalez-Garcia, M. Schreck, and J. G. Buijnsters, “Heavily boron-doped diamond grown on scalable heteroepitaxial quasi-substrates: A

promising single crystal material for electrochemical sensing applications," *Carbon*, vol. 201, pp. 1229–1240, 2023.

[229] M. H. McLaughlin, E. Corcoran, A. C. Pakpour-Tabrizi, D. C. de Faria, and R. B. Jackman, "Influence of temperature on the electrochemical window of boron doped diamond: a comparison of commercially available electrodes," *Scientific Reports*, vol. 10, no. 1, pp. 1–9, 2020.

[230] G. R. Salazar-Banda, L. S. Andrade, P. A. Nascente, P. S. Pizani, R. C. Rocha-Filho, and L. A. Avaca, "On the changing electrochemical behaviour of boron-doped diamond surfaces with time after cathodic pre-treatments," *Electrochimica Acta*, vol. 51, no. 22, pp. 4612–4619, 2006.

[231] Y. Einaga, "Development of electrochemical applications of boron-doped diamond electrodes," *Bulletin of the Chemical Society of Japan*, vol. 91, no. 12, pp. 1752–1762, 2018.

[232] J. Xu, Y. Yokota, R. A. Wong, Y. Kim, and Y. Einaga, "Unusual electrochemical properties of low-doped boron-doped diamond electrodes containing sp2 carbon," *Journal of the American Chemical Society*, vol. 142, no. 5, pp. 2310–2316, 2020.

[233] Y. V. Pleskov, Y. E. Evstefeeva, M. Krotova, V. Varnin, and I. Teremetskaya, "Synthetic semiconductor diamond electrodes: Electrochemical behaviour of homoepitaxial boron-doped films orientated as (1 1 1),(1 1 0), and (1 0 0) faces," *Journal of Electroanalytical Chemistry*, vol. 595, no. 2, pp. 168–174, 2006.

[234] S. C. B. Oliveira and A. M. Oliveira-Brett, "Voltammetric and electrochemical impedance spectroscopy characterization of a cathodic and anodic pre-treated boron doped diamond electrode," *Electrochimica Acta*, vol. 55, no. 15, pp. 4599–4605, 2010.

[235] S. Baluchova, A. Taylor, V. Mortet, S. Sedlakova, L. Klimša, J. Kopeček, O. Hák, and K. Schwarzova-Peckova, "Porous boron doped diamond for dopamine sensing: Effect of boron doping level on morphology and electrochemical performance," *Electrochimica Acta*, vol. 327, p. 135025, 2019.

[236] K. Cinková, C. Batchelor-McAuley, M. Marton, M. Vojs, L. Švorc, and R. G. Compton, "The activity of non-metallic boron-doped diamond electrodes with sub-micron scale heterogeneity and the role of the morphology of sp2 impurities," *Carbon*, vol. 110, pp. 148–154, 2016.

[237] M. C. Granger, M. Witek, J. Xu, J. Wang, M. Hupert, A. Hanks, M. D. Koppang, J. E. Butler, G. Lucazeau, M. Mermoux *et al.*, "Standard electrochemical behavior of high-quality, boron-

doped polycrystalline diamond thin-film electrodes," *Analytical chemistry*, vol. 72, no. 16, pp. 3793–3804, 2000.

[238] P. Sharma and T. Bhatti, "A review on electrochemical double-layer capacitors," *Energy conversion and management*, vol. 51, no. 12, pp. 2901–2912, 2010.

[239] G. Oskam, D. Vanmaekelbergh, and J. Kelly, "A reappraisal of the frequency dependence of the impedance of semiconductor electrodes," *Journal of electroanalytical chemistry and interfacial electrochemistry*, vol. 315, no. 1-2, pp. 65–85, 1991.

[240] P. Yu, J. Zhang, T. Zheng, and T. Wang, "Influence of boron doped level on the electrochemical behavior of boron doped diamond electrodes and uric acid detection," *Colloids and Surfaces A: Physicochemical and Engineering Aspects*, vol. 494, pp. 241–247, 2016.

[241] M. Abaturov, V. Bakin, and M. Krotova, "Definition of concentration and profile of concentration of the doping impurity in semiconductor electrodes," *Elektrokhimiya*, vol. 31, pp. 1214–1220, 1995.

[242] J. Van de Lagemaat, D. Vanmaekelbergh, and J. Kelly, "Electrochemistry of homoepitaxial cvd diamond: energetics and electrode kinetics in aqueous electrolytes," *Journal of Electroanalytical Chemistry*, vol. 475, no. 2, pp. 139–151, 1999.

[243] A. F. Sartori, "Heteroepitaxial boron-doped diamond: from synthesis to application," Ph.D. dissertation, Augsburg, 2016.

[244] M. Baldan, A. Azevedo, A. Couto, and N. Ferreira, "Cathodic and anodic pre-treated boron doped diamond with different sp2 content: Morphological, structural, and impedance spectroscopy characterizations," *Journal of Physics and Chemistry of Solids*, vol. 74, no. 12, pp. 1830–1835, 2013.

[245] Z. V. Živcová, V. Petrák, O. Frank, and L. Kavan, "Electrochemical impedance spectroscopy of polycrystalline boron doped diamond layers with hydrogen and oxygen terminated surface," *Diamond and Related Materials*, vol. 55, pp. 70–76, 2015.

[246] C. Pietzka, A. Denisenko, A. Romanyuk, P. Schäfer, L. A. Kibler, J. Scharpf, and E. Kohn, "Electronic surface barrier properties of boron-doped diamond oxidized by plasma treatment," *Diamond and related materials*, vol. 19, no. 2-3, pp. 213–216, 2010.

[247] N. Simon, H. Girard, M. Manesse, D. Ballutaud, and A. Etcheberry, "Electrochemical preconditioning of moderately boron doped diamond electrodes: Effect of annealing," *Diamond and related materials*, vol. 17, no. 7-10, pp. 1371–1375, 2008.

[248] J. A. Bennett, J. Wang, Y. Show, and G. M. Swain, “Effect of sp2-bonded nondiamond carbon impurity on the response of boron-doped polycrystalline diamond thin-film electrodes,” *Journal of The Electrochemical Society*, vol. 151, no. 9, p. E306, 2004.

[249] J. V. Macpherson, “A practical guide to using boron doped diamond in electrochemical research,” *Physical Chemistry Chemical Physics*, vol. 17, no. 5, pp. 2935–2949, 2015.

[250] H. Yang, Y. Ma, and Y. Dai, “Progress of structural and electronic properties of diamond: a mini review,” *Functional Diamond*, vol. 1, no. 1, pp. 150–159, 2022.

[251] K. Devarayan, D. Lei, H.-Y. Kim, and B.-S. Kim, “Flexible transparent electrode based on pani nanowire/nylon nanofiber reinforced cellulose acetate thin film as supercapacitor,” *Chemical Engineering Journal*, vol. 273, pp. 603–609, 2015.

[252] D. Tsubone, T. Hasebe, A. Kamijo, and A. Hotta, “Fracture mechanics of diamond-like carbon (dlc) films coated on flexible polymer substrates,” *Surface and Coatings Technology*, vol. 201, no. 14, pp. 6423–6430, 2007.

[253] L.-P. Ma, W. Ren, and H.-M. Cheng, “Transfer methods of graphene from metal substrates: A review,” *Small Methods*, vol. 3, no. 7, p. 1900049, 2019.

[254] W. Jung, D. Kim, M. Lee, S. Kim, J.-H. Kim, and C.-S. Han, “Ultraconformal contact transfer of monolayer graphene on metal to various substrates,” *Advanced Materials*, vol. 26, no. 37, pp. 6394–6400, 2014.

[255] A. S. Cruz-Félix, A. Santiago-Alvarado, J. Márquez-García, and J. González-García, “Pdms samples characterization with variations of synthesis parameters for tunable optics applications,” *Heliyon*, vol. 5, no. 12, p. e03064, 2019.

[256] K. Khanafer, A. Duprey, M. Schlicht, and R. Berguer, “Effects of strain rate, mixing ratio, and stress–strain definition on the mechanical behavior of the polydimethylsiloxane (pdms) material as related to its biological applications,” *Biomedical microdevices*, vol. 11, pp. 503–508, 2009.

[257] I. Grabowska, M. Sajnoga, M. Juchniewicz, M. Chudy, A. Dybko, and Z. Brzozka, “Microfluidic system with electrochemical and optical detection,” *Microelectronic engineering*, vol. 84, no. 5-8, pp. 1741–1743, 2007.

[258] S. Gupta, B. R. Weiner, and G. Morell, “Spectroscopic ellipsometry studies of nanocrystalline carbon thin films deposited by hfcvd,” *Diamond and related materials*, vol. 10, no. 11, pp. 1968–1972, 2001.

[259] A. Majumdar, S. C. Das, R. Bogdanowicz, T. Shripathi, W. Langel, and R. Hippler, "Role of nitrogen in evolution of sp2/sp3 bonding and optical band gap in hydrogenated carbon nitride," *Vibrational Spectroscopy*, vol. 66, pp. 63–68, 2013.

[260] V. Ralchenko, S. Pimenov, V. Konov, A. Khomich, A. Saveliev, A. Popovich, I. Vlasov, E. Zavedeev, A. Bozhko, E. Loubnin *et al.*, "Nitrogenated nanocrystalline diamond films: Thermal and optical properties," *Diamond and Related Materials*, vol. 16, no. 12, pp. 2067–2073, 2007.

[261] C. Popov, W. Kulisch, M. Jelinek, A. Bock, and J. Strnad, "Nanocrystalline diamond/amorphous carbon composite films for applications in tribology, optics and biomedicine," *Thin Solid Films*, vol. 494, no. 1-2, pp. 92–97, 2006.

[262] H. Kawarada, "Hydrogen-terminated diamond surfaces and interfaces," *Surface Science Reports*, vol. 26, no. 7, pp. 205–259, 1996.

[263] J. Stotter, J. Zak, Z. Behler, Y. Show, and G. M. Swain, "Optical and electrochemical properties of optically transparent, boron-doped diamond thin films deposited on quartz," *Analytical Chemistry*, vol. 74, no. 23, pp. 5924–5930, 2002.

[264] K. E. Bennet, K. H. Lee, J. N. Kruchowski, S.-Y. Chang, M. P. Marsh, A. A. V. Orsow, A. Paez, and F. S. Manciu, "Development of conductive boron-doped diamond electrode: a microscopic, spectroscopic, and voltammetric study," *Materials*, vol. 6, no. 12, pp. 5726–5741, 2013.

[265] J. Stotter, S. Haymond, J. Zak, Y. Show, Z. Cvackova, and G. Swain, "Optically transparent diamond electrodes for uv-vis and ir spectroelectrochemistry," *The Electrochemical Society Interface*, vol. 12, no. 1, p. 33, 2003.

[266] Y. Zhang, S. Yoshihara, T. Shirakashi, and T. Kyomen, "Electrochemical characteristics of boron-doped, undoped and nitrogen-doped diamond films," *Diamond and related materials*, vol. 14, no. 2, pp. 213–219, 2005.

[267] Z. Suo, E. Ma, H. Gleskova, and S. Wagner, "Mechanics of rollable and foldable film-on-foil electronics," *Applied physics letters*, vol. 74, no. 8, pp. 1177–1179, 1999.

[268] W. Wang, M. Polo, G. Sanchez, J. Cifre, and J. Esteve, "Internal stress and strain in heavily boron-doped diamond films grown by microwave plasma and hot filament chemical vapor deposition," *Journal of applied physics*, vol. 80, no. 3, pp. 1846–1850, 1996.

[269] S.-Y. Jeong, Y.-W. Ma, J.-U. Lee, G.-J. Je, and B.-s. Shin, “Flexible and highly sensitive strain sensor based on laser-induced graphene pattern fabricated by 355 nm pulsed laser,” *Sensors*, vol. 19, no. 22, p. 4867, 2019.

[270] V. Selamneni, A. BS, and P. Sahatiya, “Highly air-stabilized black phosphorus on disposable paper substrate as a tunnelling effect-based highly sensitive piezoresistive strain sensor,” *Medical Devices & Sensors*, vol. 3, no. 4, p. e10099, 2020.

[271] M. Zhu, K. Sakamoto, J. Li, N. Inomata, M. Toda, and T. Ono, “Piezoresistive strain sensor based on monolayer molybdenum disulfide continuous film deposited by chemical vapor deposition,” *Journal of Micromechanics and Microengineering*, vol. 29, no. 5, p. 055002, 2019.

[272] H. Li, J. Zhang, J. Chen, Z. Luo, J. Zhang, Y. Alhandarish, Q. Liu, W. Tang, and L. Wang, “A supersensitive, multidimensional flexible strain gauge sensor based on ag/pdms for human activities monitoring,” *Scientific Reports*, vol. 10, no. 1, pp. 1–9, 2020.

[273] M. Hempel, D. Nezich, J. Kong, and M. Hofmann, “A novel class of strain gauges based on layered percolative films of 2d materials,” *Nano letters*, vol. 12, no. 11, pp. 5714–5718, 2012.

[274] S.-H. Bae, Y. Lee, B. K. Sharma, H.-J. Lee, J.-H. Kim, and J.-H. Ahn, “Graphene-based transparent strain sensor,” *Carbon*, vol. 51, pp. 236–242, 2013.

[275] P. Zomer, S. Dash, N. Tombros, and B. Van Wees, “A transfer technique for high mobility graphene devices on commercially available hexagonal boron nitride,” *Applied Physics Letters*, vol. 99, no. 23, p. 232104, 2011.

[276] I. Childres, L. A. Jauregui, W. Park, H. Cao, Y. P. Chen *et al.*, “Raman spectroscopy of graphene and related materials,” *New developments in photon and materials research*, vol. 1, pp. 1–20, 2013.

[277] J.-B. Wu, M.-L. Lin, X. Cong, H.-N. Liu, and P.-H. Tan, “Raman spectroscopy of graphene-based materials and its applications in related devices,” *Chemical Society Reviews*, vol. 47, no. 5, pp. 1822–1873, 2018.

[278] I. Vlassiouk, S. Smirnov, I. Ivanov, P. F. Fulvio, S. Dai, H. Meyer, M. Chi, D. Hensley, P. Datskos, and N. V. Lavrik, “Electrical and thermal conductivity of low temperature cvd graphene: the effect of disorder,” *Nanotechnology*, vol. 22, no. 27, p. 275716, 2011.

[279] S. Vollebregt, B. Alfano, F. Ricciardella, A. Giesbers, Y. Grachova, H. Van Zeijl, T. Polichetti, and P. M. Sarro, “A transfer-free wafer-scale cvd graphene fabrication process for mems/nems

sensors," in *2016 IEEE 29th International Conference on Micro Electro Mechanical Systems (MEMS)*. IEEE, 2016, pp. 17–20.

[280] T. Yoon, Q. Wu, D.-J. Yun, S. H. Kim, and Y. J. Song, "Direct tuning of graphene work function via chemical vapor deposition control," *Scientific Reports*, vol. 10, no. 1, p. 9870, 2020.

[281] G. Shao, "Work function and electron affinity of semiconductors: Doping effect and complication due to fermi level pinning," *Energy & Environmental Materials*, vol. 4, no. 3, pp. 273–276, 2021.

[282] J. Ryl, M. Cieslik, A. Zielinski, M. Ficek, B. Dec, K. Darowicki, and R. Bogdanowicz, "High-temperature oxidation of heavy boron-doped diamond electrodes: microstructural and electrochemical performance modification," *Materials*, vol. 13, no. 4, p. 964, 2020.

[283] J. Muñoz, J. Oliver-De La Cruz, G. Forte, and M. Pumera, "Graphene-based 3d-printed nanocomposite bioelectronics for monitoring breast cancer cell adhesion," *Biosensors and Bioelectronics*, p. 115113, 2023.

[284] N. V. Blaž, L. D. Živanov, M. G. Kisić, and A. B. Menićanin, "Fully 3d printed rolled capacitor based on conductive abs composite electrodes," *Electrochemistry Communications*, vol. 134, p. 107178, 2022.

[285] C. Kalinke, N. V. Neumsteir, G. de Oliveira Aparecido, T. V. de Barros Ferraz, P. L. Dos Santos, B. C. Janegitz, and J. A. Bonacin, "Comparison of activation processes for 3d printed pla-graphene electrodes: electrochemical properties and application for sensing of dopamine," *Analyst*, vol. 145, no. 4, pp. 1207–1218, 2020.

[286] R. Gusmão, M. P. Browne, Z. Sofer, and M. Pumera, "The capacitance and electron transfer of 3d-printed graphene electrodes are dramatically influenced by the type of solvent used for pre-treatment," *Electrochemistry Communications*, vol. 102, pp. 83–88, 2019.

[287] X. Xu, M. Koeberg, C.-J. Kuijpers, and E. Kok, "Development and validation of highly selective screening and confirmatory methods for the qualitative forensic analysis of organic explosive compounds with high performance liquid chromatography coupled with (photodiode array and) ltq ion trap/orbitrap mass spectrometric detections (hplc-(pda)-ltqorbitrap)," *Science & justice*, vol. 54, no. 1, pp. 3–21, 2014.

[288] T. D. Schachel, A. Stork, R. Schulte-Ladbeck, T. Vielhaber, and U. Karst, "Identification and differentiation of commercial and military explosives via high performance liquid chromatography–high resolution mass spectrometry (hplc-hrms), x-ray diffractometry (xrd)

and x-ray fluorescence spectroscopy (xrf): Towards a forensic substance database on explosives," *Forensic science international*, vol. 308, p. 110180, 2020.

[289] Y. T. Yew, A. Ambrosi, and M. Pumera, "Nitroaromatic explosives detection using electrochemically exfoliated graphene," *Scientific reports*, vol. 6, no. 1, p. 33276, 2016.

[290] W.-B. Ma, K.-H. Zhu, S.-F. Ye, Y. Wang, L. Guo, X.-Y. Tao, L.-T. Guo, H.-L. Fan, Z.-S. Liu, Y.-B. Zhu *et al.*, "A self-healing hydrogel electrolyte towards all-in-one flexible supercapacitors," *Journal of Materials Science: Materials in Electronics*, vol. 32, pp. 20 445–20 460, 2021.

[291] S. Alipoori, S. Mazinani, S. H. Aboutalebi, and F. Sharif, "Review of pva-based gel polymer electrolytes in flexible solid-state supercapacitors: Opportunities and challenges," *journal of energy storage*, vol. 27, p. 101072, 2020.

[292] S. Deshmukh, P. Jakobczyk, M. Ficek, J. Ryl, D. Geng, and R. Bogdanowicz, "Tuning the laser-induced processing of 3d porous graphenic nanostructures by boron-doped diamond particles for flexible microsupercapacitors," *Advanced Functional Materials*, vol. 32, no. 36, p. 2206097, 2022.

[293] A. Mortari, A. Maaroof, D. Martin, and M. B. Cortie, "Mesoporous gold electrodes for sensors based on electrochemical double layer capacitance," *Sensors and Actuators B: Chemical*, vol. 123, no. 1, pp. 262–268, 2007.

[294] B. Fang, Y.-Z. Wei, and M. Kumagai, "Modified carbon materials for high-rate edlcs application," *Journal of power sources*, vol. 155, no. 2, pp. 487–491, 2006.

[295] J. Á. Martín-Illán, L. Sierra, P. Ocón, and F. Zamora, "Electrochemical double-layer capacitor based on carbon@ covalent organic framework aerogels," *Angewandte Chemie*, vol. 134, no. 48, p. e202213106, 2022.

[296] A. Vu, X. Li, J. Phillips, A. Han, W. H. Smyrl, P. Buhlmann, and A. Stein, "Three-dimensionally ordered mesoporous (3dom) carbon materials as electrodes for electrochemical double-layer capacitors with ionic liquid electrolytes," *Chemistry of Materials*, vol. 25, no. 21, pp. 4137–4148, 2013.

[297] S. Westerlund and L. Ekstam, "Capacitor theory," *IEEE Transactions on Dielectrics and Electrical Insulation*, vol. 1, no. 5, pp. 826–839, 1994.

[298] P. C. Blog. (2023) Capacitance and its calculation, dielectric, dipoles and dielectric absorption. [Online]. Available: https://passive-components.eu/capacitors-capacitance-dipoles-and-dielectric-absorption/4/#split_content

[299] K. Hyyppa, “Dielectric absorption in memory capacitors,” *IEEE Transactions on Instrumentation and Measurement*, vol. 21, no. 1, pp. 53–56, 1972.

[300] K. Takagi, K. Natsui, T. Watanabe, and Y. Einaga, “Increasing the electric double-layer capacitance in boron-doped diamond electrodes,” *ChemElectroChem*, vol. 6, no. 6, pp. 1683–1687, 2019.

[301] E. Redondo and M. Pumera, “Mxene-functionalised 3d-printed electrodes for electrochemical capacitors,” *Electrochemistry Communications*, vol. 124, p. 106920, 2021.

[302] J. Xiao, M. Long, X. Zhang, J. Ouyang, H. Xu, and Y. Gao, “Theoretical predictions on the electronic structure and charge carrier mobility in 2d phosphorus sheets,” *Scientific reports*, vol. 5, no. 1, p. 9961, 2015.

[303] A. Avsar, I. J. Vera-Marun, T. J. You, K. Watanabe, T. Taniguchi, A. H. C. Neto, and B. Ozyilmaz, “Electrical characterization of fully encapsulated ultra thin black phosphorus-based heterostructures with graphene contacts,” *arXiv preprint arXiv:1412.1191*, 2014.

[304] A. Ziletti, A. Carvalho, D. K. Campbell, D. F. Coker, and A. C. Neto, “Oxygen defects in phosphorene,” *Physical review letters*, vol. 114, no. 4, p. 046801, 2015.

[305] A. Favron, E. Gaufres, F. Fossard, P. Lévesque, A. Phaneuf-L’Heureux, N. Tang, A. Loiseau, R. Leonelli, S. Francoeur, and R. Martel, “Exfoliating pristine black phosphorus down to the monolayer: photo-oxidation and electronic confinement effects,” *arXiv preprint arXiv:1408.0345*, 2014.

[306] J. D. Wood, S. A. Wells, D. Jariwala, K.-S. Chen, E. Cho, V. K. Sangwan, X. Liu, L. J. Lauhon, T. J. Marks, and M. C. Hersam, “Effective passivation of exfoliated black phosphorus transistors against ambient degradation,” *Nano letters*, vol. 14, no. 12, pp. 6964–6970, 2014.

[307] J. Kim, S. K. Baek, K. S. Kim, Y. J. Chang, and E. Choi, “Long-term stability study of graphene-passivated black phosphorus under air exposure,” *Current Applied Physics*, vol. 16, no. 2, pp. 165–169, 2016.

[308] J. Yoon and Z. Lee, “Effective passivation of black phosphorus under ambient conditions,” *Applied Microscopy*, vol. 47, no. 3, pp. 176–186, 2017.

[309] U. E. P. Agency. (2022) Freshwater screening benchmarks. [Online]. Available: https://www.epa.gov/risk/freshwater-screening-benchmarks

[310] M. Xu, B. Tang, Y. Lu, C. Zhu, Q. Lu, C. Zhu, L. Zheng, J. Zhang, N. Han, W. Fang *et al.*, “Machine learning driven synthesis of few-layered wte2 with geometrical control,” *Journal of the American Chemical Society*, vol. 143, no. 43, pp. 18 103–18 113, 2021.

LIST OF FIGURES

LIST OF TABLES